Anna Christina Stark, BSc

Pulsed electrodeposition of aluminum as half-cell reaction in secondary batteries

MASTER'S THESIS

to achieve the university degree of

Diplom-Ingenieurin

Master's degree programme: Technical Chemistry

submitted to

Graz University of Technology

Supervisor

Assoc.Prof. Dipl.-Chem. Dr.rer.nat., Bernhard Gollas

Institute for Chemistry and Technology of Materials

Graz, Jänner 2021

AFFIDAVIT

I declare that I have authored this thesis independently, that I have not used other than the declared sources/resources, and that I have explicitly indicated all material which has been quoted either literally or by content from the sources used. The text document uploaded to TUGRAZonline is identical to the present master‘s thesis dissertation.

Date

Signature

Acknowledgement

First, I would like to thank Prof. Bernhard Gollas for offering me the opportunity to conduct my master thesis at his research group. The patient guidance and the supervision during this work helped me a lot to finish this last task of my master studies.

A huge "thank you" goes out for Sandra Steiner. Since the beginning of the master thesis she was always there to critically argue about problems and find solutions for them. If I had a problem, I could always talk to her, doesn’t matter if there were private or research issues. Sandra is a great person to be around and I am going to miss the teamwork deeply, our long conversations in the office and seeing her happy and bubbly personality daily.

Additionally, am I thanking David Moser from the FELMI for providing the SEM images and giving further insights for discussing the obtained results.

A special thank goes out to the rest of the working group Sebastian Rohde & Philipp Materna and the staff at the institute for the friendly environment, the good time we had working together in the laboratory and in the office.

Furthermore, I want to thank my family especially my parents for their support during the last years and for always being there for me. I really appreciate your permanent love and the guidance you give me in life.

Last but not least, I thank my friends for always being there for me, lifting me up at bad days and sharing good moments. We started this journey together and it is pleased to see how everyone of our group made it to the end in his own kind of way. Thank you! With that, one chapter of my life closes and new chapter begins.

Abstract

In order to charge secondary aluminum batteries and to avoid dendritic or non-compact aluminum morphologies on the anode, the influence of pulse current was studied. As electrolyte the deep eutectic solvent consisting of $AlCl_3$ and urea with a molar ratio of 1.5:1 was used. In electrochemical metal deposition, the ratio of the deposition current over the limiting current affects the growth morphology. The limiting current of the aluminum deposition was investigated by cyclic voltammetry and rotating disk electrode voltammetry. Here, it was essential to compensate the resistance of the electrolyte throughout the measurements with the potentiostat. It was found that the limiting current of the electroactive species $[Al_2Cl_7]^-$ is not diffusion controlled. The Koutecky-Levich analysis revealed a kinetically controlled current density of -68.03 mA/cm² and a diffusion coefficient for $[Al_2Cl_7]^-$ of $2.39 \cdot 10^{-7}$ cm²/s. The pulsed current charging experiments were performed in Swagelok battery cells with copper current collectors as negative and aluminum as positive electrodes. With an average current density of -0.067 mA/cm² and varying pulse parameters, it has been shown that smaller duty cycles lead to more nuclei on the copper substrate and therefore, to a more homogeneous and slightly more compact aluminum layer. The most homogeneous morphology could be achieved with a pulse current of -6.71 mA/cm², a duty cycle of 0.01 and a frequency of 0.5 Hz.

Kurzfassung

Um während des Ladens einer sekundären Aluminiumbatterie dendritische oder nicht kompakte Aluminium-Morphologien auf der Anode zu vermeiden, wurde der Einfluss von Pulsstrom untersucht. Als Elektrolyt wurde die stark eutektische Flüssigkeit aus $AlCl_3$ und Harnstoff in einem Molverhältnis von 1.5:1 verwendet. In der elektrochemischen Metallabscheidung beeinflusst das Verhältnis Abscheidestrom zu Grenzstrom die Wachstumsmorphologie. Der Grenzstrom der Aluminiumabscheidung wurde mittels zyklischer Voltammetrie und Voltammetrie an rotierenden Scheibenelektroden untersucht. Hierbei war es unerlässlich, den Einfluss des Elektrolytwiderstands während der Messungen mit Hilfe des Potentiostaten zu kompensieren. Es stellt sich heraus, dass der Grenzstrom der elektroaktiven Spezies $[Al_2Cl_7]^-$ nicht diffusionskontrolliert ist. Die Koutecky-Levich-Analyse ergab eine kinetisch kontrollierte Grenzstromdichte von -68.03 mA/cm² und einen Diffusionskoeffizient für $[Al_2Cl_7]^-$ von $2.39 \cdot 10^{-7}$ cm²/s. Pulsstrom-Ladeversuche wurden in Swagelok-Zellen mit Stromableitern aus Kupfer als negative und Aluminium als positive Elektroden durchgeführt. Bei einer mittleren Stromdichte von –0.067 mA/cm² und variierenden Pulsparametern hat sich gezeigt, dass kleine Lastzyklen zu mehr Kristallisationskeimen und dadurch zu einer homogeneren und etwas kompakteren Aluminiumschicht auf der Arbeitselektrode führen. Die homogenste Morphologie wurde mit einer Pulsstromdichte von –6.71 mA/cm², einem Lastzyklus von 0.01 und einer Frequenz von 0.5 Hz erreicht.

List of abbreviations, variables and constants

Abbreviations

[BMIm]Cl	*1-butyl-3-methylimidazoliumchloride*
[EMIm]Cl	*1-ethyl-3-methylimidazoliumchloride*
Ah	*ampere hours*
AIB	*aluminum-ion battery*
BR	*basis-oriented reproduction type*
CA	*chronoamperometry*
CE	*counter electrode*
CEff	*current efficiency / coulombic efficiency*
CV	*cyclic voltammogram*
DC	*direct current*
DES	*deep eutectic solvent*
EDL	*electric double layer*
EDX / EDS	*energy dispersive X-ray spectroscopy*
Et_3NHCl	*trimethylamine hydrochloride*
EtOH	*ethanol*
FI	*field-oriented isolated crystals type*
FT	*field-oriented texture type*
g	*gram*
GC	*glassy carbon*
h	*hours*
HBD	*hydrogen bond donors*
ILs	*ionic liquids*
LIB	*lithium-ion battery*
ms	*milliseconds*
Na_3AlF_6	*sodium hexafluoroaluminate (cryolite)*
OCP	*open cell potential*
PEEK	*polyether ether ketone*
PFA	*perfluoroalkoxyalkanes*
PIC	*pulse-interrupt current*
PTFE	*polytetrafluoroethylene*
RDE	*rotating disk electrode*
RE	*reference electrode*
rpm	*rotations per minute*

RT	*room temperature*
RTIL	*room temperature ionic liquid*
SEM	*scanning electron microscopy*
SHE	*standard hydrogen electrode*
TEM	*transition electron microscopy*
UD	*unoriented dispersion type*
Uralumina 150	*electrolyte* $AlCl_3$*:urea 1.5 mol:1 mol*
WE	*working electrode*
Z	*twinning intermediate growth type*

Variables and constants

j_d	*diffusion limited current density*
K_{eq}	*equilibrium constant*
k_{red}	*reduction rate constant*
η_{κ}	*nucleation growth over potential*
$\emptyset$	*diameter*
A	*surface area*
c_{b}	*concentration in the bulk electrolyte*
C_{dl}	*double layer capacitance*
c_{n}	*concentration at a specific point in the diffusion layer*
c_{s}	*concentration at the surface of the electrode*
D	*diffusion coefficient*
e^-	*electron*
E^0	*standard potential*
E_{a}	*applied potential*
E_{p}	*polarization potential working electrode*
E_{u}	*uncompensated potential drop /* iR_{u}
F	*Faraday constant*
f	*frequency*
i	*electric current*
i_{p}	*peak current*
iR_{u}	*ohmic drop, potential drop*
j	*current density*
j_{l}	*limiting current density*
j_{p}	*peak current density*
L	*length*
l	*distance between working electrode and tip of Luggin-capillary*
M	*atom mass*
M^+	*metal cation*
n	*number of moles*
Q	*charge* $Q=i\cdot t$
R	*electrical resistance*
r_{c}	*duty cycle*
R_{u}	*uncompensated resistance*
T	*temperature*

t	*time*
t_{off}	*pulse off-time*
t_{on}	*pulse length*
U_{cell}	*cell voltage*
i_K	*kinetic current*
k	*reaction rate constant*
r	*radius*
z	*number of electrons transferred per ion*
δ_{p}	*thickness of diffusion layer*
δ_{s}	*thickness of stagnant diffusion layer*
η	*overpotential*
κ	*specific conductivity*
μ	*mikro*
ν	*scran rate*
π	*3.1415*
σ	*electrical conductivity*
τ	*transition time*
υ	*kinematic viscosity*
ω	*angular rotation rate*

Table of contents

1 Introduction

In the next years the continuing trend of shifting power generation from fossil fuels to renewable sources like wind and solar will continue. It is due to the indispensable global demand of energy whilst working on to minimise the global CO_2 emissions. The continuity of the power supply of renewable energy sources largely depend on the climate, season and other conditions in the area where the power plant is located. This leads to power peaks and valleys. To guarantee a stable grid attractive energy conversion and storage devices are needed. Suitable energy conversion units are for instance batteries, fuel cells, photovoltaic devices or supercapacitors.[1][2][3] Their operating principles involve different mechanisms. For example, electrochemical energy storages devices like batteries store charge within the electrodes and in the case of fuel cells charge is stored in the fuel, which is fed externally onto the surface of the electrodes. [4]

Currently, lead-acid batteries, sodium sulfur (NaS) and Li-ion batteries (LIB) are the most widely employed and mature battery storage systems. Li-ion batteries are commonly used for laptops, smart phones and other portable electronic devices.[2][5][6] The attractiveness of Li-ion battery technology resides in its versatility as its covers a wide range of applications as mentioned above. It dominated the rechargeable battery market and a great amount of research is invested into LIB. The element Li is of interest in the scientific world due to the highest redox potential (–3.04 V vs. SHE) of all elements, a small radius (90 pm) and the low weight (6.94 g/mol). This promises high energy density, high power density and fast diffusion rates through the electrode material in LIBs. Nevertheless, there are some drawbacks. One issue in material perspective is the low relative abundance of lithium in the earth crust, which gives rise to the fear of lithium shortage in the future. High energy costs of battery manufacturing and recycling plus safety issues in regard of the used electrolytes makes the LIB, especially for large-scale applications, worthy of discussion.[2][4][7][8][9][10]

Based on these facts, other electropositive metals / new chemistries are needed for assembling more sustainable batteries to satisfy the expectations on future energy storage devices.

1.1 Aluminum as anode material

A promising alternative to lithium is the trivalent aluminum, a lightweight and cheap abundant metallic element in the earth crust. It has the ability to exchange three electrons during the electrochemical process. When used as anode material in aluminum ion batteries (AIB) the theoretical volumetric capacity is 8.04 Ah/cm³ which is four times the value of lithium with 2.05 Ah/cm³ and the gravimetric capacity is 2.98 Ah/g compared to lithium with 3.86 Ah/g. The safety hazard is reduced due to the better air stability compared to lithium metal.[11][12][13][14][15] When exposing aluminum to air, a protective passive film forms. On the one side, it extremely improves the safety level of electrochemical storage devises when used as anode material. On the other side, early attempts of using aluminum in batteries as anode material did not succeed mainly due to the protective oxide layer. Unfortunately, it reduces the electrode potential resulting in a much lower batteries working voltage in respect to the theoretical one.[12] In aluminum batteries with aqueous electrolyte the hydrogen evolution at the cathode side at more positive standard potentials hinders the reversible deposition of pure aluminum (−1.66 V vs. SHE) making it only a primary one.[16] Based on this unpleasant characteristic, the necessity of working on non-aqueous electrolyte was given to develop a secondary aluminum battery and making electrodeposition and electrostripping of aluminum reversible.

1.2 Electrolytes for aluminum deposition

Since the 1970´s molten salt chloroaluminate melts like the binary NaCl:$AlCl_3$ or the ternary KCl:NaCl:$AlCl_3$ are well known systems for aluminum electrodeposition.[12] They have been considered as possible electrolytes for the development of secondary aluminum batteries. The disadvantage is the high operative temperature above 100 ° C. The switch from monovalent metal cations to organic long-chain cations decreased the melting point to room temperature.[17][18][19]

Ionic liquids (ILs) are a class of compounds containing organic cations or anions that melt at or near room temperature. They represent a new type of non-aqueous electrolytes that combine the benefits of both solid and liquid systems.[20] They offer unique properties such as high ionic conductivity, low vapour pressure, non-flammability, thermal and chemical stability with large electrochemical potential windows. In particular, ILs based on $AlCl_3$ and quaternary ammonium salts are the most utilized media for reversible electrodeposition in secondary aluminum batteries. Especially, the eutectic mixture of 1-ethyl-3-methylimidazolium chloride ([EMIm]Cl) and $AlCl_3$ with a molar excess of $AlCl_3$ is one of the most intensely investigated ILs for the deposition of aluminum.[16] The molar ratio of $AlCl_3$ and the quaternary ammonium salt defines, if the electrolyte is Lewis acidic, neutral or Lewis basic and therefore, what kind of anionic species exists.[21] In basic and neutral melts, where the molar ratio is < 1 or 1, the main anionic species in solution is $[AlCl_4]^-$ [eq. (1)]. The electrodeposition of Al from these ILs is only possible in Lewis acidic media, e.g. if there is an excess of $AlCl_3$ [eq.(2)]. In this case, the dominant species is $[Al_2Cl_7]^-$, which is of great utility in secondary batteries, because the reduction of the species to metallic Al is reversible [eq.(3)].

$$AlCl_3 + [EMIm]Cl \longrightarrow [AlCl_4]^- + [EMIm]^+ \quad (1)$$

$$[AlCl_4]^- + AlCl_3 \rightleftharpoons [Al_2Cl_7]^- \quad (2)$$

$$4\ [Al_2Cl_7]^- + 3\ e^- \rightleftharpoons Al + 7\ [AlCl_4]^- \quad (3)$$

The $[AlCl_4]^-$ is far too stable to be reduced at potentials less cathodic than that of the ammonium cation making the ionic liquid unsuitable for battery applications.

Chloroaluminate ILs are highly hygroscopic decomposing under an exothermic reaction to hydrochloric acid HCl and aluminum hydroxide $Al(OH)_3$ when exposed to moisture.[22][23] Over the years, the number of producible RTIL grew together with the toxicity of some RTIL and their high price. As a result, the continuing interest in this kind of solvents leads to the production of so called deep eutectic solvents (DES), which are ionic liquid analogues. DES are obtained e.g. by mixing a metal salt with a hydrogen bond donor (HBD), such as an alcohol or an amide as complexing agent. Besides this, the formation of DES is also possible by mixing quaternary ammonium salts with HBD or a metal salt. The majority of studies have focused on cations based on nitrogen, but phosphonium and sulfonium based quaternary salts do exist as well.[24]

The term eutectic is derived from the Greek word for low melting e.g. the resulting eutectic mixture is characterized by a melting point considerably lower than its individual components. H-bond formation between the halide anion X^- and the H-bond moiety causes a charge delocalization. The formed complex between the metal salt and the HBD is liquid at ambient temperatures. This is the difference to ionic liquids, which are based on discrete anions compared to DES, which are based on anionic complexes.[24]

In most cases, a DES is obtained by mixing the components together and stirring mechanically.

At room temperature, is has the general properties of ILs such as low volatility, low melting temperature and nonflammability.[20]

Abood et al. showed that it is possible to form DESs by adding a HBD like acetamide or urea to a metal chloride like aluminum chloride [eq. (4)].[25] The ionic liquid analogue formed through mixing urea and $AlCl_3$ has previously shown to serve as a low-cost electrolyte for an aluminum secondary battery.[26][27]

$$2\ AlCl_3 + n\ urea \longrightarrow [AlCl_4]^- + [AlCl_2\ (urea)_n]^+ \qquad (4)$$

Al deposition is possible from cationic species of the form $[AlCl_2\ (amide)_n]^+$ and starts in the potential range around −1 V vs. Al/ Al^{3+} [eq. (5)]. In this potential window $[AlCl_4]^-$ cannot be reduced. This makes aluminum deposition possible in Lewis neutral media in contrast to room temperature ionic liquids.[25][26]

$$2\ [AlCl_2\ (urea)_n]^+ + 3\ e^- \rightleftharpoons Al + n\ urea + [AlCl_4]^- \qquad (5)$$

By adding more $AlCl_3$ to the eutectic mixture like in equation (2), the melt gets Lewis acidic and the reaction generates an increasing fraction of $[Al_2Cl_7]^-$ in the liquid, which can be reduced to Al according to eq. (3).
Therefore, two ionic species are reducible at moderate cathodic potentials in DES based on $AlCl_3$:amide which leads to two possible deposition pathways.[28]

Nowadays, the most common non-aqueous electrolytes used for electrochemical deposition and stripping of aluminum in Al secondary batteries are $AlCl_3$:[EMIm]Cl, $AlCl_3$:[BMIm]Cl, $AlCl_3$:Et_3NHCl, $AlCl_3$:Urea and $AlCl_3$:Acetamide.[24][25][29][30][31] The $AlCl_3$:[EMIm]Cl ionic liquid is the most popular one due to its high ionic conductivity, large potential window, low vapour pressure and its good aluminum stripping and deposition properties with high coulombic efficiency.[32] The DES based on amides are also liquid at room temperature, show slightly lower conductivity ($AlCl_3$/urea: $\sigma = 0.6$ mS/cm, $AlCl_3$:acetamide: $\sigma = 0.8$ mS/cm) and higher viscosity compared to the ionic liquids with organic cations like $AlCl_3$:imidazolium electrolytes ($\sigma \approx 10$ mS/cm).[13][25]
Owing to higher viscosities, due to the presence of an extensive hydrogen bond network, a lower mobility of free species and larger ion size leads to lower conductivities.[29]

1.3 Morphology of electrodeposited metals

The metal deposition from an aqueous solution or a molten salt / ionic liquid is described as electrochemical or electroless / chemical surface metallising. The electrochemical method is also known as electroplating or electrodeposition and is used to form a metal coating onto metallic or electrically conducting surfaces. In this section, the focus lies on the electrochemical method. The two basic forms are direct current (DC) and pulsed-current deposition.

The electrodeposition of metallic layers from electrolyte is based on the discharge of the metal ions present in the electrolyte at the cathodic surface. Before they are reduced at the surface, they need to wander from the bulk of the electrolyte through the double layer to the surface of the substrate. The metal ions deposit onto the surface by accepting electrons from an external electric power source. After ad-atoms have formed, they diffuse along the surface towards energetically favoured growth sites like edges, steps or kinks or they are directly deposited onto a growth site, where they can incorporate into the crystal lattice. If there are no growth sites, new nuclei must form. After the nuclei have reached a critical size, also called a thermodynamically stable state, the growth process begins.[33][34]

There are two different nucleation models, instantaneous and progressive nucleation. Instantaneous nucleation is identified as all nuclei formed at nearly the same time followed by the growth process. In contrast to progressive nucleation, where it is assumed that nucleation does not occur simultaneously over the entire cathode surface. It is more like a process extended in time so that crystals generated earlier may be considerably larger in size than ones generated later. This causes inhomogeneous crystal size distribution. Instantaneous nucleation achieves better crystalline quality than progressive nucleation.[34][35]

Both processes, the nucleation and the growth process, can be expressed in terms of characteristic overpotential. Overpotential is defined as the difference between equilibrium potential and potential of the same electrode when current is flowing, due to the change of the surface concentration of ad-atoms.[36] Due to the higher activation energy of nucleation, it contributes more to the overpotential. There can be significant differences of crystallisation overpotentials at various points on the surface. In electrochemically deposited metal layers, most commonly, the layers are polycrystalline and consist of a countless number of small grains or crystallites.

Winand et al. [37] explains the observed crystal shapes and therefore, the obtained morphology in polycrystalline systems based on two parameters: the ratio of current density to the bulk concentration of the active species (j/c) and the inhibition intensity. If the diffusion layer thickness is inhomogeneous on the substrate surface, j/j_d (limiting current density) is used instead of j/c. The influence of j/j_d onto the morphology of the electrodeposit can be explained with the impact of the overpotential on the local current (density) distribution and therefore, the change in the concentration of the active species at the surface of the substrate. As inhibition intensity the concentration of physically or chemically absorbed species, like atoms, ions or molecules on the substrate surface is understood. They hinder the process on the cathode surface, but they are not homogeneously spread so they do favour active sites. For example, if they get reduced instead of the metal ion on the substrate surface, they decrease the current density for the reduction of active species and in the following the current efficiency. They change the morphology of the deposit as well as the overpotential of the working electrode.

Generally said, by increasing j/j_d and / or the inhibition intensity, the nucleation rate increases and the grain size of the deposit decreases. If the inhibition is constant and the current density is increasing, the growth rate of the deposited metal layer increases, but the number of atoms / ions on the surface decrease.

By contrast, if the current density is constant, but the inhibition is increasing, then the growth rate of the deposited metal layer decreases and the number of the ions / atoms at the surface increase. The different growth types of polycrystalline electrodeposits are summed up in Fig. 1.

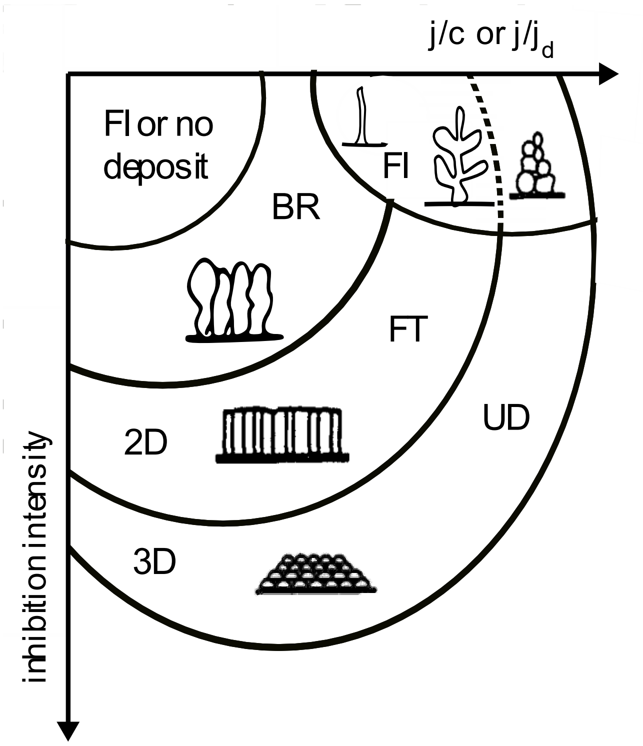

Fig. 1: Different growth types of polycrystalline electrodeposits as a function of current density over limiting current density ratio and inhibition intensity. (Analogous to [37]*, p. 578, Fig. 6)*

The first main growth type in this diagram is FI (field-oriented isolated crystal type), which is observed at low inhibition and can form with increasing current density whiskers, dendrites and even powdery deposits. The second main growth type is BR (basis-oriented reproduction type), which is observed at moderate conditions. Typically, good lateral growth is obtained, but by increasing deposition time, crystals become large and the surface rough like in FI type. Z (twinning intermediate growth type) lies between FR and FT. For the fourth grow type FT (field-oriented texture) a large number of elongated crystals perpendicular to the substrate is typical, as well as a coherent deposit. The last type is UD (unoriented dispersion type), obtained at high inhibition intensity and high current density and producing small crystals. The types are classified according to Fischer et al. [38]. The first four types are obtained through 2D nucleation, only the last growth type is obtained from 3D nucleation at the substrate surface. After the electrodeposition is completed, the morphology of the polycrystalline deposits formed can be described as:

i) compact
ii) disperse: dendritic or spongy, granular, etc.

The reality is sometimes much more complicated and each morphology should be described individually in terms of its structural features like grain dimension, orientation and composition.

The morphology is likely to be the most important property of electrodeposited metals. It mainly depends on kinetic parameters of the deposition process, the deposition overpotential, deposition time and current density. Also, the crystal structure and type of substrate metal play an important role. The substrate retains its influence up to a certain deposit thickness. As the layer gets thicker, the structure and morphology is determined only by deposition conditions.[39][40]

The effect of the deposition overpotential and the current density on the structure and morphology of metal film is enormous. The higher the applied overpotential, the greater the number of weaker active sites taking part in the nucleation process and hence, the greater the nucleus density on the surface. The larger the nucleation rates, the more homogeneous and more evenly is the crystal grain size distribution, which leads to a smoother and less coarse deposit.

Especially the current density in pulsed current deposition influences the morphology. By using pulses very short in time, the diffusion layer gets extremely thin. In order to deposit a given amount of metal in a set time, the resulting peak current pulses need to be higher.

Consequently, it results in higher deposition overpotentials, which promote the nucleation process. Hence, a finer grained deposit form. Despite this, during off-time by products of the reduction process or other species in the electrolyte, which were transported to the surface of the substrate during the current pulse, are able to diffuse back into bulk solution and are therefore less likely to be incorporated into the deposit.[33]

The structure of metal deposits can be investigated with electron microscopy like scanning electron microscopy (SEM) or transmission electron microscopy (TEM). The SEM is mainly used for monitoring deposit structures and the advantage over optical microscopy is a greater depth of field, which allows a rough topography to be completely in focus. The SEM has better resolution than optical microscopy and TEM has an even higher resolution than scanning electron microscopy. It is used to measure the structure of the deposit on nanoscale to determine the grain size. Also, a detailed crystal structure analysis is possible due to diffractometry.[40]

Aluminum is widely used in the industry due to its excellent properties, like in metal coatings to improve corrosion resistance and its high advantageous recycling. Commercial aluminum production is carried out by the high temperature (~ 1000 °C) Hall-Heroult process. Besides this enormously energy-intensive process, which needs high quantities of electricity, water and resources, new alternative methods should come into light to replace the energy-intensive aluminum production activities.[41]

Coating with aluminum can be done by hot dipping, thermal spraying, physical or chemical vapour deposition to name a few.[42] Most of the commercial Al electroplating is done nowadays by the SIGAL process, originally developed by Siemens AG in Germany. The mix of organoaluminum compounds, aromatic solvents, and other additives such as alkali halides or hydrides and quaternary ammonium salts leads to pyrophoric and flammable electrolytes. No ideal conditions, in case of safety and environmental perspectives.[41][43]

Over the last decades electrodeposition from ILs has received a lot of attention. Chloroaluminate ILs are the most frequently studied system.[21] They have not been completely accepted in many applications because of their dependence on the use of an inert gas atmosphere, inherent toxicity, high cost and hygroscopic nature. The goal is to improve the Al and Al alloy plating technology compared to the current Al plating technology by using these ILs.

The electrodeposition and surface morphology of aluminum on different substrates depends on the current density and / or the potential applied, the Lewis acidity, additives, diluents, deposition time and temperature.[44] Especially when used in aluminum battery systems, the interface between the aluminum anode and the electrolyte needs to be considered. While electrodeposition of Al during the charging process in the battery, dendrite growth may produce a short circuit when piercing the separator, causing safety hazards and cell failure or capacity fade due to anode mass loss.[13][15] The reversibility of the reaction and the efficiency of the electrochemical process are of importance for batteries. But it should also be noted that the metallurgical aspects of the deposit such as the quality of the deposit in terms of roughness, crystal size and morphology must be studied.[11] For the use in secondary batteries, the non-aqueous electrolytes must succeed in two topics: electroplating and energy storage.

Finding the right deposition parameters for electrodeposition of Al from chloroaluminate ILs can be a hard task and has to be thought trough individually in dependence of starting conditions.

Schoetz et al. [45] reported the morphology of Al deposition from $AlCl_3$:[EMIm]Cl onto bare Al at −0.16 mA/cm² for 30 minutes at RT. The grain size increased with increasing Lewis acidity of the IL. The shape of the deposit becomes more hemispherical as the grain size increased from 200 to 500 nm. In ultra acidic ILs (2.3:1 molar ratio) the obtained grains grow to cauliflower-like agglomerates with a size ranging from 1 µm to 2 µm. It is reported, that dendrites are only formed at current densities over −100 mA/cm².

Bakkar et al. [42] showed that higher overpotentials improving deposit compactness and reduced grain size to nm scale when Al is deposited potentiostatically on low carbon steel from $AlCl_3$:[EMIm]Cl (1.5:1 molar ratio).

Tang et al. [46] studied the Al electrodeposition on Pt substrate at RT from $AlCl_3$:[EMIm]Cl with a molar ratio of 2:1. Via galvanostatic polarization the particle size decreased with increasing current density. Starting from −3 mA/cm² with flaky grains and poor adherence to −8 mA/cm² with smooth and dense surface, due to fine particles. In addition, pulsed deposition of Al was carried out, where the current density was fixed at −16 mA/cm² and the duty cycle and the frequency were varied. The result was a dense and compact Al layer in all cases of the monopolar pulse parameters. The most dense and smoothest metal layer was obtained with long off-times and short on-times.

Li et al. [47] deposited Al from a 2:1 molar ratio $AlCl_3$:[EMIm]Cl electrolyte onto Cu substrate by direct current and pulse current deposition at 60 °C. There was an increase in the deposit compactness and a decrease in grain size by increasing the current density from −5 mA/cm² to −20 mA/cm² by DC deposition. By comparing the DC deposition at −5 mA/cm² to pulsed current deposition, there was a decrease in the grain size from 20 µm to 15 µm and an improvement in the surface roughness. Pulse current density, duty cycle influences the morphology of the substrate as well as the temperature. The adhesion of the Al deposited via pulsed current deposition was poor. During off-time of 5 ms the deposited Al grains coalescence to bigger grains in comparison to 1 ms or 2 ms off-time (t_{on} + t_{off} = 10 ms). Also, the grain size of the deposits increased as the temperature increased from 60 °C to 90 °C. Grain shape changed from spherical to flake like grains, respectively. The smallest grain size of 0.3 µm was obtained at 25 °C, 8 ms on-time and 2 ms off-time, 20 Hz and −8 mA/cm².

Cvetkovic et al. [44] investigated the difference in the obtained Al morphology when Al is deposited onto GC or Al as substrate material from $AlCl_3$:urea (1.6:1 molar ratio) electrolyte at different temperatures. In both cases (GC & Al) no complete coverage of the substrate was possible, even though the coverage of the Al substrate was higher. On Al substrate the deposition morphology was flaky at −250 mV for 30 min at 35 °C compared to cauliflower-like agglomerates obtained a −2 mA/cm² at 50 °C. The same potential applied to deposit Al onto GC, except the temperature changed to 50 °C, the particle size is more inhomogeneous and less flaky. By comparing the galvanostatic deposition at −2 mA/cm² onto GC, there are regular crystalline particles and particles enriched with 3D additions like agglomerates.

Abood et al. [21] deposited Al from $AlCl_3$:urea electrolyte onto Cu substrate under variable conditions. A molar ratio of 1.3:1 was used for Al deposition at a constant potential of −0.6 V for 1.5 h. The temperature was varied between 20 and 60 °C. The obtained grain size varied from sand like particles at 20 °C and 30 °C to flake like structure at 40 °C and needle like structures at 50 °C and 60 °C. The particle size increased from 123 nm to 152 nm with increasing temperature. At 20 °C the deposited Al layer was silvery grey and changed to dark grey appearance at 60 °C.

In brief, the most frequently reported morphology in electrochemically deposited Al is described as hemispherical, cauliflower or flake like. The particle size decreases with increasing current densities. It is shown that the morphology of plated Al layers can be improved in terms of roughness and density by switching from direct current to pulse plating method. During off-time, particles tend to agglomerate, also a poor adhesion of the Al layer was recognized with pulsed interval current (PIC) method.

Tsuda at al. [43]. reviews the progress in electrochemical plating technology with haloaluminate RTILs and DES. It is reported that at moderate current densities (≤ −40 mA/cm²) the morphology is relatively dense. At higher current densities, dendrite formation can be observed. The problem is rooted in the depletion of $[A_2Cl_7]^-$ at the electrode surface, which changes the Lewis acidity during the plating process. Ways to overcome this problem is by increasing the temperature of the plating bath or by adding aromatic hydrocarbon co-solvents like benzene or toluene to improve the viscosity and the conductivity. It is also reported that pulse plating methods improve the deposit morphology.

1.4 Pulse-plating of aluminum

Pulse and pulse reverse plating is the electrochemical deposition of metals by a periodical variation of the applied current or voltage. Deposition by pulse current occurs under continuously changing conditions and therefore produces deposits, which differ significantly from those obtained by constant direct current (DC) plating, where the processes at the electrode surface are unchanged during the plating process. There are two variations pulse plating can be divided into:

i) *Periodically interrupted DC current plating (unipolar waveforms) or*
ii) *Periodically current reversal plating (bipolar waveforms)*

The main idea behind applying a pulsed current or a pulsed potential is to achieve better functional and / or decorative coatings. In batteries, the formation of dendrites at the electrode surface are fatal causing safety hazards and minimizing lifetime.[15] By using pulse reverse plating, the growth of dendrites and therefore, the morphology of the plated metal can be influenced. For this thesis, the bipolar metal deposition was not tested. For an energy storage device like the secondary aluminum batterie, an energy and time efficient charging process is of need. By using pulse reverse plating as the charging process, the opposite would be the case.
The advantage of pulse and pulse reverse plating was first recognized in the early 1950s and the first patent goes back to this time.[48] In pulse plating and general, the galvanostatic process is of favoured over the potential controlled process in metal deposition. There are some control and measuring issues of potentiostatic metal deposition. In industrial processes where a two-electrode configuration is standard, the precise control of the WE potential is difficult. A fraction of the overall cell voltage imposed or measured is used to drive electrochemical reaction at counter electrode, plus the Ohmic drop of the solution leads to mistakes. The reference electrode used in standard three-electrode set ups in laboratory scale, enables to control the potential of the WE. In industrial scale where large currents are used, the RE would help to control the WE potential, but even a small potential drop between the RE and the WE, would lead to several volts mistakes.[48]
By controlling or measuring the current over the period of time during the electrolysis regarding the Faradays law of electrolysis [eq. (6)]:

$$Q = z \cdot F \cdot n \qquad (6)$$

Q .... *total charge [C]*
z .... *number of electrons transferred per ion*
F .... *Faraday constant, 96485 [C/mol]*
n............... *number of moles [mol]*

the mass of plated metal is proportional to the number of moles of electrons transferred when $Q = i \cdot t$ and $n = \frac{m}{M}$ [eq. (7)]:

$$m = \frac{I \cdot t \cdot M}{z \cdot F} \tag{7}$$

m............. *mass [g]*
I .... *electrical current [A]*
t .... *time [h]*
M............. *atomic mass [g/mol]*
z .... *number of electrons transferred per ion*
F .... *Faraday constant, 96485 [C/mol]*

The plating current is an important process parameter for an electrolytic process, because the mass of the plated metal can be determined. [40]
The almost unlimited combination of pulse parameters for achieving the same current densities like in DC plating is the big advantage. Nevertheless, pulse parameters like frequency, duty cycle and pulse current density (height of the pulse) need to be appropriately chosen (Fig. 2). This can be a difficult task due to the wide variety of pulse parameters. For example, the duty cycle (r_c) equals the pulse length divided by the period e.g. the on-time of the pulse divided by the sum of on and off-time [eq. (8)].

$$r_\mathrm{c} = \frac{t_\mathrm{on}}{t_\mathrm{on} + t_\mathrm{off}} \tag{8}$$

It is expressed in percentage or ratio of on-time like 50 % or 0.5, respectively. The pulse frequency is another important parameter that can influence the deposition results. The frequency is defined as the number of times a wave (here, current or potential wave) is produced within a second [eq. (9)].

$$f = \frac{1}{t} \tag{9}$$

where *t* is the time in seconds. The unit of the frequency is Hz.

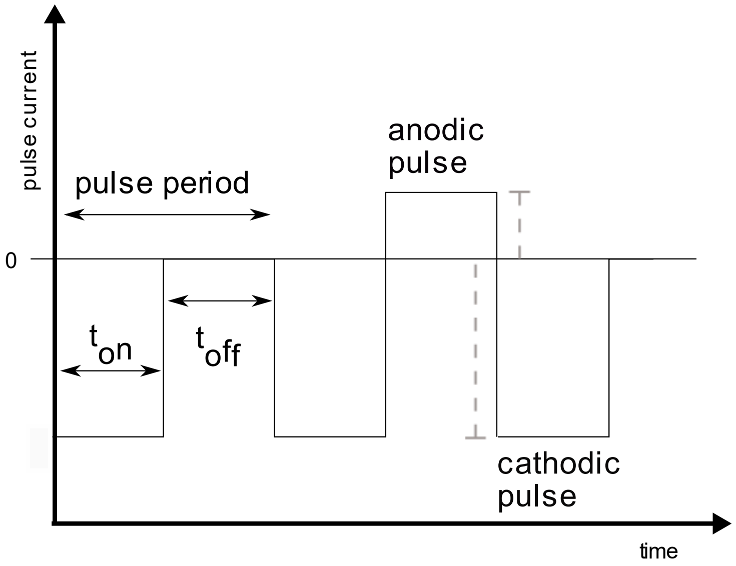

Fig. 2: Schematic diagram of the current waveform of the pulse current used in electrochemical deposition of metals. When the current is applied, it is called on-time, in contrast to off-time, where no current is flowing. The pulse period is the sum of the on and the off time and thus the inverse of the pulse frequency. The anodic pulse also refers to pulse reverse.

Before working on the experimental parameters, the various theoretical concepts and fundamental principles of pulse deposition and dissolution need to be understood.

The electrode gets charged due to deposition and dissolution reactions of metal ions in equilibrium at the electrode-electrolyte interface. Therefore, it attracts counter charged species in solution to the electrode surface. The interface between the two phases is termed electrochemical double layer. The interface electrically behaves like a simple parallel plate capacitor with the capacity C_{dl} also known as the double layer capacity. If a potential or current pulse is applied, the system is shifted from equilibrium and a net dissolution or deposition of metal species is allowed, accompanied by a current flow. In the case of pulse experiments, it is necessary to distinguish between faradaic and non-faradaic currents. First, a non-faradaic current is used to charge the double layer and negligible deposition or dissolution occurs. When the capacitor is nearly fully charged, faradaic current dominates, which is caused by electrochemical reactions at the electrode surface. Reactions requiring the smallest applied overpotential will take place according to their redox potential. [49]

At the end of the pulse, the capacitor is discharged when the current or potential is switched off. In the case of deposition, the discharged species also called ad-atoms are incorporated into the crystal lattice. By diffusion along the electrode surface, the ad-atoms can access sites to find a thermodynamically favourable position. The ad-atoms can be incorporated within an existing crystal lattice or nucleate at the electrode surface. During off time, re-crystallisation can occur. Below a critical radius, newly formed nuclei are thermodynamically unstable due to their high surface energy and can dissolve. High pulse current densities in pulse plating favour the formation of small nuclei.[48] A high current density leads to a high overpotential and provides enough energy to enable the formation of a lot of thermodynamically stable nuclei on the substrate.

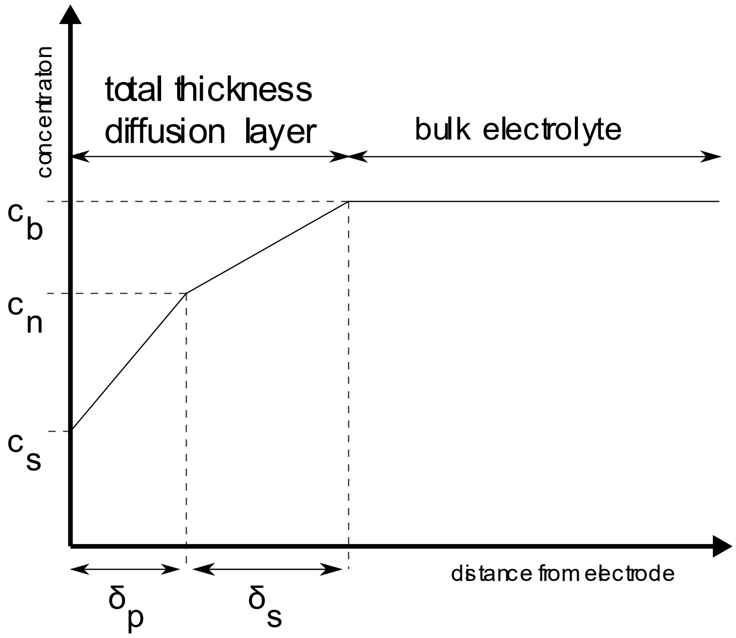

Fig. 3: Diffusion layer model for the electrolyte in front of the working electrode. The abbreviations refer to: thickness pulsating diffusion layer (δ_p); steady-state, stagnant diffusion layer (δ_s), c_b is the *bulk electrolyte and* c_n *the concentration at* $x= \delta p$; c_s *refers to the surface concentration of the active species in the electrolyte.*

After consumption of the metal ions at the electrode surface, the concentration near the electrode is decreasing and it has to be replenished from the bulk electrolyte to allow further deposition. During the deposition pulse, a depletion layer, also called diffusion layer, begins to form (Fig. 3). Diffusion arises from the concentration gradient and transports metal ions from the bulk to the electrode surface. For pulse deposition systems, an inner and outer diffusion layer exists. The concentration profile in the inner diffusion layer follows the frequency of the pulse waveform. Next to diffusional mass transfer, convection (pressure gradient) and migration (potential gradient) can also arise in the bulk of the electrolyte. By calculating the flux of the active species to the surface of the electrode, convection can be neglected if conditions are quiescent and no density gradient forms.[50] For short current pulses, the inner diffusion layer is very thin.[48] If the metal ion reduction is faster than the replenishment of the species from the bulk electrolyte, longer off-times can help to regenerate the metal ion concentration in the inner diffusion layer. Another possibility would be to reduce the pulse current density.

The most common method of determining the current, at which the reactant concentration at the electrode surface reaches zero, is the limiting current technique.[51] The limiting current for the deposition of a metal ion with a bulk concentration of c_b is given by the following equation (10):

$$\overrightarrow{|j_{\mathrm{lim}}|} = z \cdot F \cdot D \cdot \frac{c_\mathrm{b}}{\delta_\mathrm{s}} \tag{10}$$

j_{lim} .... *limiting current densitiy [A/cm²]*
z.............. *number of electrons transferred per ion*
F .... *Faraday constant, 96485 [C/mol]*
D .... *diffusion coefficient [cm²/s]*
c_b .... *bulk concentration [mol/cm³]*
δ_s............. *thickness of the diffusion layer [cm]*

To know the concentration of the species which should be reduced is of importance for applicable pulse plating processes. According to Fick's first law of diffusion, the flux of the cations to the electrode surface depends on the concentration gradient at the electrode surface. If parameters like pulse current density or limiting current density should be controlled during the pulse plating process, the concentration must be calculated in advance

Therefore, the reaction mechanism has to be considered. The diffusion coefficient strongly depends on the concentration of the active ions. The diffusion coefficient can be experimentally determined and compared to theoretical values.

One possible way to determine the diffusion coefficient is to perform chronopotentiometry.[52] In this type of experiment, the current flowing in the cell is instantaneously stepped from zero to some finite value, i.e. the overall reaction rate is fixed, and the potential of the working electrode is then monitored as a function of time. As the flux of the reaction species to the surface of the electrode is getting lower at a certain potential value over time, the potential jumps to a more negative value to where a second reduction process can occur. This enables a stable current flow. The time the concentration needs to reaches zero and the potential transition occurs, is the transition time.[52] The flux of the active species to the electrode surface can be limited by mass transport like diffusion. If the reaction is diffusion controlled, the Sand law is obeyed and the diffusion coefficient can be calculated from the equation (11) [53]:

$$i \cdot \sqrt{\tau} = \frac{1}{2} \cdot z \cdot F \cdot A \cdot \sqrt{\pi \cdot D} \cdot c_0 \tag{11}$$

i............... *applied current [A]*
τ.............. *transition time [s]*
z.............. *number of electrons transferred per ion*
F .... *Faraday constant, 96485 [C/mol]*
A.............. *electrode area [cm²]*
D .... *diffusion coefficient [cm²/s]*
c_0............. *bulk concentration [mol/cm³]*

Another method to measure the diffusion coefficient is by rotating disk electrode (RDE) voltammetry. The limiting current measured for different rotational rates can be plotted against the square root of the rotational rate. The corresponding expression is known as the Levich equation (12). It is a test, whether the current is diffusion controlled or not. If the plot *i* vs. $\omega^{1/2}$ is linear and passes through the origin, the current is entirely controlled by diffusion.[53] The slope of such a plot can be used to calculate the diffusion coefficient of the electroactive species.

$$i_{\mathrm{L}} = 0.620 \cdot z \cdot F \cdot A \cdot D^{2/3} \cdot \omega^{1/2} \cdot \upsilon^{-(1/6)} \cdot c \tag{12}$$

i_{L}............. *Levich current [A]*
z.............. *number of electrons transferred per molecule or ion*
F .... *Faraday constant, 96485 [C/mol]*
A.............. *electrode area [cm²]*
D .... *diffusion coefficient [cm ²/s]*
ω .... *angular rotation rate of the electrode [rad/s]*
υ.............. *kinematic viscosity [cm²/s]*
c.............. *bulk concentration of analyte [mol/cm³]*

The Levich equation is fulfilled with the proportionality of *i* vs. $\omega^{1/2}$. The system is reversible and diffusion controlled. If the proportionality is not given, the electrode reaction rate is not controlled by diffusion but rather limited by another elementary step, e.g. electron transfer or coupled chemical reactions. It can be determined if the redox process is kinetically limited with the plot of $\frac{1}{i}$ vs $\frac{1}{\omega^{1/2}}$ known as Koutecky-Levich plot, which follows the Koutecky-Levich equation (13) [50]:

$$\frac{1}{i} = \frac{1}{i_K} + \frac{1}{0.62 \cdot F \cdot z \cdot D^{2/3} \cdot \nu^{-(1/6)} \cdot c \cdot \omega^{1/2}} \tag{13}$$

where *i* is the measured current, i_K the kinetically controlled current and the second term describes the mass transport. The i_K would be obtained for infinite rotation speed where mass transfer would be so efficient that the surface concentration c would be equal to the bulk concentration. The plot $\frac{1}{i}$ vs $\frac{1}{\omega^{1/2}}$ should be linear and the intercept of the linear regression line with the y-axis equals i_K:

$$\frac{1}{i_K} = \frac{1}{z \cdot F \cdot k \cdot c} \tag{14}$$

i_K............. *kinetic current [A]*

z.............. *number of electrons transferred per ion*

F .... *Faraday constant, 96485 [C/mol]*

k.............. *reaction rate constant [cm/s]*

c.............. *concentration [mol/cm^3]*

From the experimental slope of the Koutecky-Levich plot the diffusion coefficient of the reacting species in the electrolyte can be determined.

In cyclic voltammetry where the electrode is not rotating, for reversible diffusion-controlled electron transfer reaction the peak current i_p increases linearly with the square root of the scan rate which is described by the Randles-Sevcik equation (15) [54]:

$$i_p = 0.4463 \cdot z \cdot F \cdot A \cdot c \cdot \left(\frac{z \cdot F \cdot \nu \cdot D}{R \cdot T}\right)^{\frac{1}{2}} \tag{15}$$

i_p............. *peak current [A]*

z.............. *number of electrons transferred per ion*

F .... *Faraday constant, 96485 [C/mol]*

A .... *electrode area [cm^2]*

c.............. *bulk concentration [mol/cm^3]*

ν.............. *scan rate [V/s]*

R .... *gas constant 8.314 [J/(mol·K)]*

T.............. *temperature [K]*
D .... *diffusion coefficient [cm²/s]*

Therefore, a plot of i_p vs. $v^{1/2}$ should be linear and pass through the origin if the system is reversible and has fast kinetics. This means, the electron transfer rates at all potentials are significantly greater than the rate of mass transport. From the slope of the fitted data the diffusion coefficient may be estimated.

The potential sweep techniques, like cyclic voltammetry, indicate the potentials at which electrode processes occur. As already mentioned, the corresponding peak currents can be analysed with for example the Randles-Sevcik equation. The quality of the information gained from the data analysis depends on the experimental quality of the performed potential sweep techniques. If there is a difference between the applied and the actual potential of the working electrode, because of the high resistance of the electrolyte, reactions occur at lower rate. For example, by sweeping the potential in cathodic direction, the electrolyte resistance between the working and the refence electrode can cause a potential drop also called iR_u drop. This leads to a less negative actual potential compared to the measured one. Consequently, the correlation between the measured peak potential and the measured peak current is erroneous. The resistance of the electrolyte between the WE and RE, which is the reason for the difficulty in controlling the electrode potential, can be minimized by *iR* drop correction or compensation. During the measurement, the resistance can be compensated via automatic resistance compensation of programmable potentiostats. By minimizing the *iR* drop during voltammetric measurements, the obtained data of the analysed system contain less artefacts and the electrochemical analysis will be more precise.

1.5 Aim of this thesis

The aim of this thesis is to electrodeposit compact, homogeneous and dendrite free Al from the DES $AlCl_3$:urea with a molar ratio of 1.5:1 via pulsed current for the use in the charging process of secondary aluminum batteries. The morphology of the deposited Al-layers are influenced by the ratio of the deposition current to limiting current. Therefore, the limiting current needs to be determined. The diffusion coefficient of the active species $[Al_2Cl_7]^-$ is necessary to calculate the diffusion limited current. In the first step, the electrolyte is characterized via potential sweep voltammetry. The obtained data is analysed regarding the Randles-Sevcik equation for cyclic voltammetry, and the Levich and Koutecky-Levich equation for RDE voltammetry to determine the diffusion coefficient. The limiting current will then be estimated. The direct current and pulsed deposition parameters are varied in regard of the ratio deposition current to limiting current to enable a homogeneous and dendrite free Al morphology on copper substrates.

2 Experimental methodology

2.1 Preparational steps

2.1.1 Preparation of electrolyte

The preparation of the electrolyte Uralumina 150 was carried out in an argon-filled glovebox (GS Glovebox Systemtechnik Alpha) with water and oxygen contents below 1 ppm. Anhydrous aluminium chloride (abcr GmbH, aluminum chloride anhydrous, 99.99 %) together with dried urea (SIGMA-ALDRICH, urea 99.5 %) was transferred into the glovebox. Before that, urea was dried in an oven (Heraeus) at 80 °C for 24 hours. The two solid components were mixed together in a 1.5:1 $AlCl_3$:urea molar ratio and stirred with a glass rod until a transparent liquid had formed at room temperature The mixing process must be slow to avoid electrolyte decomposition due to the exothermal reaction. The mixture was further stirred with a magnetic stir bar overnight to produce the liquid deep eutectic solvent (Fig. 4).

Fig. 4: The deep eutectic solvent Uralumina 150 in a glass vial. The electrolyte is prepared in an argon filled glovebox to prevent hydrolysis. The electrolyte is liquid at room temperature.

2.1.2 Preparation of electrodes

Different working electrodes (WE) were used in different cell setups. The first step was to clean their surfaces before use. Pt and GC working electrodes for the three-electrode glass cell setup were polished manually using a Metrohm polishing set (Metrohm Polishing Set 62802000), of Al_2O_3 powder with particle size of 0.3 µm and a polishing cloth. Outside the glovebox, Al_2O_3 was mixed with water to form a slurry. The electrodes were polished in circular motions for a few minutes to remove impurities. Afterwards, the electrodes were fully rinsed with deionized water to get rid of the polishing slurry and dried in an oven at 70 °C. Inside the glovebox, the electrodes were polished in between different measurements with the same Metrohm polishing set. Instead of water diglyme (SIGMA-ALDRICH diethylene glycol dimethyl ether, anhydrous 99.5 %) was used to form the slurry.

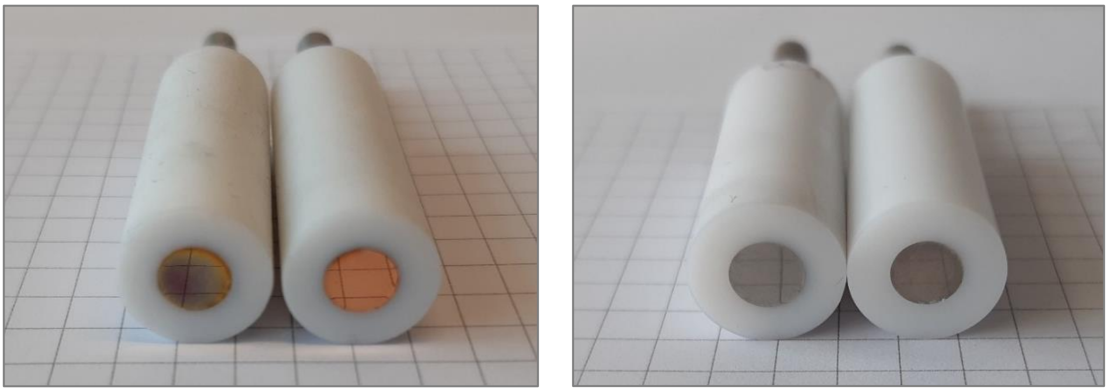

(a) (b)

Fig. 5: Influence of the grinding and polishing step on the electrodes used in Swagelok cells. a) There is a polished (right) and not polished (left) Cu working electrode compared with each other. b) Comparison of the Al metal conus polished (left) and not polished (right) in Al working electrode.

The Cu and Al electrodes used in the three-electrode glass cell and the Swagelok cell were ground and polished mechanically. The Struers grinding devices (Struers LaboPol-25 & Struers LaboForce-1) together with Struers SiC grinding plates for wet grinding were used for this purpose. Each electrode was ground on plate #P1200 (15 µm particle size) for a few minutes, followed by #P2400 (8 µm particle size) for 20 minutes and again #P4000 (5 µm particle size) for 20 minutes. For polishing, the Struers MD-Mol Polishing Cloth 100 % wool was used together with Struers DP-Lubricant Red and Struers DP-Suspension P Ø 3 µm diamond grinding and polishing suspension. Each electrode was polished for 10 minutes and until the surface had a mirror-like finish (Fig. 5). To remove residues from the polishing liquids the Al and Cu electrodes were cleaned with soap and rinsed with distilled water. Only the Al electrodes were sonicated in an ultrasound bath (Emag Germany emmi-4®) in ethanol (ROTH Ethanol 96 %) for five minutes, followed by a rinse with deionized water before they were dried in the oven for 48 h prior use.
To remove the residual oxide from the Cu electrodes, after the cleaning step with soap, they were tipped into 1 M H_2SO_4 for 1 minute, rinsed thoroughly with distilled water and cleaned with EtOH before they were immediately transferred into the glovebox.

2.2 Electrochemical apparatus

To analyse the Uralumina 150 electrolyte by cyclic voltammetry and RDE voltammetry, a three-electrode glass cell setup inside the glovebox was necessary. The electrochemical characterization was followed by assembling Swagelok cells to perform direct current (DC) and pulsed current deposition of aluminum on Cu as electrode material.

2.2.1 Three electrode setup in glass cells

The electrochemical measurements were carried out in a three-electrode glass cell setup (Fig. 6) in the glovebox.

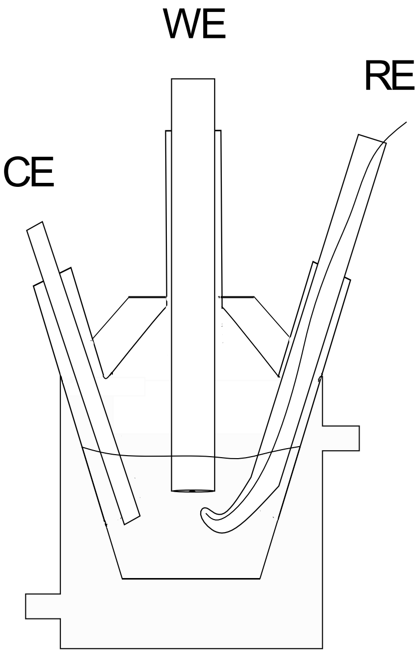

Fig. 6: Three-electrode glass cell setup. In the middle of the glass cell is the working electrode, on the left side is the aluminum foil as counter electrode and on the right side, there is the aluminum wire as reference electrode in a Luggin-capillary. The tip of the Luggin-capillary is positioned near the surface of the WE.

The glass cell was filled with Uralumina 150 until the tip of the WE dipped into the electrolyte. The polished WE was positioned in the middle of the cell as stationary or rotating disk assembly. For rotating the electrode, a scientific instrument from Princeton Applied Research (PAR) was used. The details regarding the used working electrodes are summarized in *Table 1*. As counter electrode, aluminum foil was positioned next to the WE. The aluminum foil was cleaned with EtOH and distilled water, dried at 70 °C before transferred into the glovebox. To control the potential of the WE versus the reference, the cell was equipped with an aluminum wire (ADVENT research materials, aluminium wire 99.999 %, Ø 1.0 mm). The tip of the RE was polished with very fine abrasive paper inside the glovebox in order to remove possible oxides on the aluminum surface. The tip of the Luggin-capillary was positioned around 1-2 mm from the surface of the working electrode. The small distance between RE and WE was crucial for the quality of the electrochemical measurements due to the high resistance of the electrolyte. All electrochemical measurements were carried out with a Metrohm Autolab Potentiostat/Galvanostat PGSTAT100 controlled by Nova 1.1 software.

Table 1: Overview of the working electrodes

Disk material	Ø	A [cm²]	Sheath	Manufacturer	Use
GC	3 mm	0.071	PEEK	Metrohm	glass cell stationary
Pt	4 mm	0.12	PTFE	PAR	glass cell rotating
Pt	3 mm	0.071	PEEK	Metrohm	glass cell stationary
Cu	3 mm	0.071	PTFE	Metrohm	glass cell stationary
Cu	6 mm	0.28	PTFE	TU Graz	Swagelok cell
Al	6 mm	0.28	PTFE	TU Graz	Swagelok cell
Al	3 mm	0.07	PTFE	Metrohm	glass cell stationary

Coulombic efficiency

The coulombic efficiencies were investigated using the three-electrode glass cell setup. Therefore, the plating and stripping process of aluminum from the electrolyte onto the surface of the working electrode was performed via cyclic voltammetry. The CEffs were calculated [eq. (16)] based on the amount of electric charge used during dissolution (stripping process) divided by the amount of electric charge consumed for deposition of aluminum onto the working electrode surface:

$$CE_{ff} = \frac{Q_{discharge}}{Q_{charge}} \cdot 100 \tag{16}$$

Q .... charge [C]

2.2.2 Uncompensated resistance – the *iR* drop

The moderate to low conductivities of DES as electrolyte media can affect the results of electrochemical measurements performed in these non-aqueous electrolytes.

In a classical three-electrode setup the reference electrode (RE) is needed for measuring and controlling the potential of the working electrode (WE) and is connected via a Luggin-capillary to the electrolyte. The distance between the tip of the Luggin-capillary and the chemically active surface area of the WE should be as small as possible. The smallest distance should be two times the outer diameter of Luggin-capillary roughly, to not disturb the diffusion processes close to the working electrode. Otherwise, the solution current path at the working electrode can be blocked due to shielding processes, which causes nonuniform current densities at the electrode surface.[52][55] Even though the distance between the reference electrode and WE is very small, there is a drop in the potential. The resistance between the tip of the Luggin-capillary and the surface of the WE is called uncompensated solution resistance R_u (Fig. 7).

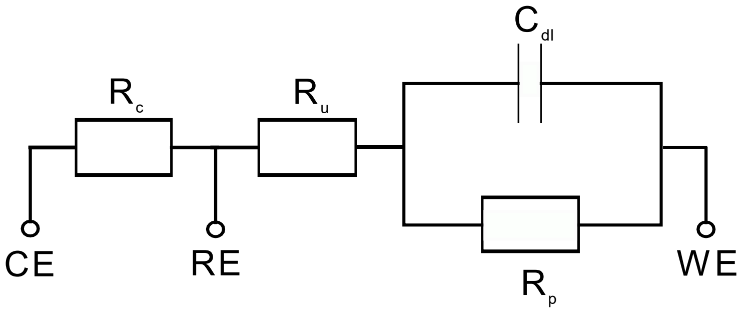

Fig. 7: Electrical equivalent circuit of the test cell with three electrode set up. The first resistance R_c is the *resistance of the current path, followed by* R_u *which is the uncompensated resistance and* R_p *is the polarization resistance of the working electrode.* C_{dl} *is the doubler layer capacity of the working electrode.*

It mainly comes from the resistance of the electrolyte, next to the minimal resistance of the electrode material. This resistance R_u reduces the actual polarization potential E_p of the WE in relation to the applied potential E_a according to equation (17):

$$E_\mathrm{p} = E_\mathrm{a} - iR_\mathrm{u} \tag{17}$$

The product of polarization current *i* and R_u is called ohmic drop or potential drop [eq. (18)]:

$$E_\mathrm{u} = iR_u \tag{18}$$

If a cathodic current flows, the true potential of the working electrode is less negative than the specified potential. The opposite holds in the case of an anodic current. The problem of the iR_u drop and its compensation is well known and has worried electrochemists over a long period of time.[56]

To minimize the R_u value, good cell design is of importance, the conductivity of the electrolyte solution can be increased with additional non-reactive supporting electrolyte. Reducing the size of the working electrode can help reduce the iR_u drop. For example, at microelectrodes with a surface area in µm range, the currents are extremely small. This leads consequently to a decrease in potential control error compared to the same experiment with an electrode of macroscopic size.[52]

Before the start of the actual electrochemical measurement, the iR_u drop for the used experimental setup including the electrolyte, the WE and the RE can be calculated in advance [eq. (19)] [56]:

$$R_{\mathrm{u}} = \frac{arctan\frac{l}{r}}{2 \cdot \pi \cdot \kappa \cdot r} \tag{19}$$

l .... *distance between the working electrode and the Luggin-capillary*
r .... *radius of the circular working electrode*
κ.............. *specific conductivity of the electrolyte*

Based on the calculated R_u values, the necessity of any iR_u compensation can be evaluated. For the quality of the results, it is important that no surface layers are present or formed on the WE during the measurement and that the conductivity of the electrolyte remains constant during the whole experiment.

Furthermore, the experimental determination of the iR_u drop can be done by e.g. impedance measurements, the current interrupt method or the positive feedback method.

For this work the *i*-interrupt measurement was performed in the Uralumina 150 electrolyte with Al and GC as working electrodes in the three-electrode glass cell. The impact of high resistance of the electrolyte onto the measured potential was minimized by reducing the distance between WE and RE to a minimum of around 1 mm during these measurements, and all cyclic voltammetric measurements were performed in the three-electrode glass cell.

For the first measurements with Al and GC as working electrodes, it was not possible to determine the uncompensated resistance.

Usually after the interruption, the measured potential decreases immediately when the ohmic voltage drop iR_u disappears, while the “true” polarization voltage E_p of the working electrode only decreases slowly due to the storage capacity of the double layer. The potential of the Al and GC electrodes remained constant during the time of the measurement, which was unexpected (Fig. 8).

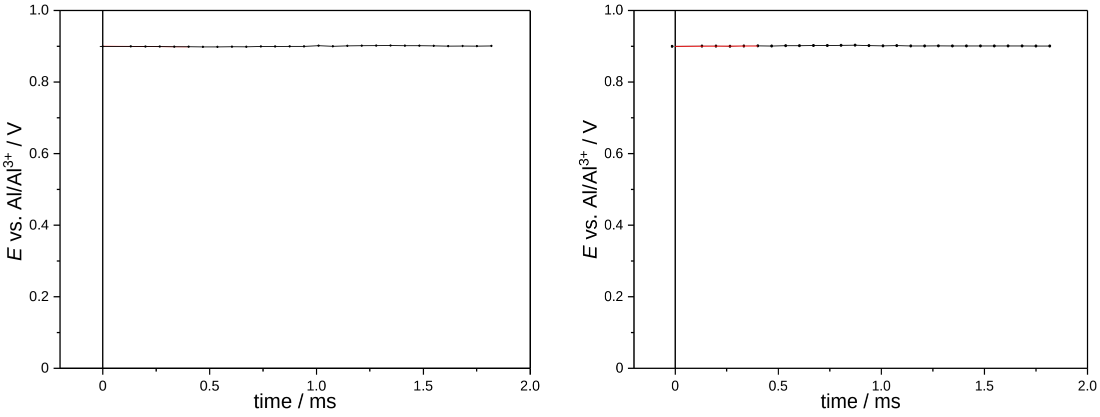

(a) (b)

Fig. 8: I-interrupt method using Al and GC working electrodes. In a) is the chronopotentiogram of the Al WE. No decrease in the potential of the working electrode can be seen. In b) also no potential drop during the chronopotentiometry of the GC working electrode appeared.

With Pt, the *i*-interrupt measurement was successful and the potential of the working electrode decreased after the polarization current was interrupted. If the voltage of the cell is measured immediately before and immediately after the current has been interrupted, the difference in the measured voltages is the ohmic drop. The ohmic drop divided by the known current before the interruption gives the ohmic resistance R. The resistance values obtained from the data are reported in the Autolab display. Different potentials were applied, ranging from +1.1 V to −1.1 V vs. $\mathrm{Al/Al^{3+}}$ to see if it has an impact on the obtained resistance values. The progress of the potential after the interruption is shown in Fig. 9. The evaluated R_u was 833 ± 218 ohm and varied depending on the applied potential. For the calculation the average ohmic values obtained from the potential variations seen in Fig. 9 are used. The resistance values based on measurement with the potential −0.2 V and +0.2 V are not used in the calculation, due to the high difference to the other values. The evaluated R_u incl. ± 2 V would be 883 ± 248 ohm.

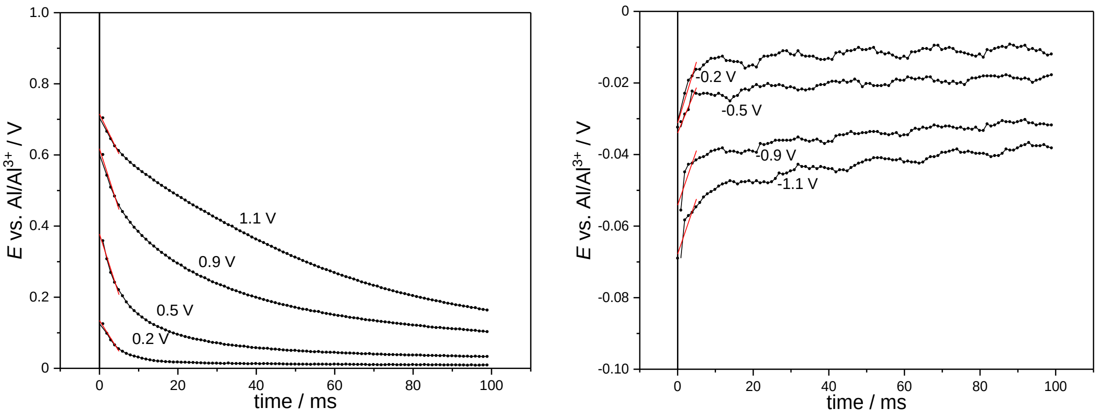

(a) (b)

Fig. 9: Current-interrupt method on Pt WE in a) positive potential range and b) negative potential range. Different potentials were applied ranging from +1.1 V to -1.1 V.

Another way to determine the uncompensated electrolyte resistance is the positive feedback method. It is based on the control of the potential of the working electrode vs. the RE by adjusting the current flow. The necessary current response depends on the actual values of the uncompensated resistance and the double layer capacitance. If the ohmic resistance causes a potential control error it can be corrected by a correction voltage proportional to the current flow. The compensation of R should be less than 100 % because otherwise the potentiostat will start to oscillate.[53]

Here, the potential was stepped from 0 V to 0.1 V and back to 0 V. Each potential was held for 5 seconds. The responding curve starts to change when the ohmic resistance is compensated. Different amounts of resistance were compensated and the results can be seen in Fig. 10. The higher the percentage of compensated resistance the more intense is the oscillation of the potentiostat like illustrated in Fig. 10 d). The manufacturer of the potentiostat recommends compensating around 90 % of the internal resistance, to prevent oscillation. For these measurements a Pt WE was used.

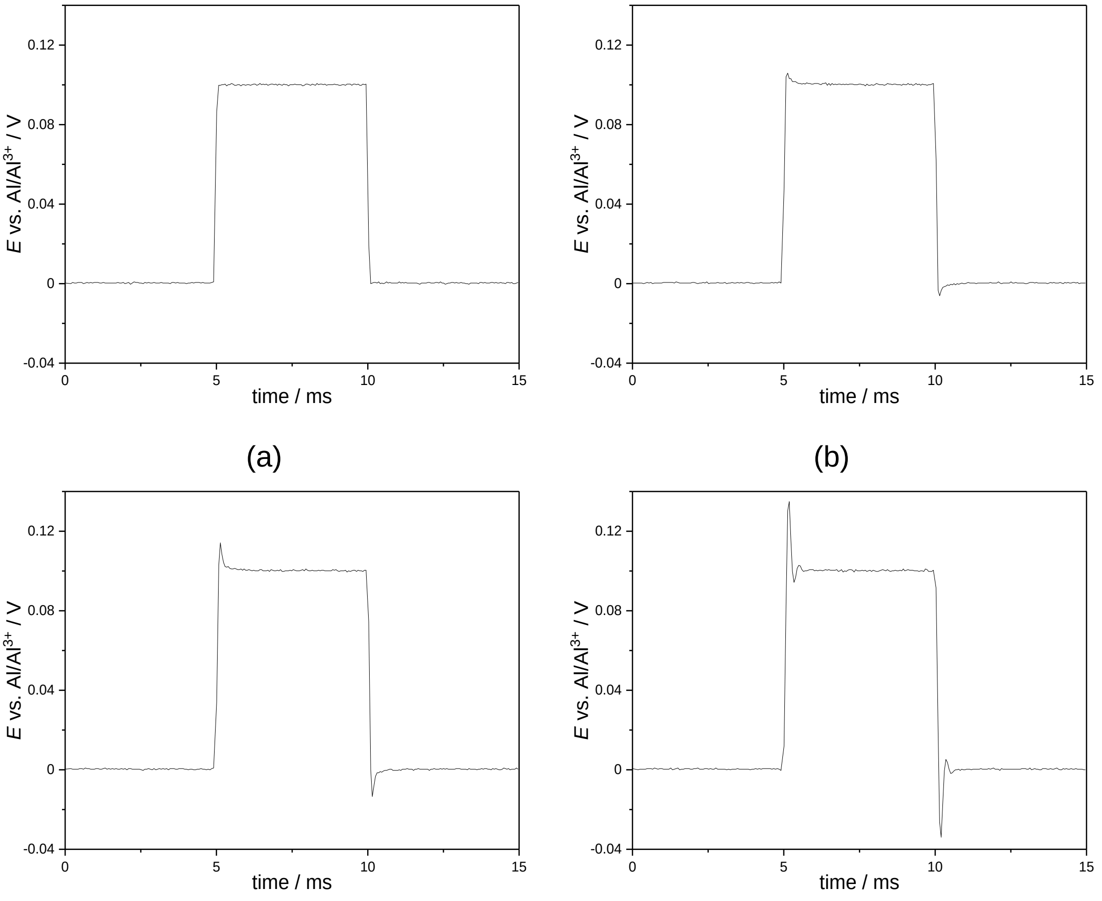

(a) (b)

(c) (d)

Fig. 10: Measured data obtained from positive feedback method on Pt WE. By increasing the extent of the resistance compensation from a) 0 % to d) 90 %, the potential of the working electrode starts to respond by little oscillating waves at the beginning and the end of the current pulse. In detail the resistance compensation is a) 0 Ω b) 1300 Ω c) 1350 Ω d) 1400 Ω.

Once the resistance R_u has been measured or computed according to one of the above described methods, the measured current-potential curves can be corrected afterwards by subtracting the ohmic drop for each measured current data point from the corresponding potential values.[57]

If the iR_u drop should be compensated during the measurement, a few potentiostatic methods are possible, namely compensation by positive feedback, compensation by current interrupt methods or compensation by negative resistance and alternating current methods.

In potentiodynamic experiments, the automatic iR_u drop correction is of enormous importance, due to the effect of the iR_u drop on the actual scan rate.[56]

2.2.3 **Swagelok cells**

Symmetrical aluminum half-cell batteries were assembled to perform DC and pulsed aluminum deposition (*Fig. 11*).

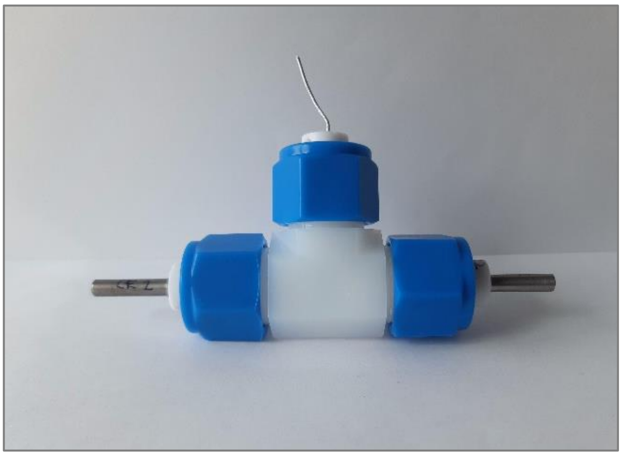

Fig. 11: The assembled Swagelok cell with reference electrode in the middle between counter electrode and working electrode.

The body of the Swagelok cells are so called T-fittings made from PFA (perfluoroalkoxy alkanes). The deposition was performed on Cu as working electrode material. The working and counter electrode (Al as electrode material) were positioned 3 mm apart from each other. In Fig. 12 the construction of the electrodes can be seen. The reference electrode consisting of an aluminum wire was positioned in the middle of the two electrodes. The electrodes were prepared as described in chapter 2.1.2. Additionally, the aluminum wire was ground before assembly in the cell to remove the oxide layer. The cell was filled with 1 ml of Uralumina 150 electrolyte and closed tightly.

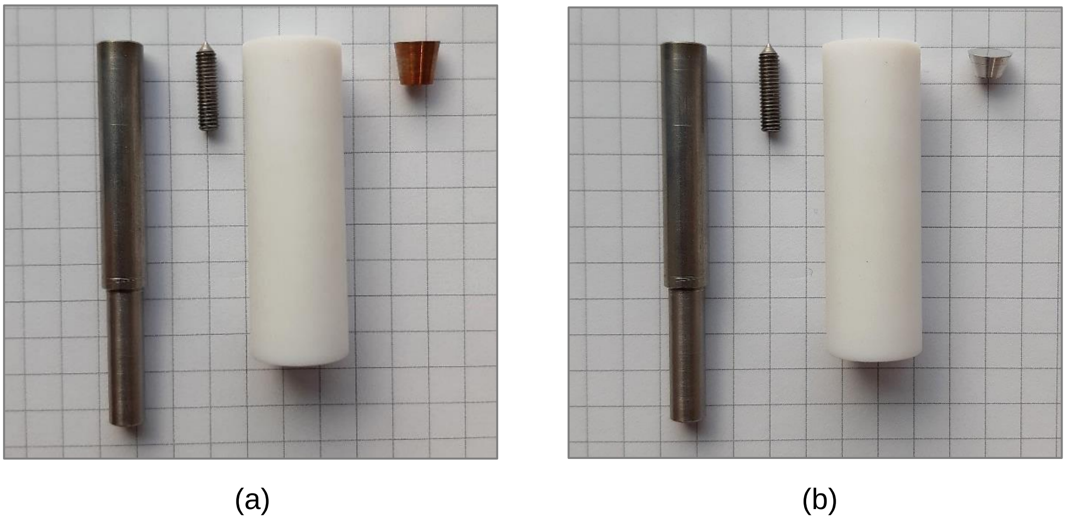

(a) (b)

Fig. 12: Electrode set up of electrodes used in Swagelok cells. On the right side of each picture is the metal conus a) copper and b) aluminum together with the cell body of PTFE material and the electrically conductive metal contact for connection to the potentiostat or galvanostat.

The charging half-cycle was performed using the battery test system BaSyTec CTS LAB XL and the software BaSyTec V 6.1.2.1/BDE. For five cells, the deposition was performed with direct current, followed by 5 cells, where different pulse parameters were varied. After the deposition, the cells were disassembled inside the glovebox and the electrodes carefully rinsed with acetonitrile to remove the electrolyte. Afterwards, scanning electron microscopy (SEM) was performed to analyse the morphology of the deposits. The SEM images were taken with a Zeiss Sigma 300 VP microscope (software SmartSEM Version 6.01) equipped with an in-lens and an Everhart-Thornley secondary electron detector. EDS spectra were acquired with an Oxford SDD 80 EDS detector. EDX analysis was carried out with a Zeiss Sigma 300 VP microscope in combination with an Oxford SDD 80 EDS Detector (software AZTEC 3.4).

Electrochemical impedance spectroscopy

Further Swagelok cells were assembled to carry out electrochemical impedance measurements for determining the resistance of the electrolyte and to calculate the electrical conductivity.

As WE, RE and CE aluminum was used and the cell was loaded with 1 ml of Uralumina 150.

The measurement was performed outside the glovebox using a Zahner IM6 12079 with software Thales Z2.29 USB. The measurements were carried out four times in a frequency range from 100 kHz - 100 mHz (*Fig. 1A, 2A, 3A, 4A*) followed by a single measurement with frequencies ranging from 100 kHz - 1 mHz (*Fig. 5A*). They started at the open cell potential of 0 V vs. Al/Al^{3+}.

The resistance based on the five measurements was 565 ± 131 ohm.

To calculate the electrical conductivity based on the measured resistance of the electrolyte, the formula (20) was used:

$$\sigma = \frac{1}{R} \cdot \frac{L}{A} \tag{20}$$

σ.............. *electrical conductivity of electrolyte [S/cm]*
R .... *resistance [ohm]*
L.............. *distance between WE and CE [cm]*
A.............. *area of the working electrode [cm²]*

The electrical conductivity based on the internal resistance is 0.75 ± 0.19 mS/cm, which is also reported in the literature. [25]

3 Results and discussion

3.1 Characterization of the electrolyte

3.1.1 Cyclic voltammetry

i) *<u>Influence of the iR drop on cyclic voltammetry in Uralumina 150</u>*

The cyclic voltammograms of different working electrodes (GC, Pt, Cu) recorded in the deep eutectic solvent $AlCl_3$:urea with the molar ratio of 1.5:1 are discussed in this section. The goal was to determine the influence of the *iR* drop on the actual shape of the CVs and how to compensate the ohmic potential drop in this specific electrolyte to obtain reliable data.

In Lewis acidic $AlCl_3$:urea mixtures with an excess of $AlCl_3$, there are $[Al_2Cl_7]^-$ ions, which can be reduced to metallic aluminum at room temperature in a specific potential range [equation (3)].[45]

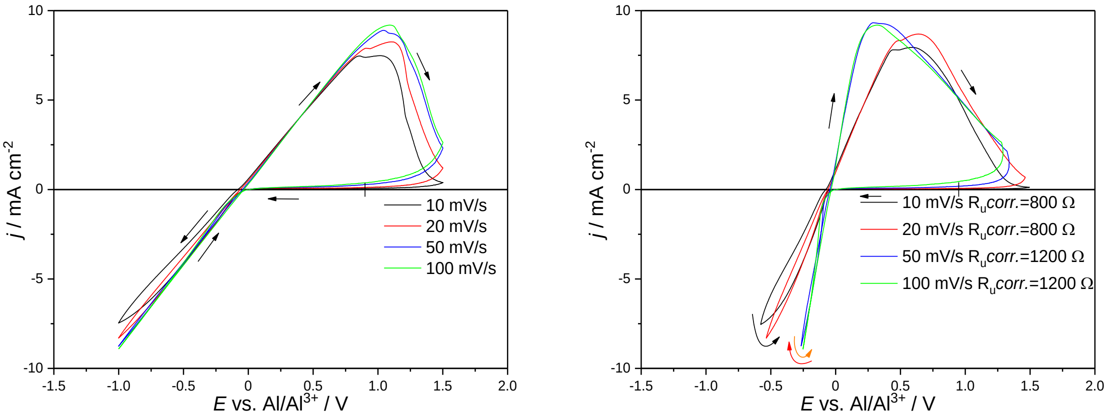

(a) (b)

Fig. 13: CVs at glassy carbon working electrode with scan rates of 10 mV/s, 20 mV/s, 50 mV/s and 100 mV/s. a) The original measured CV and b) the CV corrected by the product of the internal resistance and the polarization current (iR_u drop) via software after the measurement.

All the cyclic voltammograms in Fig. 13 a) show a typical curve of the deposition and dissolution of aluminium on a glassy carbon working electrode. The CVs are obtained for various scan rates ranging from 10 to 100 mV/s at RT. The potential window in which the potential was swept ranged from –1 to 1.5 V vs. Al/Al^{3+}. The scan started in cathodic direction at the open circuit potential of 0.9 V vs. Al/Al^{3+}. The reduction of the electroactive aluminum species starts around –0.1 V vs. Al/Al^{3+}. The reduction process starts normally with an overpotential at the working electrode to enable the nucleation and growth of aluminum nuclei on the blank substrate surface. If the deposited Al is not fully dissolved in the anodic sweep, the nucleation overpotential was close to 0 V, due to the already existing growth sites (see Fig. 18).

Nevertheless, the overpotential value was very low on the glassy carbon working electrode.

The current density increased linearly in the cathodic potential range and proceeded without apparent deposition peaks. By comparing the cathodic current densities of different scan rates, there is no clear relation to see. In in theory, there is a relation between the scan rate and the measuring current. The cathodic current densities increased slightly with increased scan rate.

Fig. 13 b) shows the same CV curves with the GC electrode but after iR_u drop correction. The iR_u drop was corrected with the software Nova 1.11 by Autolab for each scan rate individually. For the first two scan rates 10 mV/s and 20 mV/s a correction of 800 ohms was possible. The scan rates 50 mV/s and 100 mV/s were corrected with 1200 ohms. The effect of the iR_u drop correction was the shift of the measured potentials by iR_u according to equation (17). The product of the uncompensated resistance and polarization current iR_u or E_u, reduces the actual polarization potential of the working electrode in relation to the applied potential. Therefore, the true potential is less negative than the measured one in the cathodic potential range. The same goes for anodic potential range. The measured potential in Fig. 13 a) consist of the actual (true) potential plus E_u. Therefore, before the correction the cathodic switching potential is higher and after the correction, the cathodic switching potential is lower. The anodic switching potential stays at +1.5 V but the max. current density measured at +1.1 V shifted to +0.6 V and lower in dependence of the scan rate after the correction.

In Fig. 14 CVs are performed at a scan rate of 100 mV/s on the GC working electrode. All scans started at open circuit potential of 0.9 V vs. Al/Al^{3+} in cathodic direction. The difference between Fig. 14 a) and b) is the way of iR drop compensation. In a) the ohmic drop was compensated during the measurement via the potentiostat (hardware), whereas in b) the iR drop was corrected mathematically after the measurement by subtracting E_u from E_a. For good comparison, the same resistance values were chosen.

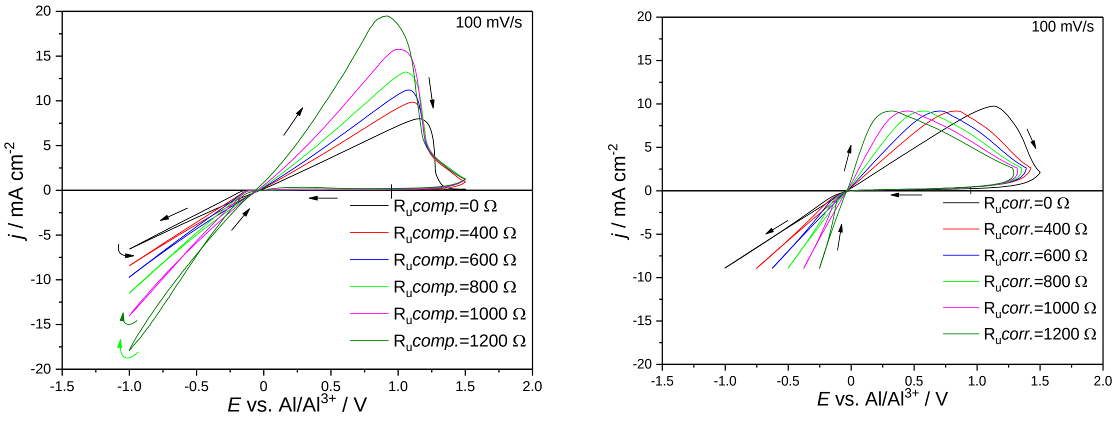

(a) (b)

Fig. 14: CVs on GC working electrode at a scan rate of 100 mV/s and a) iR drop compensation during the measurement or b) mathematical iR drop correction after the measurement via Nova 1.11 software. Different resistance values are compensated to see the influence of the potential drop on the CV shape.

As clearly visible, the shape of the curves and peak values (potential and current densities) look remarkably different. For the *iR* drop compensation during the measurement, the switching potential remains constant at –1 V vs. Al/Al^{3+}. If the automatic compensation of E_u compensates all of the *iR* drop, the system would reach the potential the potentiostat is applying, like $E_p = E_a$. The current values at the switching potential increased from around –7 mA/cm^2 at no *iR* compensation to around –18 mA/cm^2 with 1200 ohm for *iR* drop compensation. The same goes for the anodic peak current densities which rises from 7 mA/cm^2 (no resistance is compensated) to 19 mA/cm (1200 ohms compensated). The anodic peak potential shifted from 1.2 V to 0.9 V vs. Al/Al^{3+}. In comparison, the CVs in b) were corrected mathematically after the measurement. It is clearly visible that the switching potential is shifted to less negative values, from –1 V to –0.2 V vs. Al/Al^{3+}. The current densities at the switching potentials remained constant at –9 mA/cm^2.

Based on this information, the *iR* drop correction afterwards just causes a shift of the switching potential to less negative values. The software subtracts the *iR* drop caused by the uncompensated resistance of the electrolyte from the applied potential to achieve the true potential. During the measurement, the *iR* drop is still an issue, due to the erroneous potentials and scan rate, resulting in lower aluminum deposition rates and consequently lower current densities. Whereas, the *iR* drop compensation during the measurement enables the system to perform the deposition and dissolution of aluminum without the artefacts of the ohmic potential drop, caused by the low conductivity of the electrolyte.

As second working electrode, platinum was used as substrate for electrochemical deposition and dissolution of Al from Uralumina 150. The potential scan started at the open circuit potential at 0.8 V vs. Al/Al^{3+} in negative direction to –1 V, back to 1.5 V and ended at the OCP. On Pt as substrate, the nucleation overpotential was around 200 mV and therefore higher than on GC. Four different scan rates were used, 5 mV/s, 10 mV/s, 50 mV/s and 100 mV/s. In Fig. 15 a) the uncompensated CVs performed on Pt as working electrode are shown.

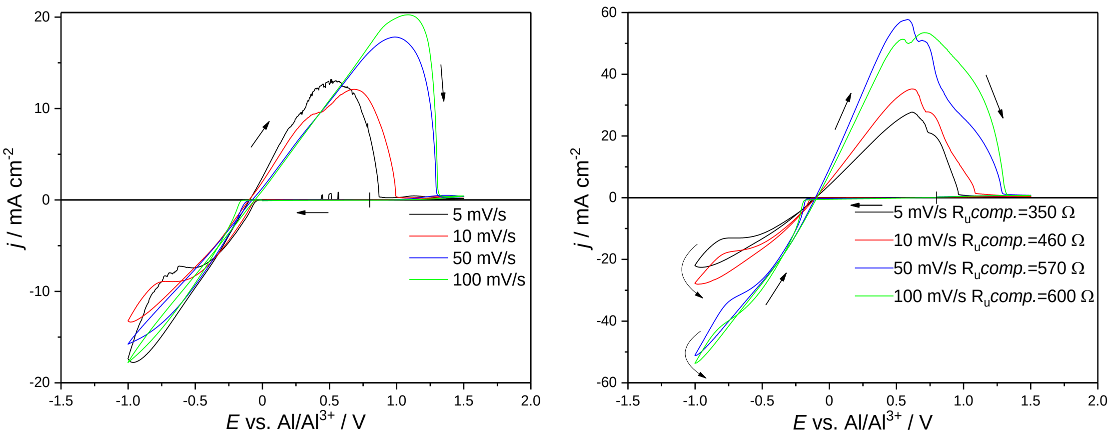

(a) (b)

Fig. 15: CVs on Pt working electrode with scan rates 5 mV/s, 10 mV/s, 50 mV/s and 100 mV/s. In a) the curves measured without iR-drop compensation can be seen and in diagram b) the curves with compensated iR drop are visualized. For each scan rate, the electrolyte resistance was compensated with the max. possible values determined via current interrupt method.

In the cathodic potential range the $[Al_2Cl_7]^-$ species is reduced to Al, followed by the dissolution of Al from the substrate in the anodic potential range.

The influence of the scan rate on the measured current densities at the cathodic switching potential in Fig. 15 a) are little compared to Fig. 15 b). The highest measured current density increased from –13 mA/cm^2 at 10 mV/s to –16 mA/cm^2 at 50 mV/s. The values for the highest current density at 5 mV/s and 100 mV/s are in the same range around –18 mA/cm^2. When the potential was more negative than –0.2 V, Al deposition occurred and proceeded without apparent deposition peaks but with a continuous increase in current density. The second diagram (Fig. 15 b) shows different CV curves, where the ohmic drop was compensated by the potentiostat hardware during the measurement.

For each scan rate, the extent of the ohmic drop compensation was individually decided. At faster scan rates a higher ohmic drop compensation was possible. By lowering the scan rate the possible ohmic drop compensation values deceased. Therefore, the actual potential of the working electrode E_p should match the applied potential E_a in these measurements. By comparing the different CVs in a) and b), it is clearly visible that the current densities increased with the scan rate in b). Without the influence of the ohmic drop the current density increased from −18 mA/cm² to −58 mA/cm² (at 100 mV/s). In b) the scan rate affecting the current density can be observed.

The anodic peak current density rises from 20 mA/cm² in 16 a) to 60 mA/cm² in 16 b) when compensating 600 ohms (100 mV/s). In contrast to the current densities, the coulombic efficiency (CEff) decreases with increasing *iR* drop compensation (*Fig. 6A*). For example, the CEff for the deposition and dissolution of Al on Pt substrate at a scan rate of 100 mV/s is 98.73 % without and 91.04 % with *iR* drop compensation. The values are listed in *Table 2*.

Table 2: Coulombic efficiencies of aluminum deposition

scan rate [mV/s]	CEff	*R* comp. [Ω]	CEff
5	84.59 %	350	77.38 %
10	95.79 %	460	80.61 %
50	99.09 %	570	75.82 %
100	98.73 %	600	91.04 %

The same observation is shown when multi cycle CV is performed with 10 cycles in a row. The cyclic voltammograms are performed with a scan rate of 10 mV/s without Ohmic drop compensation (*Fig. 7A*) and with Ohmic drop compensation (*Fig. 8A*). The results are summed up in *Table 3A*. The same measurements are recorded for a scan rate of 50 mV/s (*Fig. 9A & Fig. 10A*) and the results are summarised in the appendix in *Table 4A*. One reason can be that by compensating the resistance more side reactions occur because of the more negative potentials. Another reason can be the thicker Al layer on the Pt surface due to the more negative WE potential, which is more difficult to dissolve completely during the anodic sweep, which again would lower the CEff.

The third substrate material tested to deposit and strip Al onto was copper. The potential window is −1 to 0.5 V vs. Al/Al^{3+} determined in preliminary tests. The scan started at the open circuit potential of 0.4 V vs. Al/Al^{3+} in cathodic direction. The anodic curve is different compared to the anodic CV curves on glassy carbon (Fig. 13 & Fig. 14) and platinum (Fig. 15). At the Cu WE not all of the deposited aluminum can be stripped from the electrode surface during the anodic scan. When the potential was increased beyond 0.5 V vs. Al/Al^{3+} range, a second peak appeared. This peak could be due to the DES oxidation / decomposition.[58]. More likely is the oxidation or dissolution of Cu. In Fig. 16 the difference between the CV without (a) and the CV with *iR* compensation (b) can be seen. In Fig. 16 a) the ohmic drop does have a strong influence on the shape of the CV. The current density nearly linearly increased with increasing overpotential, especially at higher scan rates.

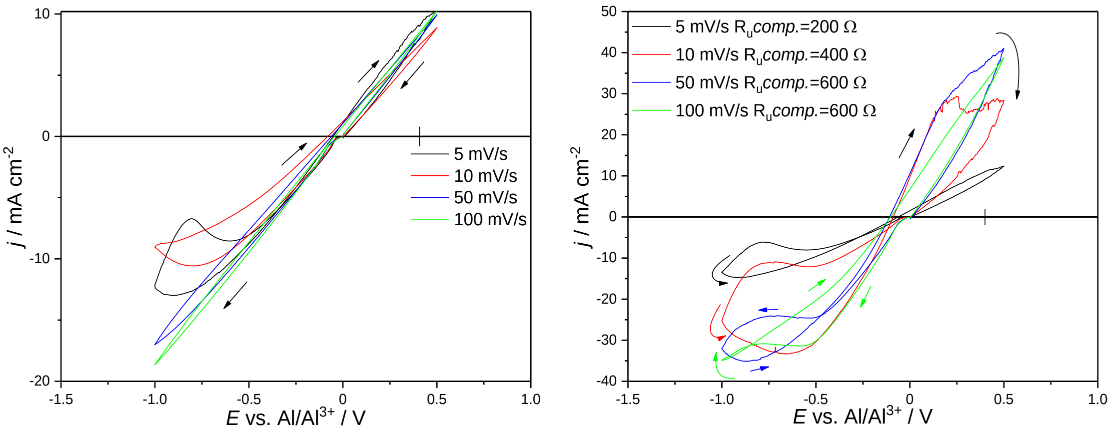

(a) (b)

Fig. 16: CV on Cu working electrode with scran rates of 5 mV/s, 10 mV/s, 50 mV/s and 100 mV/s performed with a) uncompensated iR drop and b) compensated iR drop. The correction of the ohmic drop was performed during the CV measurement. For each scan rate the value of the iR drop compensation was maximized.

For the CV recorded with the scan rate 5 mV/s, there is no difference to the peak current density in the *iR* drop compensated CV in b) (both around 12 mA/cm^2). At higher scan rates like 10 mV/s, 50 mV/s and 100 mV/s, the ohmic resistance clearly influenced the curves, so that no artefact free CV could be recorded without *iR* drop compensation. The *iR* drop compensation during the measurement resulted in broad peaks. In Fig. 16 b) the reduction currents are higher in the reverse sweep compared to the forward scan. For example, at 10 mV/s the current density at –0.6 V is –30 mA/cm (back scan) compared to –11 mA/cm^2 in the forward scan (*Table 1A*). One reason might be the larger surface area due to the deposited Al in the forward scan.

For the deposition of Al on GC no wide peaks were detected. During the Al deposition on Pt some kind of wide peaks were measured. At scan rate 5 mV/s and 10 mV/s there were wider peaks in the forward scan and at scan rate 50 mV/s and 100 mV/s there was a short period of const. current measured in the range of –6 to –8 V vs. Al/ Al^{3+}.

The deposited Al changes the area of the surface throughout the reduction process whereas the geometric electrode area used in the mathematical formula to calculate the current density (mA/cm^2) is fixed at the original value. The stabilization of the current value at wide peaks is a sign for kinetic limitation during deposition process. There are several rate determining steps possible in electrodeposition reactions:

i) mass transfer like diffusion from the bulk to the electrode surface
ii) charge transfer at the metal surface,
iii) nucleation process of the ad-atoms
iv) crystallization of the formed nuclei
v) chemical equilibria of the metal-complexes in the electrolyte

Which or how many of these steps are rate limiting for the electrochemical Al deposition, is hard to tell and needs further research. Therefore, in this thesis some methods are used to determine if the deposition is diffusion controlled or not, followed by the determination of the diffusion coefficient.

It has shown that no current plateau but wide peaks were detectable. One reason can be the continuing deposition of Al and therefore, continuing growth of the active surface area.

The most important results are listed below, to summarise what kind of information is gained so far from cyclic voltammetry in Uralumina 150:

- The GC electrode is not recommended to perform CVs in electrolytes with low conductivity like Uralumina 150. One reason are the difficulties during ohmic drop determination via *i*-interrupt and positive feedback method, which can lead to incorrect ohmic drop compensation (Fig. 8). Another reason are the obtained cyclic voltammograms after *iR* drop compensation. The influence of the ohmic resistance was very clear due to the shape of the curve even though the compensated resistance was already very high (> 1000 Ω).

- Pt as WE material can be recommended based on the performance during the CV. Firstly, the determination of the uncompensated resistance prior to cyclic voltammetry worked as expected. Secondly, the reversible deposition and dissolution of Al onto the substrate worked well and the *iR* drop was easily compensated. In dependence of the scan rate, small peaks were recorded.

- On Cu as WE the Al deposition worked well but for complete dissolution after the deposition step the anodic potential window is too small. Therefore, additional electrode pre-treatment steps are necessary like grinding and polishing before each measurement.

- Additionally, it is to say, that no matter what kind of WE is used, the automatic *iR* drop compensation during the CV is highly recommended. Otherwise, the measurement error can lead to incorrect information gained from the current-potential curves.

ii) *Variation of cathodic switching potential*

During the performance of cyclic voltammetry in Uralumina 150 with Pt as working electrode, there were broad peaks observed. In the tested potential range –1 V to 1.5 V vs. Al/Al^{3+} the peaks had different shapes, depending on the scan rate. To investigate if there is a peak in a more negative cathodic potential range, because of the *iR* drop affecting the measured potential, the potential was swept from the open circuit potential to −5 V and −9 V vs. Al/Al^{3+} and back. All measurements are depicted in Fig. 17.

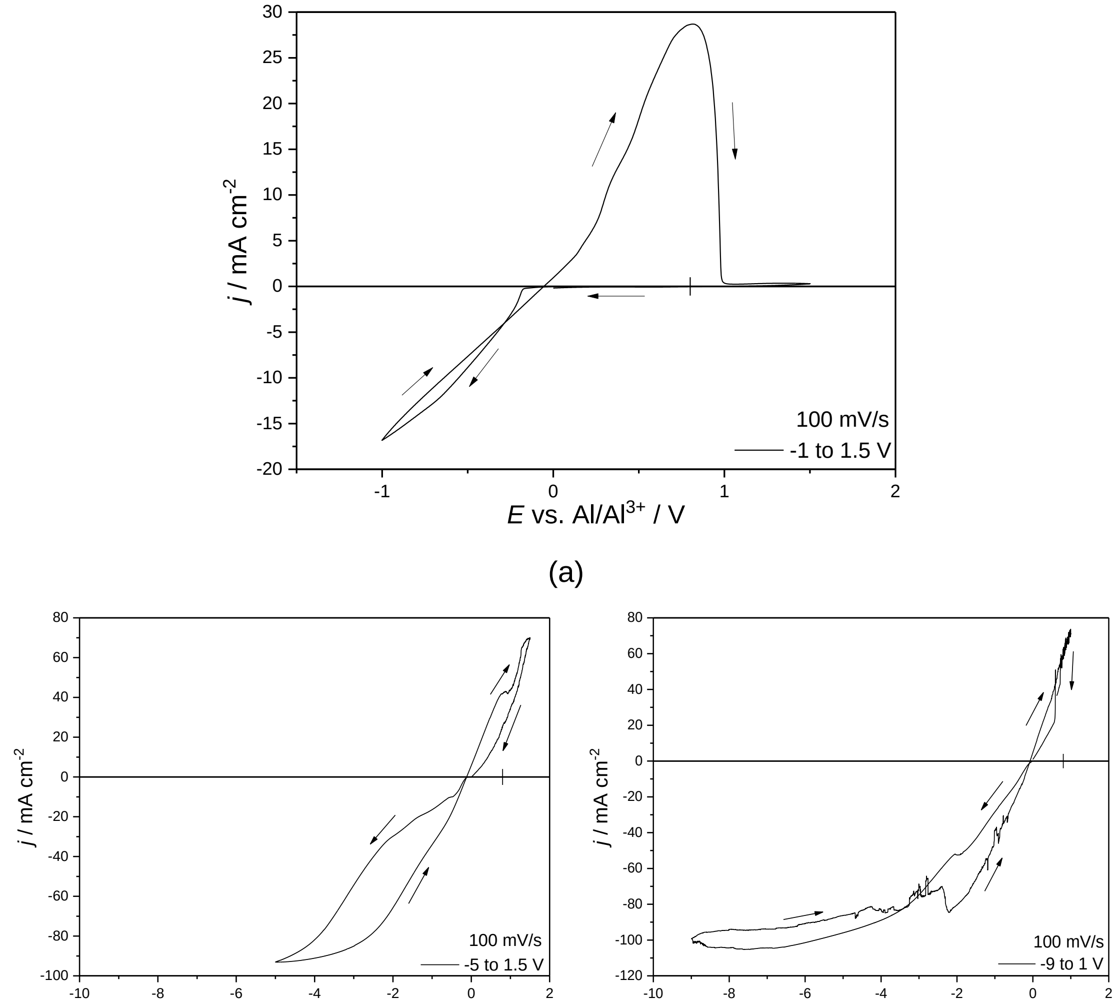

(a)

(b) (c)

Fig. 17: Cyclic voltammograms with different switching potentials for the deposition of aluminum in Uralumina 150 with Pt as working electrode. In diagram a) the CV performed in a potential range between -1 V and 1.5 V vs. Al/Al^{3+} can be seen. In b) the CV performed in a potential range between -5 V and 1.5 V vs. Al/Al^{3+} is visualized. In diagram c) the CV performed in the largest potential range from -9 to 1 V vs. Al/Al^{3+} can be seen. All measurements were performed at a scan rate of 100 mV/s.

In the CV with a cathodic switching potential of −5 V vs. Al/Al^{3+}, the deposition started at a nucleation overpotential of −200 mV. As the potential reached around −4 V the current density seemed to stabilize, but the progress was not completely clear because of the switching potential at −5 V. The anodic sweep of the CV changed the appearance compared to the anodic sweep recorded in previous experiments, for example in Fig. 15.

The reason is that the amount of plated Al was probably too large to remove the metal layer during the anodic potential sweep. Therefore, the curve resembles more a CV recorded on a Cu WE as seen in Fig. 16. To see if there is a peak at even more negative potentials, the cathodic switching potential was extended to −9 V vs. Al/Al^{3+}. Between −4 V and −9 V vs. Al/Al^{3+} the current density stabilized at around −100 mA/cm². The current density in the forward scan was a little bit higher compared to the backward scan. In the anodic sweep, it was not possible to dissolve the deposited Al from the substrate surface completely.

Another essential point of this experiment was the change in colour of the electrolyte. After the first measurement to −5 V vs. Al/Al^{3+} the electrolyte had turned dark in front of the working electrode. It is not clear if the colour change happened during the anodic sweeps or already during the cathodic sweep It can be assumed that some of the stripped Al did not dissolve back into the electrolyte to form $[Al_2Cl_7]^-$ and just detached from the electrode surface. The same happened during the scan to even more negative potential. Hence, the electrolyte is either not stable at more negative potentials and start to decompose or the plated Al does not react back to form $[Al_2Cl_7]^-$ species according to reaction equation (3) after the plating process.

iii) *The nucleation overpotential*

The next topic worthy of discussion is the nucleation overpotential for Al deposition on different electrode materials. The overpotential is necessary for the nucleation and growth process of thermodynamically unstable Al nuclei on the working electrode surface. After the nuclei have reached the critical size, the overpotential causes the particles to grow bigger and to form a layer of Al. If there is no nucleation overpotential seen in the first scan in cathodic direction, it is a sign that the surface of the working electrode is not as clean as it should be. There can be Al particles from previous experiments which can also result in a lower or zero open circuit potential. In contrast, impurities like oxide films or other particles would increase the overpotential due to the decrease of the surface area. A typical phenomenon observed during voltammetric cycles involving phase formation is the so-called “nucleation loop”. This loop appears in all voltammograms with freshly polished or blank electrodes, where nucleation is essential. The metal deposition on a foreign substrate requires an overpotential necessary for nucleation, leading to a trace crossing in the reverse sweep, where the overpotential is no longer necessary due to the already formed new phase.[59]

The nucleation loop is visible in Fig. 18 c) and d). To ensure a clean surface without metal deposited during the previous scan, the OCP must be checked after each measurement. If there is a change in OCP, it can be helpful to polish the surface of the WE after each measurement to ensure a clean surface and the same reaction conditions for every measurement. In case of the Pt WE in Uralumina 150 the OCP is at 0.8 V vs. Al/Al^{3+}. Is the OCP at 0 V there probably are Al particles on the surface, no further nucleation is necessary in the CV and therefore, no nucleation loop can be seen like in Fig. 18 a) and b).[60]

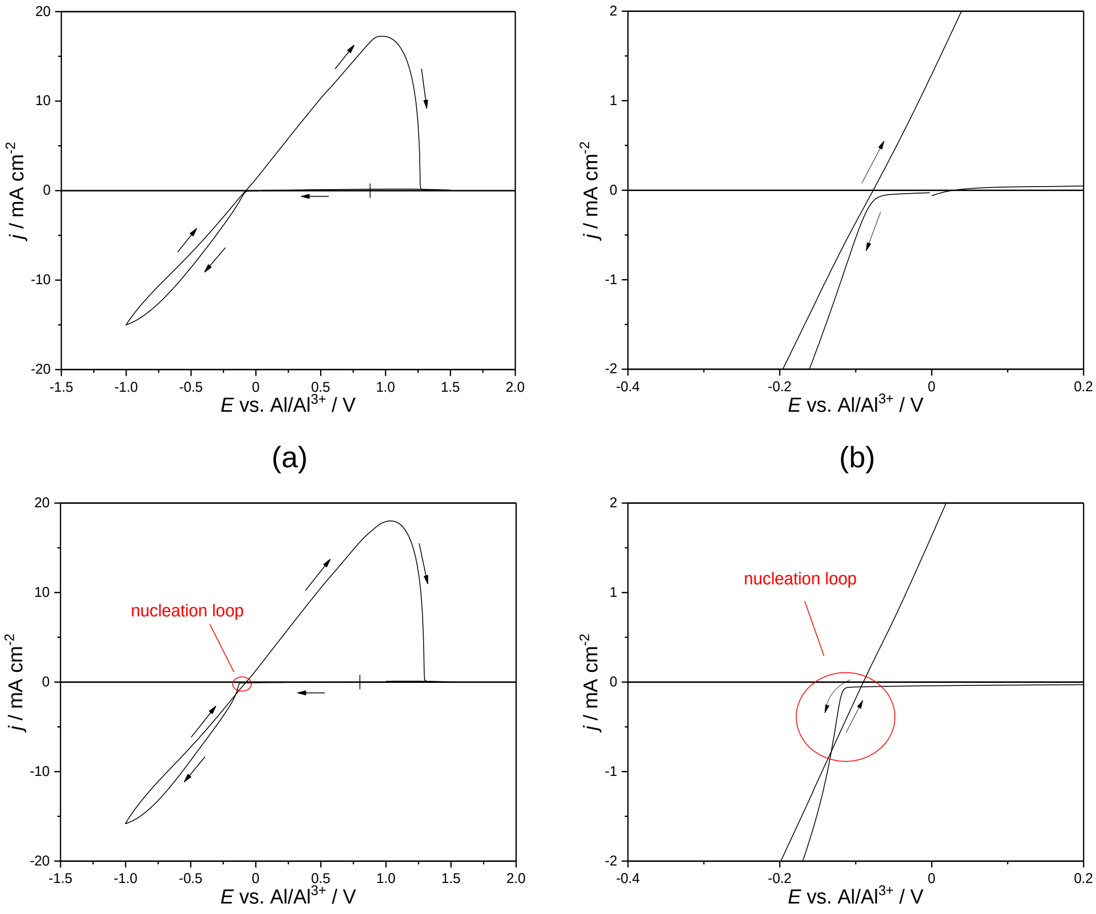

(a) (b)

(c) (d)

Fig. 18: The influence of a clean electrode surface on the nucleation overpotential and the form of the CV. In diagram a) and b) there is no nucleation overpotential visible (unpolished electrode surface). In diagram c) and d) there is a nucleation overpotential visible as well as the nucleation loop (electrode polished before measurement). All measurements were performed with a Pt working electrode. The scan rate was 10 mV/s.

iv) *Variation of scan rates*

The CV in *Fig. 19* shows a typical cycle of the deposition and dissolution of aluminium on a copper working electrode between −1.0 V and 0.5 V vs Al/Al^{3+}. The scan started at the OCP of 0.4 V vs. Al/Al^{3+} in cathodic direction. The reduction of the complex aluminium ion $[Al_2Cl_7]^-$ starts at −0.1 V vs Al/Al^{3+} and the aluminium dissolution starts at 0.1 V vs. Al/Al^{3+} in the anodic return sweep. In *Fig. 19* a) the cyclic voltammetry is performed without *iR* drop correction and in b) the *iR* drop was compensated during the measurement. In diagram b) the deposition of Al is characterised by a broad cathodic peak with a maximum at around −1.0 V vs Al/Al^{3+}. The scan rate was varied between 1 mV/s to 1000 mV/s at a temperature of 21 °C. It is observed, that the current density at around −1.0 V vs Al/Al^{3+}, where the aluminium deposition occurs, increased with increasing scan rate (*Table 2A*).

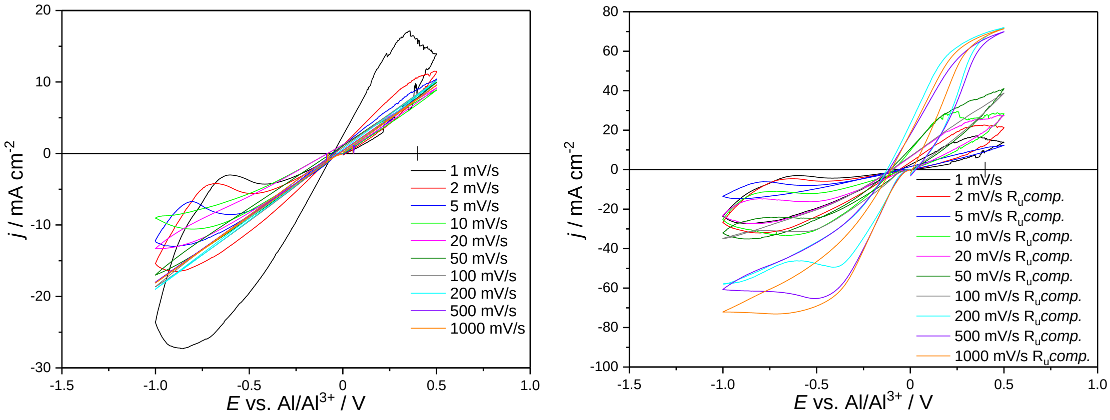

(a) (b)

Fig. 19: Cyclic voltammograms on Cu working electrode at different scan rates between -1 and 0.5 V vs. Al/Al^{3+}. The potential values in a) are uncompensated and in diagram b) the iR drop at the working electrode is compensated during the measurement.

The cathodic peak current density was plotted against the square root of the scan rate to see if there is a linear relationship between these two quantities according to the Randles-Sevcik equation [eq. (15)]. The correlation coefficient of the linear regression is only −0.982. Additionally, the plot does not pass through the origin. The plot can be seen in *Fig. 20*.

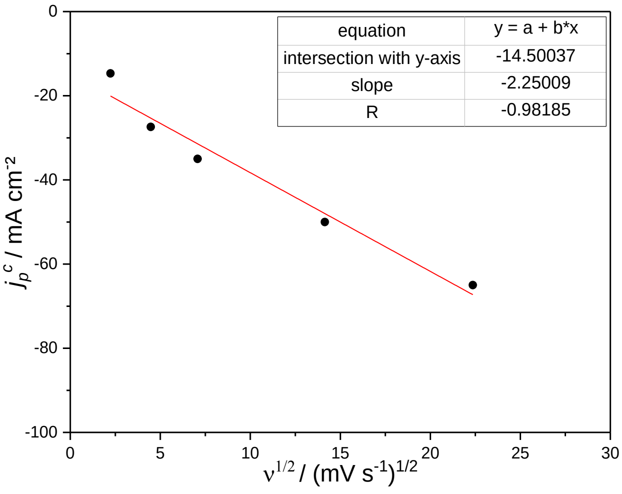

Fig. 20: Cathodic peak current densities at −0.8 V vs Al/Al^{3+} as a function of the square root of scan rate.

If the peak current increases linearly with the square root of the scan rate and passes through the origin, this would indicate that the Al deposition reaction is limited by diffusion of $[Al_2Cl_7]^-$ anions. However, the data obtained from the deposition of aluminium in cyclic voltammetry does not follow the Randles-Sevcik equation. One reason can be the influence of the ohmic drop on the peak current. The influence of the *iR* drop was minimised throughout the complete electrochemical measurement by automatic *iR* drop compensation. Perhaps the extent of compensation was not large enough or inconsistent throughout the different scan rates. Another important point might be that the reaction is not diffusion controlled but another step is controlling the reaction rate. The active species $[Al_2Cl_7]^-$ reacts according to equation (3). The equilibrium of the anions in the diffusion layer can be expressed in the reaction in equation (21) according to Schaltin et. al. [61]:

$$[Al_2Cl_7]^- + Cl^- \rightleftharpoons 2\ [AlCl_4]^- \qquad (21)$$

In the paper from Schaltin et al. it is reported for the $AlCl_3$:[EMIm]Cl IL with an equilibrium constant K_{eq} to be $10^{17.1}$. It is presumed that this equilibrium between the electroactive $[Al_2Cl_7]^-$ and the inactive $[AlCl_4]^-$ is also valid for the DES $AlCl_3$:urea.
If $[Al_2Cl_7]^-$ reacts in the diffusion layer to $[AlCl_4]^-$, this decreases the electrodeposition rate of Al and accordingly the current density in the electrodeposition process from Uralumina 150. The reduction of $[Al_2Cl_7]^-$ to Al is the net reduction of eq. (22) & (23):

$$[Al_2Cl_7]^- + 3\ e^- \rightleftharpoons Al + [AlCl_4]^- + 3\ Cl^- \qquad (22)$$

$$3\ Cl^- + 3\ [Al_2Cl_7]^- \rightleftharpoons 6\ [AlCl_4]^- \qquad (23)$$

These equations explain the presence of free Cl^- ions ion the electrolyte, which is a missing information according to equation (3) where $[Al_2Cl_7]^-$ is reduced to Al and $[AlCl_4]^-$.
Because of the current data obtained from the deposition and dissolution of aluminium in cyclic voltammetry does not follow the Randles-Sevcik equation, it is understood that the reaction mechanism in the cyclic voltammograms is not controlled by diffusion. Therefore, the diffusion coefficient could not be extracted from this data. In the next step RDE voltammetry was performed to find out, whether steady-state current data could be obtained.

3.1.2 **RDE voltammetry**

i) Influence of the iR drop on Al deposition in Uralumina 150

The RDE studies are performed in Uralumina 150 with a Pt disk working electrode at 21 °C in order to determine the diffusion coefficient of the species $[Al_2Cl_7]^-$. The corresponding RDE voltammograms are presented in Fig. 21 and Fig. 22 for rotational rates ranging from 100 to 4900 rpm at scan rates of 10 mV/s and 50 mV/s. The scan started at the OCP (+0.8 V vs. Al/Al^{3+}) and the potential was swept in negative direction to a switching potential of –1.0 V and then reversed in positive direction to 1.5 V vs. Al/Al^{3+} and back to the OCP were the scan stopped. On the reverse scan, a current hysteresis related to the nucleation process is recorded followed by the complete anodic stripping of the Al deposited on the forward scan.

In Fig. 21 a) the cathodic current density at –1.0 V vs. Al/Al^{3+} is –20 mA/cm² and the anodic current density is 27 mA/cm² at 1.5 V vs. Al/Al^{3+}. There is no significant current density increase with increasing rotational rate and there is no typical plateau shape for a steady state current observed.

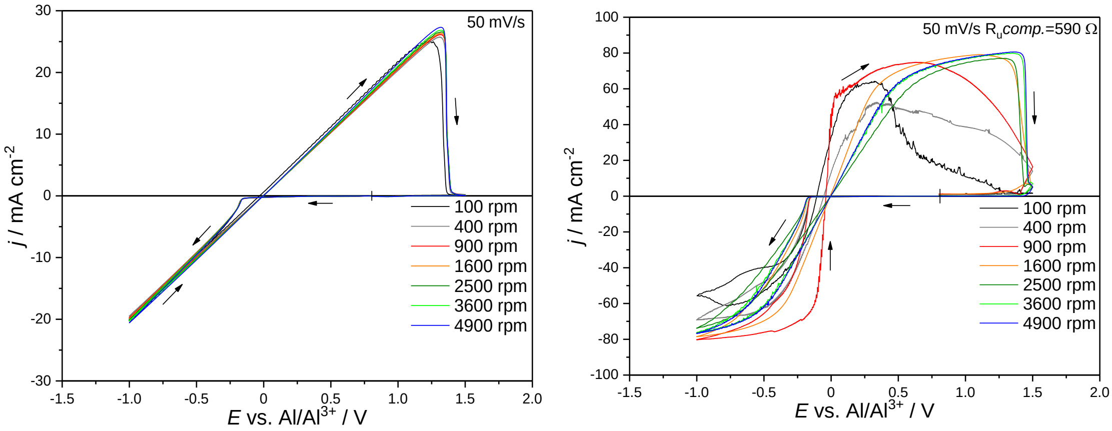

(a) (b)

Fig. 21: CV performed with a rotating Pt disk electrode at a scan rate of 50 mV/s in Uralumina 150 from -1.0 V to 1.5 V vs. Al/Al^{3+}. a) The iR drop is not compensated, whereas in b) the iR drop was compensated during the measurement. The working electrode was rotated with varying rotational rates between 100 to 4900 rpm.

The main mode of RDE operation is to determine the current as a function of potential under steady-state mass transfer. It is assumed that the electrolyte flow in a laminar regime to the surface of the working electrode. This organized flow without turbulences is only true below a critical rotation rate.[62] If the RDE technique is used in low conductivity electrolyte, one way to deal with the solution resistance is to perform compensation of the *iR* drop in real time.[63] This was carried out for the RDE voltammograms in Fig. 21 b). During the RDE voltammetry with varying rotational rates, the *iR* drop between the working electrode and the reference electrode was compensated with 590 ohms. This results in a RDE voltammogram with a cathodic current density plateau of –76.3 mA/cm² (4900 rpm) at –1.0 V vs. Al/Al^{3+} and an anodic current density plateau of 80 mA/cm² (4900 rpm) at 1.5 V vs. Al/Al^{3+}. The current density increased from Fig. 21 a) to Fig. 21 b) by the value of 58 mA/cm² for Al deposition (–1.0 V) and 53 mA/cm² in Al stripping (1.5 V) at 4900 rpm (*Table 5A*).

The graphs show that the measured currents increased with the increasing rotational rate of the working electrode.

The same behaviour of the RDE voltammograms is observed with a scan rate of 10 mV/s. In Fig. 22 a) the cathodic current density of –20 mA/cm² is measured at the cathodic switching potential of –1 V and the anodic peak current density is 28 mA/cm² for all scan rates above 900 rpm. If the ohmic drop is compensated (Fig. 22 b) the cathodic current density rises to –65 mA/cm² at –1 V and the anodic current to 65 mA/cm² at 1.4 V vs. Al/Al^{3+} (*Table 6A*). Also, the current density increases with rotational rate, except at 1600 rpm where the value is higher than the current density at 4900 rpm.

In Fig. 21 b) and Fig. 22 b) shape of the RDE voltammograms are well expressed compared to Fig. 21 a) and Fig. 22 a) where the shape of the voltammograms are influenced by the ohmic resistance.

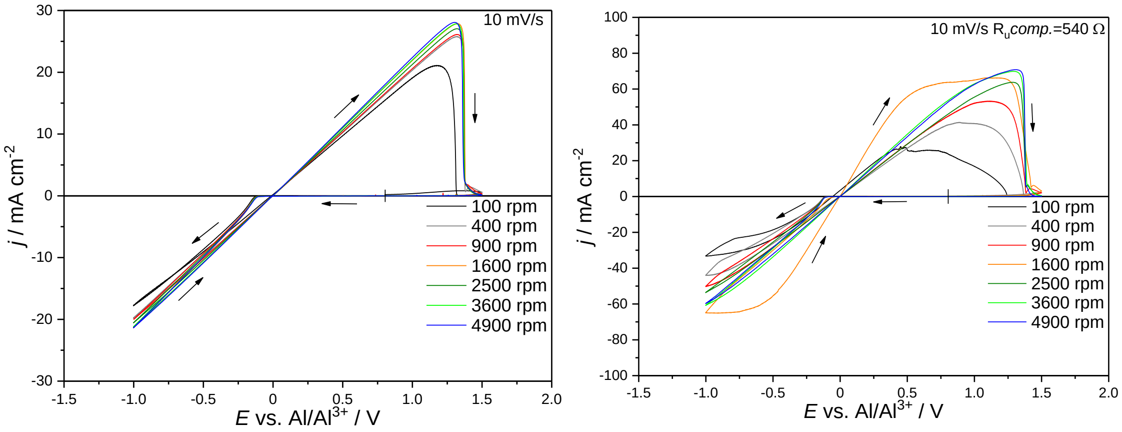

(a) (b)

Fig. 22: RDE voltammograms with Pt working electrode in a potential range between -1.0 V and 1.5 V vs. Al/Al^{3+} with a scan rate of 10 mV/s. The voltammograms in a) are uncompensated and in b) the iR drop was compensated during the measurement. The RDE voltammetry was performed in Uralumina 150 with a varying rotational rate of the working electrode between 100 rpm and 4900 rpm.

A common way of analysing the data of diffusion controlled systems is with Levich equation. The Levich equation [equation (12)], is a method to determine the diffusion coefficient as described in a previous section. In short, there was no linear correlation between the measured steady-state currents at a potential of −1 V vs. Al/Al^{3+} and the square root of the rotational rate of the working electrode (Fig. 23). Therefore, no diffusion limitation is given and the diffusion coefficient of the active species [Al$_2$Cl$_7$]$^-$ cannot be determined with the use of Levich equation.

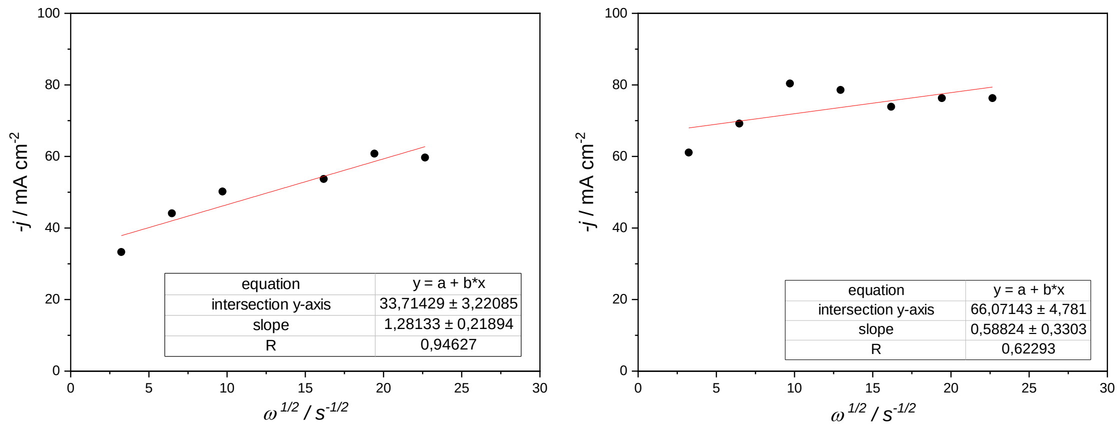

(a) (b)

Fig. 23: Plot of j vs $\omega^{1/2}$ measured at a scan rate of a) 10 mV/s and b) 50 mV/s in Uralumina 150 with Pt disk RDE and iR compensation. The red line is the linea regression of the measured data. The data point measured at 1600 rpm for 10 mV/s is not included in the regression (outlier).

Another method of analysing limiting currents in RDE voltammetry is to use the Koutecky–Levich equation (13) and plot i^{-1} (or j^{-1}) vs. $\omega^{-1/2}$, where i is the current and ω is the angular frequency of rotation (Fig. 24). In this plot the line intercepts the vertical axis above zero which indicates the reaction rate is rather limited by slow kinetics instead of mass transport.

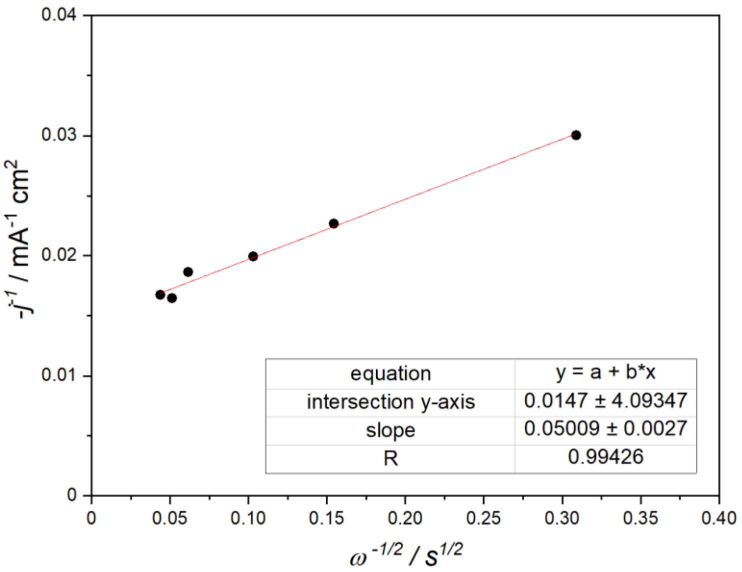

Fig. 24: Plot of j^{-1} vs. $\omega^{-1/2}$ measured at a scan rate of 10 mV/s in Uralumina 150 with Pt disk RDE. The line is the linear fit of the experimental data. The current densities are measured at −1 V vs. Al/Al^{3+}. The data point measured at 1600 rpm is not included in the regression (outlier)

For a kinetically controlled reaction, the plot should be linear and the intercept with the y-axis gives the kinetic current, i_k [eq (24)]:

$$\frac{1}{i_K} = \frac{1}{z \cdot F \cdot k_{red} \cdot c} \tag{24}$$

i_K .... *kinetic current [A]*
z .... *number of electrons transferred per ion*
F .... *Faraday constant, 96485 [C/mol]*
k_{red} .... *reduction rate constant [cm/s]*
c .... *concentration [mol/cm^3]*

From the intercept in Fig. 24 the reduction rate constant of the active species in the electrolyte can be determined following equation (24). The rate constant for the reduction reaction is of interest regarding reaction (21) where there is a chemical equilibrium between the electroactive dimer $[Al_2Cl_7]^-$ and the monomer $[AlCl_4]^-$ according to Schaltin et al [64] (equation 8). The kinetics of this equilibrium can thus limit the rate of the plating process of Al. The equilibrium between the metal-complexes in the electrolyte is not influenced by the applied potential. Hence, the reaction can be limited by the kinetics of this equilibrium instead of mass transport. The rate constant k_{red} is calculated to be $9.08 \cdot 10^{-7}$ m/s.

The diffusion coefficient was calculated based on the slope of the linear fit through the experimental data points determined on the steady-state current analysis. The used formula (25) is:

$$slope = \frac{-j^{-1}}{\omega^{-1/2}} = \frac{1}{0.62 \cdot F \cdot z \cdot D^{2/3} \cdot \upsilon^{-(1/6)} \cdot c} \tag{25}$$

j .... current density [A]
F .... Faraday constant, 96485 [C/mol]
z.............. number of electrons transferred per molecule or ion
D .... diffusion coefficient [cm²/s]
υ.............. kinematic viscosity [cm²/s]
c.............. bulk concentration of analyte [mol/cm³]

The diffusion coefficient $D_{[Al2Cl7]-}$ of the active species $[Al_2Cl_7]^-$ is calculated to be $2.39 \cdot 10^{-7}$ cm²/s.

Because a steady-state is more likely achieved with lower scan rates, the diffusion coefficient was calculated for RDE voltammetry measurement at 10 mV/s. The plot of j^{-1} vs. $\omega^{-1/2}$ measured at a scan rate of 50 mV/s is listed in the appendix (*Fig. 11A*).

The diffusion coefficient was calculated based on the assumption that 30 % of the $AlCl_3$ in the electrolyte reacts to $[Al_2Cl_7]^-$ as active species. Earlier in this work, the reaction mechanism of $[Al_2Cl_7]^-$ formation is described by reaction (4) and (2). Besides heptachlorodialuminate, there is also $[AlCl_4]^-$ as main species [equation (21)], as well as $[AlCl_2(urea)_2]^+$ and $[AlCl_2(urea)]^+$ as cations. The characterization of the DES $AlCl_3$:urea regarding the concentration and the structure of the formed species is already done by Raman spectroscopy from different authors.[65][66]

The kinematic viscosity is $52 \cdot 10^{-6}$ m²/s determined by the viscosity measurements in our lab[1] (with Mikro-Ubbelohde-Viscometer Typ 536 23 & 536 30 from SI Analytics via test standard DIN 51 562 part 2) and the concentration is calculated to be 2.59 mol/l. In literature there are different values reported for $D_{[Al2Cl7]-}$ in DESs and ILs depending on the concentration of the active species, the kinematic viscosity and the temperature. With regard to the diffusion coefficients in *Table 3* (10^{-7} cm²/s), the calculated diffusion coefficient (10^{-7} cm²/s) is in the same order of magnitude as the diffusion coefficient in

---

[1] Many thanks to Philipp Materna for doing the viscosity measurement for us.

$AlCl_3$:[EMIm]Cl.

Table 3: Diffusion coefficient in different media

electrolyte	molar ratio	ν [m²/s]	$D_{[Al2Cl7]-}$ [cm²/s]	c [mol/l]	T [°C]	reference
$AlCl_3$:[EMIm]Cl	1.5:1	$8.34 \cdot 10^{-6}$	$1.17 \cdot 10^{-7}$	1.981	40	Schaltin et al 2011 [64]
$AlCl_3$:[EMIm]Cl	1.1:1	-·*	$9.2 \cdot 10^{-7}$	0.455	25	Carlin et al 1992 [67]
$AlCl_3$:[EMIm]Cl	1.65:1	-·	$6.89 \cdot 10^{-7}$	1.8185	90	Pradhan et al 2009 [68]
NaCl:KCl:$AlCl_3$	66:20:14	-	$5.7 \cdot 10^{-6}$	0.085	140	Jafarian et al 2006 [60]
$AlCl_3$:[EMIm]Cl	2:1	-·	$7.11 \cdot 10^{-7}$	3.41	RT	Böttcher et al 2020 [16]

* *the kinematic viscosity for $AlCl_3$:[EMIm]Cl with mole fractions of $AlCl_3$ from 0.5 to 0.67 decreases from $11.3 \cdot 10^{-6}$ to $8.9 \cdot 10^{-6}$ m²/s at 30 °C, respectively.* [69]

Schaltin et al [64] calculated a diffusion coefficient of $1.17 \cdot 10^{-7}$ cm²/s and a rate constant k_{red} of $1.89 \cdot 10^{-5}$ m/s. For the electrolyte Uralumina 150 the rate constant k_{red} is $9.08 \cdot 10^{-7}$ m/s and the diffusion coefficient is $2.39 \cdot 10^{-7}$ cm²/s. The rate constant in Uralumina 150 is around one order of magnitude lower than the rate constant in $AlCl_3$:[EMIm]Cl. The $D_{[Al2Cl7]-}$ of Uralumina 150 is in the same range as $D_{[Al2Cl7]-}$ values listed in Table 3. When compared $D_{[Al2Cl7]-}$ of Uralumina 150 with $D_{[Al2Cl7]-}$ calculated by Schaltin et al., the diffusion of the active species in Uralumina 150 is slightly faster than in $AlCl_3$:[EMIm]Cl, while the rate constant is lower. There is a difference in the composition of the electrolytes and therefore, different properties are expected. The experiment with Uralumina 150 was performed at RT, whereas Schaltin et al. performed the experiment at 40 °C. A higher temperature decreases the viscosity of the electrolyte and should result in a higher diffusion coefficient, but the concentration of the active species is much higher in Uralumina 150 compared to the concentration in $AlCl_3$:[EMIm]Cl used in the paper of Schaltin et al. (2.59 mol/L vs. 1.981 mol/L).

The limiting current densities determined experimentally in the RDE voltammetry at 10 mV/s are in the same range as the limiting current densities experimentally determined by Schaltin et al. For example at 100 rpm the limiting current densities are −33.3 mA/cm² (Uralumina 150) and −40.3 mA/cm² ($AlCl_3$:[EMIm]Cl). At 1600 rpm and 10 mV/s a current density is measured of –65.1 mA/cm² which is not in line with the current densities at the other rotational rates, so this value is not used for the regression in the Levich and Koutecky-Levich plots. The kinetically limited current density is determined from the intersection with the y-axis in the Koutecky-Levich plot and is estimated to be –68.03 mA/cm². Applying higher current densities at DC or pulsed current aluminum electrodeposition does not lead to a faster Al deposition. This must be kept in mind, while thinking about the used parameters in electrochemical Al deposition. According to Winand et al. [37] the ratio of the applied plating current density to the limiting current density influences the obtained morphology of the plated Al, as well as the inhibition intensity.

3.2 Direct current aluminum deposition

Electrodeposition of aluminum was conducted on a copper working electrode from 1.5:1 molar ratio $AlCl_3$:urea deep eutectic solvent (Uralumina 150) by direct current plating. The kinetically limited current density (–68.03 mA/cm²) is used to determine the range of the current densities tested for direct current deposition. Five different current densities were tested: –10 mA/cm², –1 mA/cm², –0.220 mA/cm², –0.067 mA/cm² and –0.027 mA/cm². It has to be pointed out, that tests with 10 mA/cm² and 1 mA/cm² failed after a view seconds of measurement, due to too high cell voltages. The other three of them showed promising results and are discussed in the following chapter. The rest of the deposition parameters are summed up in *Table 4*.

Table 4: Direct current deposition parameters

Cell #	DC 1	DC 2	DC 3
WE material	Cu		
CE material	Al		
RE material	Al		
Nominal Al layer thickness [µm]	3.7		
current density [mA/cm²]	0.220	0.067	0.027
current [mA]	0.0622	0.0189	0.0076
duration [h]	13.45	44.18	109.6

Fig. 25 shows the SEM images of aluminum deposited on Cu from Uralumina 150 at different current densities a) –0.220 mA/cm² b) –0.067 mA/cm² and c) –0.027 mA/cm² for 13.45 h, 44.18 h and 109.6 h at RT. The SEM images show the homogeneous coverage of the Cu WE surface with plated aluminum. The morphology of the deposit is flaky formed on top of the metal layer. Underneath, the metal layer seems to be compact but without a cross-section analysis this is uncertain. For the EDS analysis a certain area is scanned (Fig. 25 d) and the data of the scan are summed up over the whole area. In the EDS spectra of the marked area on the plated aluminum 0.4 at% copper is detected together with 88.5 at% Al (Fig. 25 e). The naked Cu substrate area of the electrode consists of 66.2 at% Cu content together with 12.1 at% oxygen.

The morphology in image a) is more compact than in image c), where very fine but high flake-like deposits can be seen. In image b) the morphology is flaky similar to a), but the flakes are larger. The morphology of the Al deposited with a current density of 0.027 mA/cm² shows flakes that are very thin but large. By comparing the three current densities based of the morphology visualized in Fig. 25, it can be said that lower current densities lead to larger flake-like grains and the morphology in general is more inhomogeneous and rough.

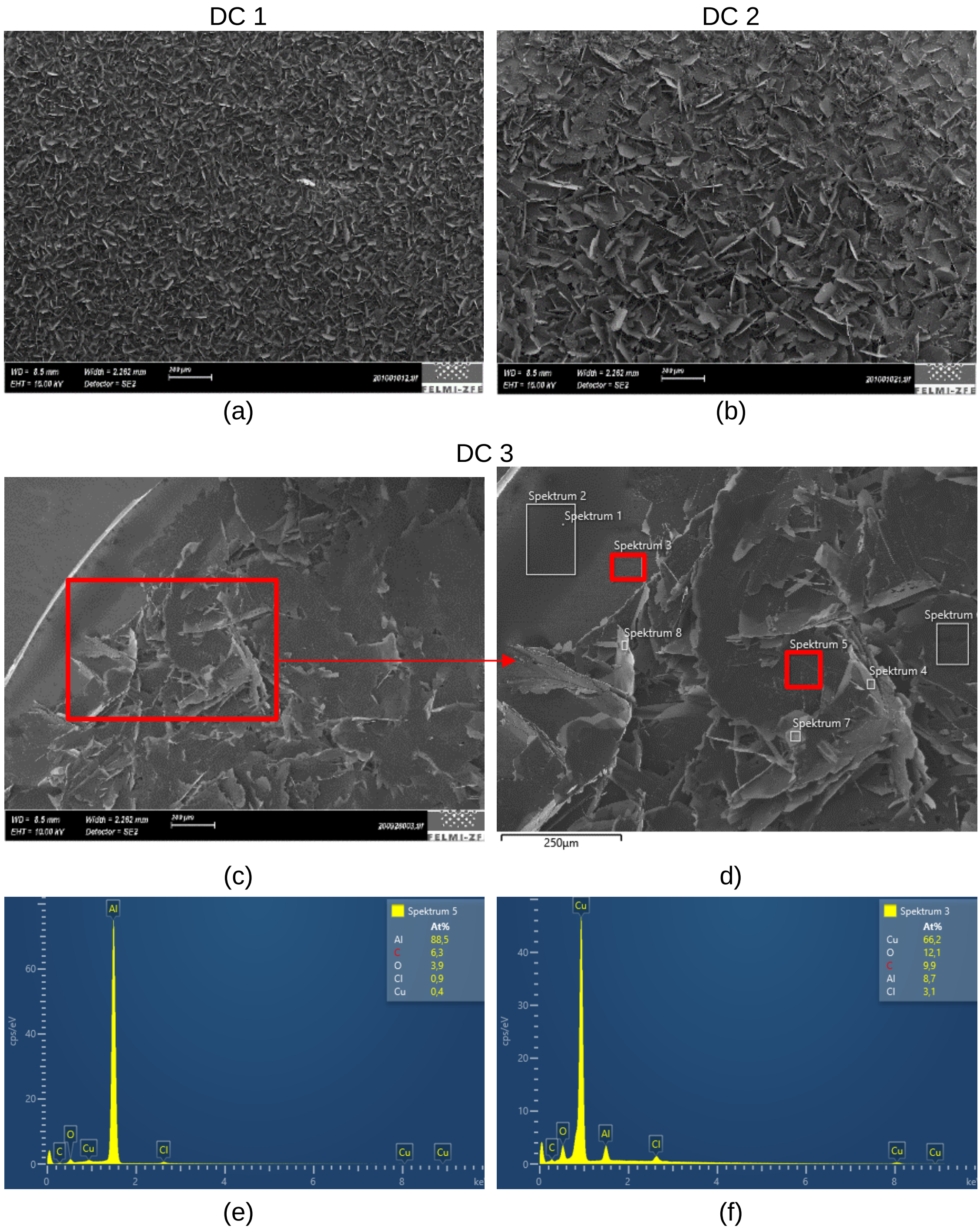

Fig. 25: Lower magnification SEM images of metal layer electrochemically deposited via direct current deposition of aluminum an Cu as WE. Three different current densities were tested, a) 0.220 mA/cm² b) 0.067 mA/cm² c) 0.027 mA/cm² and d) the different EDX spectrums of the surface metal layer in DC 3 is shown. In e) the spectra of area 5 and in f) the spectra of area 3 can be seen.

In Fig. 26 SEM images of the deposited Al layers are shown with higher magnification for determining the specific morphology of each deposit. It is clearly visible that flakes have formed during the deposition. If there is a compact Al layer underneath still cannot be said. The flake-like crystallites are getting thinner and larger by lowering the current densities. In b) there are grain like deposits on the flakes. The EDS analysis of DC 2 in

Fig. 26 d) revealed that the deposit in this area is composed of metallic aluminum (90.1 at%), followed by carbon (8.9 at%) and oxygen (0.8 at%).

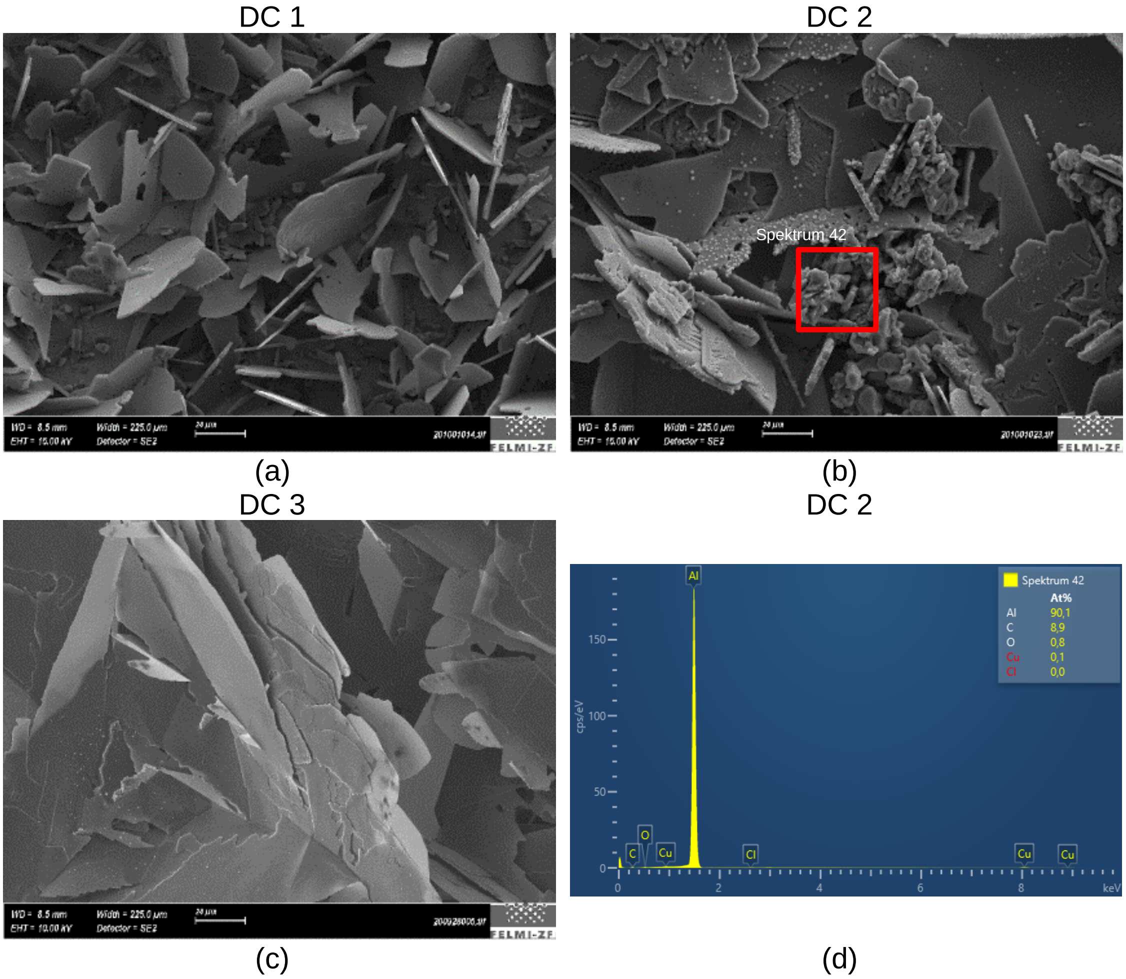

(a) (b)

(c) (d)

Fig. 26: Higher magnification SEM images of the morphology of aluminum deposits on Cu substrate via direct current deposition. Current densities were a) 0.220 mA/cm² b) 0.067 mA/cm² and c) 0.027 mA/cm². In d) is the EDX spectra of area 42 in DC 2 listed.

In direct current aluminum deposition, the aluminum metal layer is very rough with the formation of flake-like grains. The higher the current density the more homogeneous is the aluminum layer with smaller flaky grains, even though it is still very disperse. If the current density is higher, it results in a higher nucleation overpotential at the beginning of the deposition. The higher the overpotential the more nuclei can form initially and grow. The nuclei formed on the surface are more homogeneously spread in Fig. 25 a) compared to Fig. 25 c, which results in a more dense metal layer. As the metal layer continues to grow, it seems as Al grows in direction of the electric field, and therefore, flake-like grains are formed. The electric field distribution is inhomogeneous at rough surfaces, leading to higher current densities at peaks and lower current densities in valleys.[40] This can be an explanation for ongoing FI-type growth after the first flakes have formed.

The flakes are more dense and thicker for higher current densities and thinner for lower current densities. The lower current density results in a lower overpotential, lower number of growth sites and therefore, a less dense metal layer with fewer and larger individual flakes. With a current density of –0.067 mA/cm² the growth of the nuclei seems to be progressive due to the small grains visible in the SEM image. According to Winand et al. [37] the obtained morphology is called basis reproduction with FI dendrites or flakes obtained from low inhibition. By changing the DC deposition method to pulsed-current deposition method, the morphology was expected to become more compact, because of the increase of the pulse current density due to smaller duty cycle and published data on the beneficial use of pulse plating (sections 1.3 & 1.4).[43][46]

3.3 Pulsed current aluminum deposition

Electrodeposition of aluminum was conducted on copper working electrodes from 1.5:1 molar ratio $AlCl_3$:urea mixtures by pulse-interrupt current (PIC) plating. The morphologies of the deposits were characterized with SEM and EDS analysis showed that the deposits were composed of Al (> 80 at%), next to O, C and Cl. *Table 5* summarizes the parameters used for the pulsed current deposition experiments.

Table 5: Pulse-interrupt current plating parameters of aluminum on Cu substrate.

cell #	PIC 1	PIC 2	PIC 3	PIC 4	PIC 5
WE material	Cu				
CE material	Al				
RE material	Al				
nominal Al layer thickness [µm]	3.7				
mean current density [mA/cm²]	0.067				
duration [h]	44.18				
duty cycle	0.5	0.1	0.5	0.1	0.01
frequency [Hz]	2	2	0.5	0.5	0.5
on-time	250 ms	50 ms	1 s	200 ms	20 ms
off-time	250 ms	450 ms	1 s	1800 ms	1980 ms
pulse current density [mA/cm²]	0.134	0.671	0.134	0.671	6.71
pulse current [mA]	0.0379	0.190	0.0379	0.190	1.90

Pulse-interrupt current was applied to electrodeposit aluminum under different conditions but without varying the mean current density of –0.067 mA/cm². After the direct current deposition experiments, this current density showed a promising deposited metal layer. Specifically, it is also used in the cathodic half-cell reaction for Al-S batteries. In the first two experiments PIC 1 and PIC 2, the duty cycle was 0.5 and 0.1, respectively. In order to determine the effect of the duty cycle, the pulse frequency was fixed at 2 Hz. The pulse current in PIC 1 was −0.0379 mA (0.134 mA/cm²) while that in PIC 2 was −0.190 mA (−0.671 mA/cm²). The ratio of the pulse current density to the kinetically limiting current density for PIC 1 and PIC 2 varied according to the x-axis in Fig. 1.

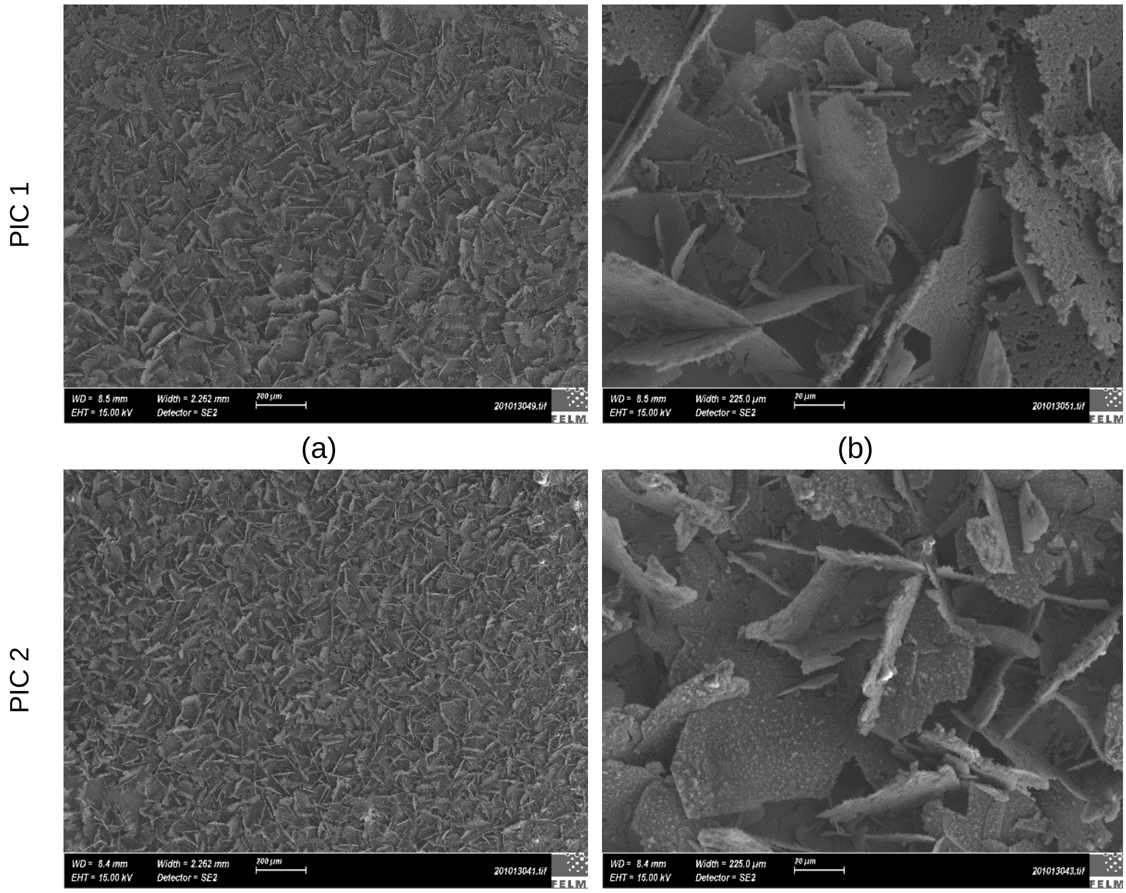

(a) (b)

(c) (d)

Fig. 27: SEM images of the morphology of Al deposited on Cu substrate for 44.18 h at a mean current density of 0.067 mA/cm² with different magnifications. In a) morphology of PIC 1 (200 µm scale bar) and b) morphology of PIC 1 at higher magnification (scale bar 20 µm). In c) morphology of PIC 2 (200 µm) and d) morphology of PIC 2 at higher magnification (scale bar 20 µm). The pulsed deposition parameter for PIC 1 and PIC 2 differ in case of the duty cycle (0.5 or 0.1) and the frequency was kept constant at 2 Hz.

In *Fig. 27* the morphology of the deposits is visualised by SEM images. The electrode surface is uniformly covered with an Al layer. The obtained morphologies are still rough like in DC plating with formation of flakes. By comparing the deposits in *Fig. 27* a) and c), the metal layer prepared with a duty cycle of 0.1 in c) is slightly less coarse and the flakes are somewhat smaller.

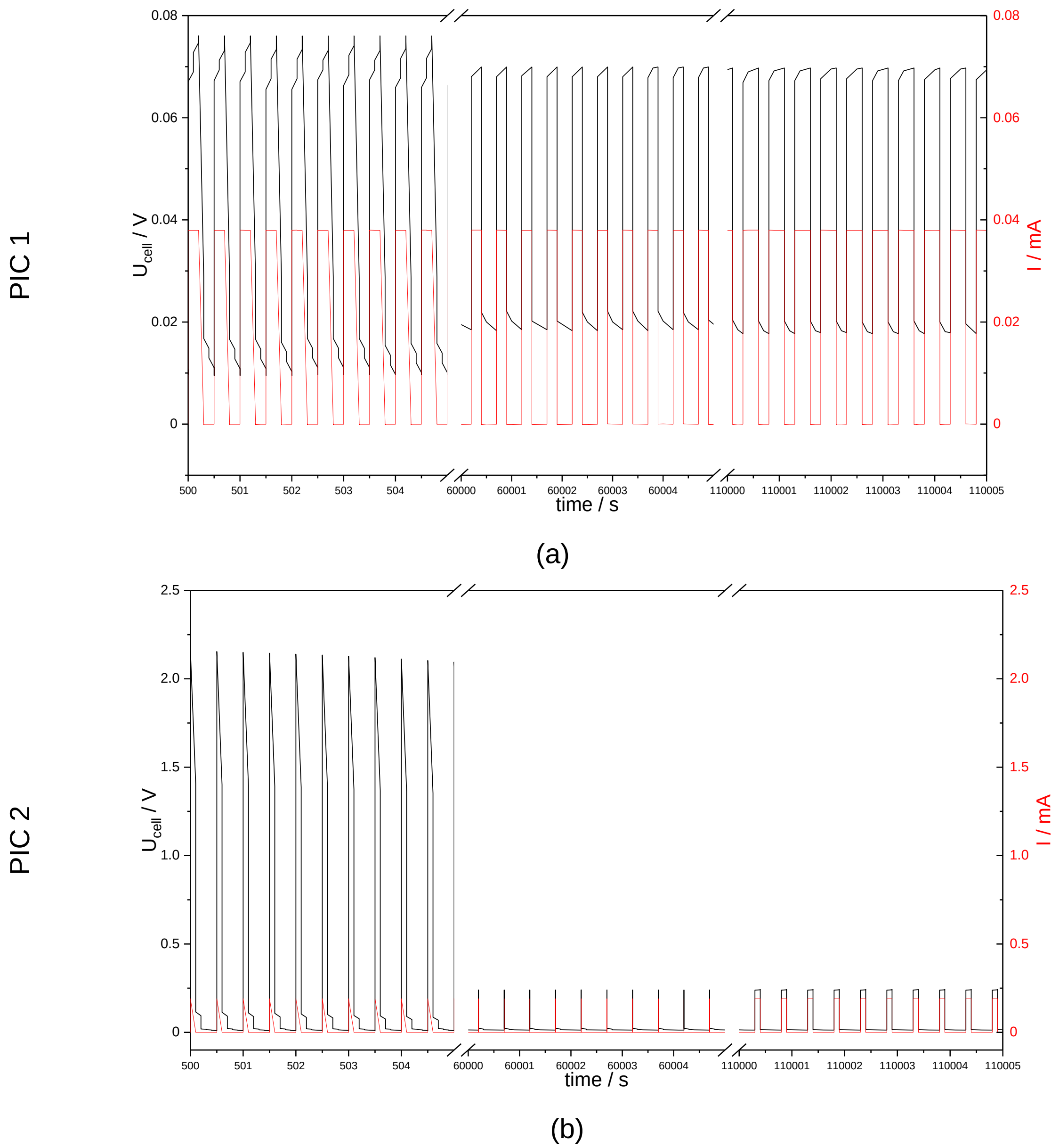

Fig. 28: Cell voltage on the left y-axis and current on the right y-axis of a) PIC 1 and b) PIC 2 over time. The cell voltage in three different time periods of the deposition process is shown.

In Fig. 28 the cell voltages of a) PIC 1 and b) PIC 2 are shown. In the appendix the cell voltage and the measured current for each cell is shown in an own diagram *(Fig. 12A* & *13A* for PIC 1 and *16A* & *17A* for PIC 2). At the beginning of the measurement, the cell voltage for PIC 2 is much higher compared to the cell voltage of PIC 1. By contrast, in a) the cell voltage is very constant during the whole measurement. There is no change in cell voltage visible compared to PIC 2, where the cell voltage at the beginning is much higher compared to the cell voltage after 60000 seconds. The reason for the higher cell voltage in PIC 2 can be an overvoltage on the counter electrode. Maybe there is an oxide layer or other inhibitors on the Al CE, which causes an overvoltage during Al dissolution. In Fig. 29 the potential of the working electrodes of a) PIC 1 and b) PIC 2 are plotted against time. In the appendix there is a detailed diagram for the working electrode PIC 1 (*Fig. 14A & 15A*) and PIC 2 (*Fig. 18A & 19A*). The potential of the working electrode starts at around 0.6 V vs. Al/Al^{3+}. The reason is the copper WE which has a more positive open circuit potential compared to the Al reference electrode. After a few seconds, when Al nuclei start to cover the surface of the Cu WE, the potential of the WE drops below 0 V. In Fig. 29 b) the overpotential of the working electrode during the pulse is 82 mV compared to the overpotential in Fig. 29 a) where the overpotential during the pulse is 25 mV vs. Al/Al^{3+}. This higher overpotential leads to a higher number of nuclei formed on the surface and results in a more compact metal deposit. To conclude, the duty cycle of 0.1 compared to 0.5 at a frequency of 2 Hz is more promising.

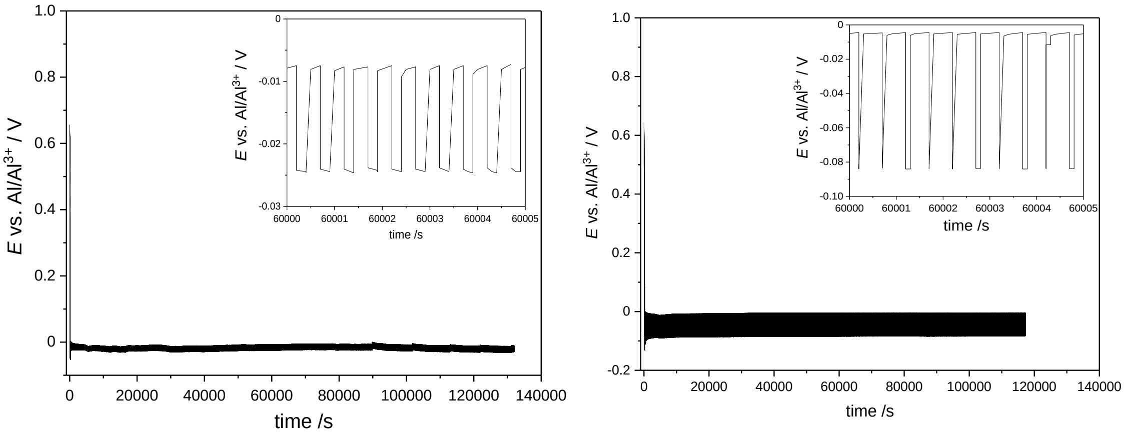

(a) (b)

Fig. 29: Working electrode potential of a) PIC 1 and b) PIC 2 over time. In the right corner of each diagram is a more detailed view on the wave form of the potential at 60000 seconds.

The next two measurements are PIC 3 and PIC 4, where the duty cycle was varied again between 0.5 and 0.1, while the frequency was fixed at 0.5 Hz. Lowering the frequency from 2 Hz to 0.5 Hz increased the off-time 4-fold from 250 ms to 1000 ms (duty cycle 0.5) and from 450 to 1800 ms (duty cycle 0.1). The mean current density and the pulse current density did not vary for the duty cycles 0.1 and 0.5. In *Fig. 30* the SEM images of the deposits from PIC 3 and PIC 4 are shown.

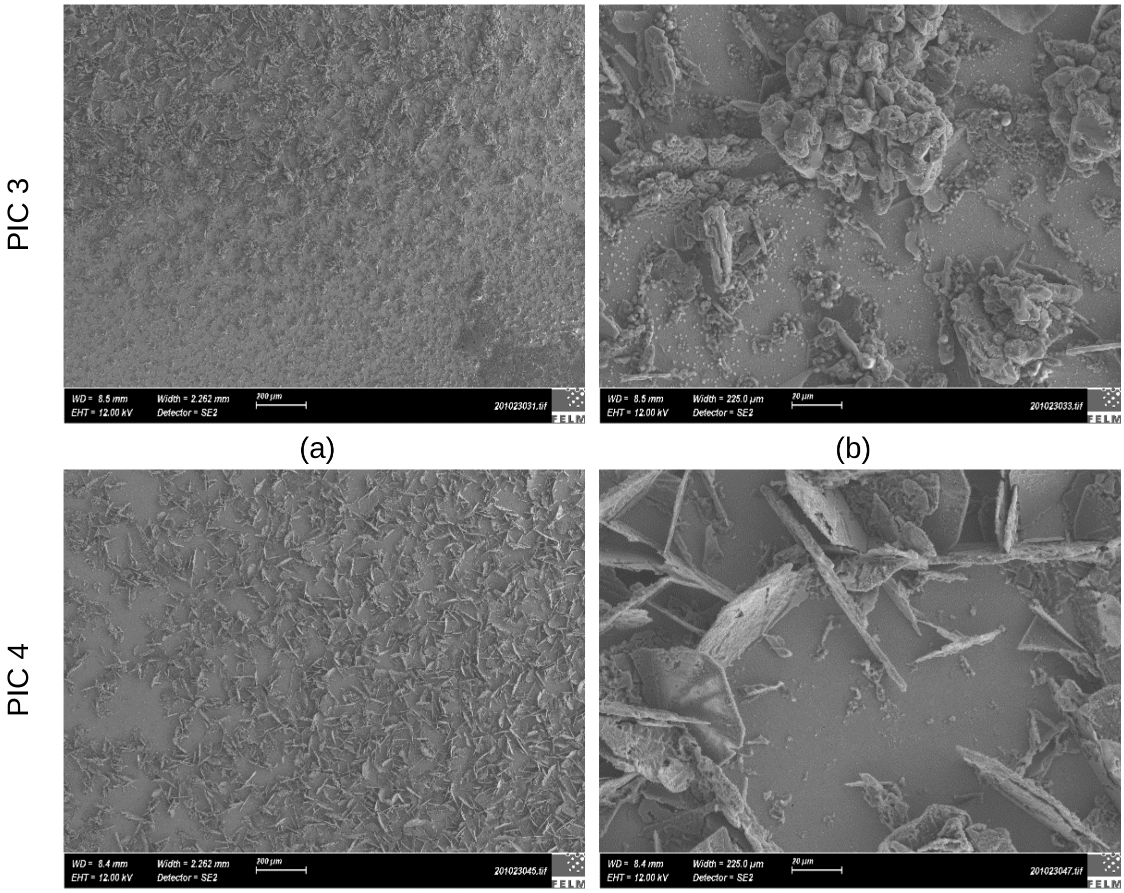

(a) (b)

(c) (d)

Fig. 30: Higher and lower magnification SEM images of the morphology of Al deposited on Cu substrate for 44.18 h at a mean current density of 0.067 mA/cm². In a) the morphology of PIC 3 (scale bar 200 µm) and b) morphology of PIC 3 with higher magnification (20 µm). In c) morphology of PIC 4 (with 200 µm) and d) morphology of PIC 4 with higher magnification (scale bar 20 µm). The pulse parameter for PIC 3 and PIC 4 varied in case of the duty cycle (0.5 vs. 0.1) and the frequency was kept constant at 0.5 Hz.

With an off-time of 1 s, the morphology appeared spongy with cauliflower like deposits. The surface is not covered completely, which can be seen in *Fig. 30* a) and b). In the appendix there is a detailed diagram for each cell regarding the cell voltage and the current for PIC 3 (*Fig. 20A*, *21A*) and PIC 4 (*Fig. 24A*, 25A). If compared to PIC 1, with the same duty cycle 0.5 but a frequency of 2 Hz instead of 0.5 Hz, the morphology changed from thin flakes to spongy cauliflower like deposits. One reason could be the coalescence of the grains during the longer off-time to from irregular and larger grains. Another reason could be progressive grain growth, which results in an inhomogeneous and coarse deposit morphology. The cell voltages in Fig. 31 for a) PIC 3 and b) PIC 4 are constant and did not vary much over time. During the first few minutes the cell voltages during the off-time varies compared to the rest of the deposition time, because the open circuit potential of bare Cu is significantly more positive than that of Al. The cell voltage for PIC 4 is constant after the initial phase. At the beginning the cell voltage is not following a strict square pulse form. The change in the pulse form roots in the higher overpotential needed at the blank Cu WE surface, to form thermodynamically stable nuclei, followed by the growth period. After the surface is covered with nuclei, the supplied energy results in grain growth. In Fig. 32 the potential of the working electrodes of a) PIC 3 and b) PIC 4 are plotted against time. In Fig. 32 b) the overpotential of the working electrode during the pulse is 100 mV compared to the overpotential in Fig. 32 a) which is 41 mV vs. Al/Al^{3+} during on-time. For a more detailed view on the data watch *Fig. 22A & 23A* for PIC 3 and *Fig. 26A & 27A* for PIC 4 in the appendix. This higher overpotential leads to a higher number of nuclei formed on the surface and should result in a more compact metal deposit. The grain shape of the deposit for PIC 4 differs from that of PIC 3. There are thin flakelike deposits, which grew in the direction of the electric field.

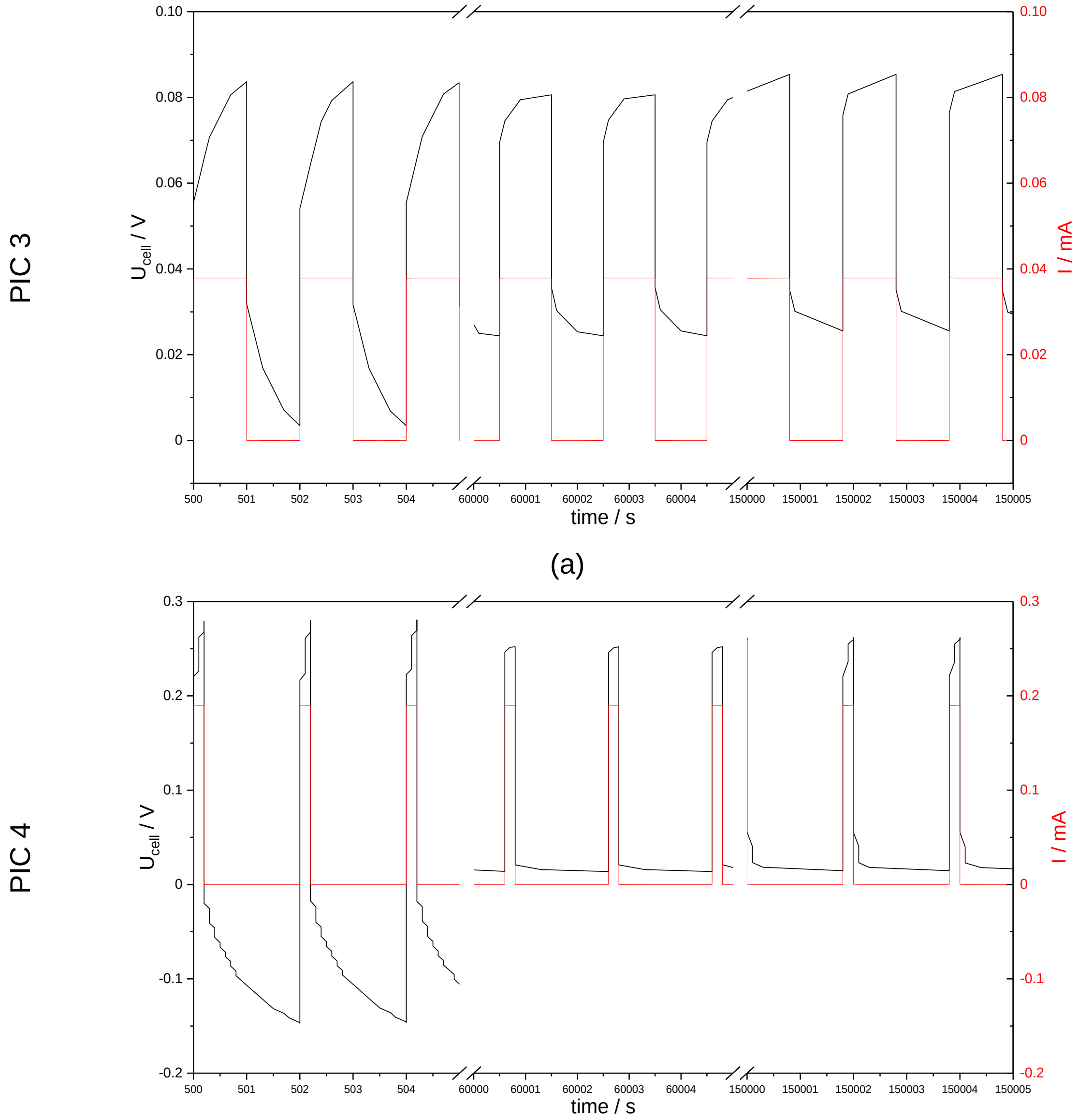

(a)

(b)

Fig. 31: Cell voltage an the left y-axis and current on the right y-axis of a) PIC 3 and b) PIC 4

during the deposition of Al on Cu substrate. Three different time periods are shown next to each other.

In addition, the surface is not homogeneously covered with Al. The formed grains did not coalesce during the off-time of 1800 ms. One reason can be instantaneous growth, which is more likely at higher pulse current. By comparing PIC 3 with PIC 4, the deposit Al particles are finer, thinner and more flake like in PIC 4. In PIC 3 the Al particles are more cauliflower like. The higher current densities in PIC 4 did not consequently lead to a more compact electrodeposit. The morphology in PIC 4 can be described as FI type as well as in PIC 3, but with a less dense electrodeposited Al layer (PIC 4).

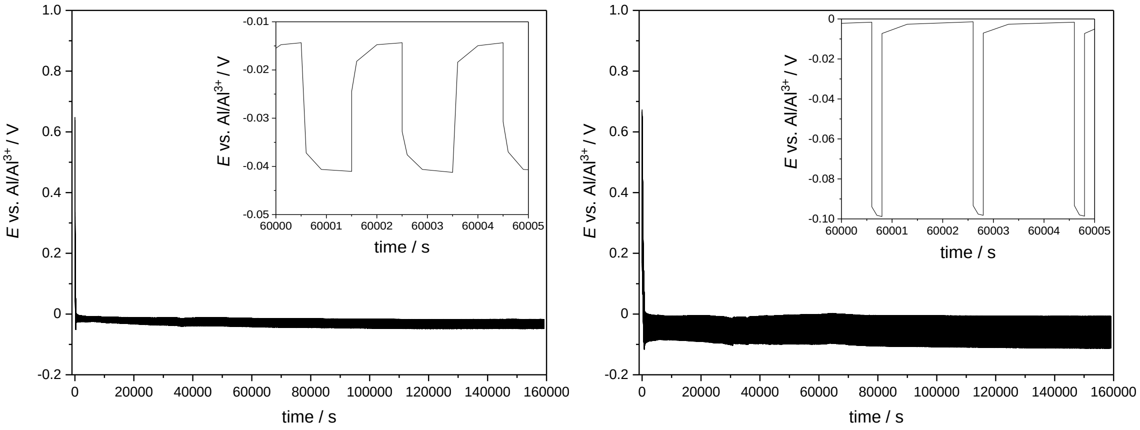

(a) (b)

Fig. 32: WE potential of a) PIC 3 and b) PIC 4 over the time of the deposition process. In the right corner of each diagram is a more detailed view on the wave form of the potential at 60000 seconds.

This leads to the last conducted measurement PIC 5. The frequency was kept constant at 0.5 Hz while the duty cycle was reduced to 0.01. This results in a pulse current of 1.9 mA (6.71 mA/cm²), which is 10 times higher than the pulse current in PIC 4. The SEM images in *Fig. 33* reveal a very fine and compact metal layer. The structure is less flaky and more compact with different growth sites on the surface and on the deposit. In *Fig. 33* a) the blank surface is the Cu WE, where the deposited metal was washed off during the removal of the electrolyte. As a negative aspect, the adhesion was very poor.

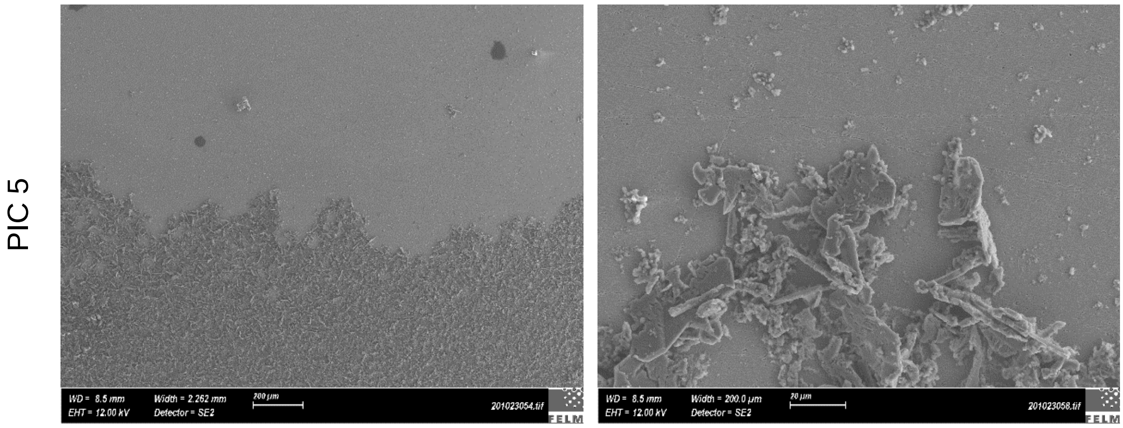

(a) (b)

Fig. 33: SEM images of the morphology of aluminum plated on Cu substrate for 44.18 h at a current density of 0.067 mA/cm² with a) lower magnification (200 µm) and b) higher magnification (20 µm). Pulse parameter for PIC 5 are a duty cycle of 0.01 and a frequency of 0.5 Hz.

The cell voltage during the cathodic pulses was quite stable over the whole deposition time. Only at the beginning the cell voltage during off-times varied compared to the cell voltage after 60000 seconds. The reason is the open circuit potential of the Cu WE, which is more positive compared to the OCP of Al. After the Cu WE surface was completely covered with Al, the cell voltage stabilized at 0 V vs. Al/Al^{3+} during off-time. (Fig. 34 a). The value of the cell voltage during on-time is around 1.8 V (Fig. 34 a). By comparing the potential of the working electrode to the cell voltage during on-time, there is a difference of around 1 V. This difference corresponds to the overpotential to dissolve aluminum from the counter electrode during the current pulse. In the appendix *Fig. 28A & 29A* covers the cell voltage and the measured current. In *Fig. 30A & 31A* the working electrode potential and the working electrode potential compared to the current over time is shown.

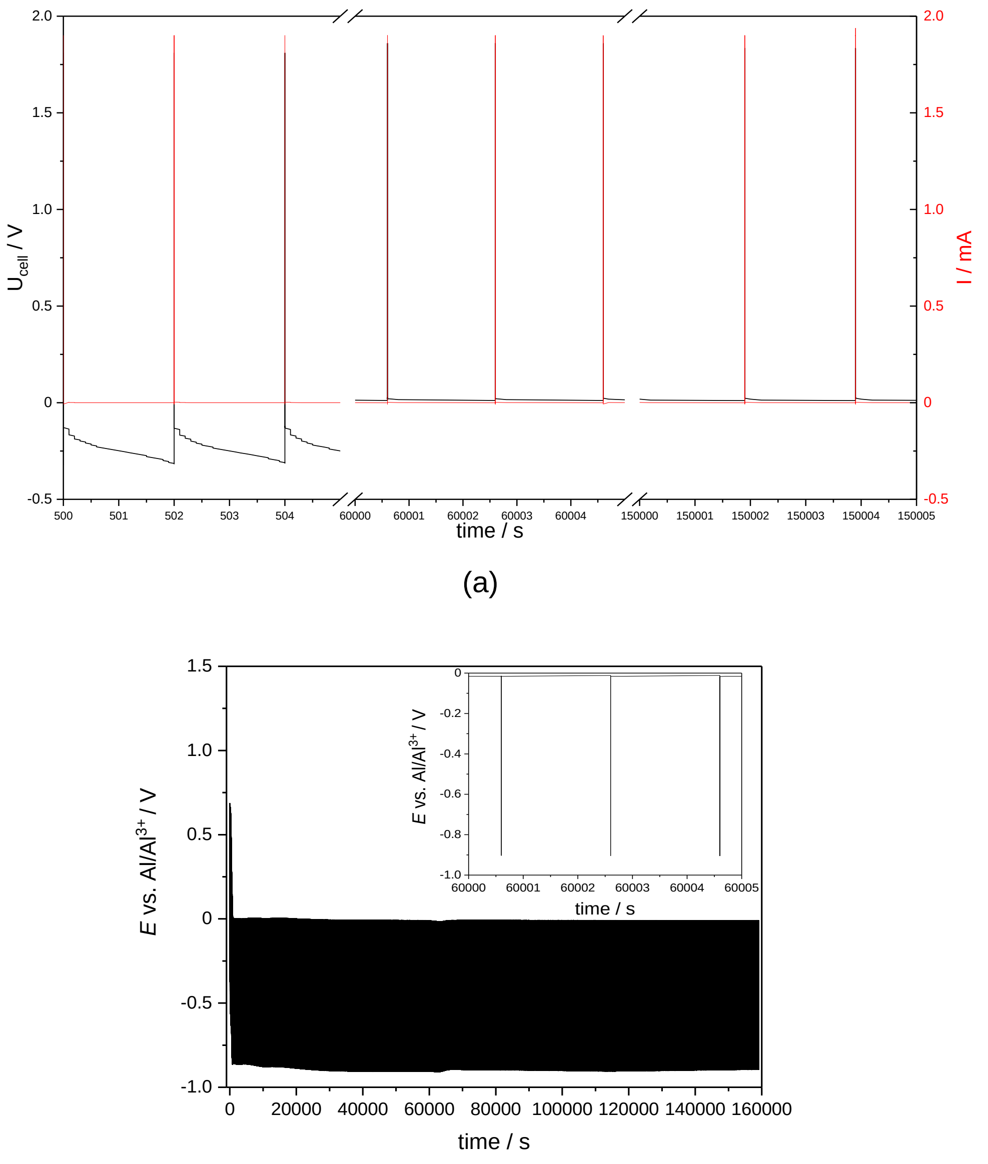

(a)

(b)

Fig. 34: a) Cell voltage on left y-axis and current on the right y-axis of the cell PIC 5 over three different periods. In b) the potential of the working electrode vs. Al/Al^{3+} is given over time. A better overview is given in the diagrams in the appendix.

To sum up the pulse deposition of Al on Cu substrate, it can be said, that in general the morphology is flaky and not compact. By varying the pulse parameters in a way that the pulse current is very high with a small duty cycle, the morphology can be influenced to a less flaky and more compact morphology. On the horizontal axis of Fig. 1 the used ratios of deposition current to limiting current varied from low to high. The morphology changed from BR with field-oriented isolated texture to the more unoriented dispersion type by increasing the pulse current to –1.90 mA (–6.71 mA/cm^2). The adhesion of the deposited Al on the Cu substrate was very poor. Generally, the adhesion was weaker with higher pulse current and longer off-times. If there was no metal deposited on the substrate, or the deposited metal layer was washed off during electrolyte removal, the EDS showed a clear Cu peak (95.2 at%) with a little bit of oxygen (2.2 at%) and aluminum (1.9 at%) on the surface (Fig. 35 b). This shows that the weak adhesion might not be because of insufficient acidic Cu pre-treatment of the copper substrate before assembling the Swagelok cells. But it is not fully documented, because there was no Al deposition on copper substrate without the acidic pre-treatment. In contrast to the blank surface of the working electrode, the deposited metal layer mainly consists of aluminum with a small amount of oxide formed on the surface (Fig. 35 c). Because the sample had to be transferred in ambient air to the SEM / EDX, the origin of the oxide layer is obvious. Otherwise, the deposited Al layer is free of impurities except Cl. A notably small Cl peak can be attributed to entrapment of electrolyte impurities in the deposited Al layer.

PIC 5

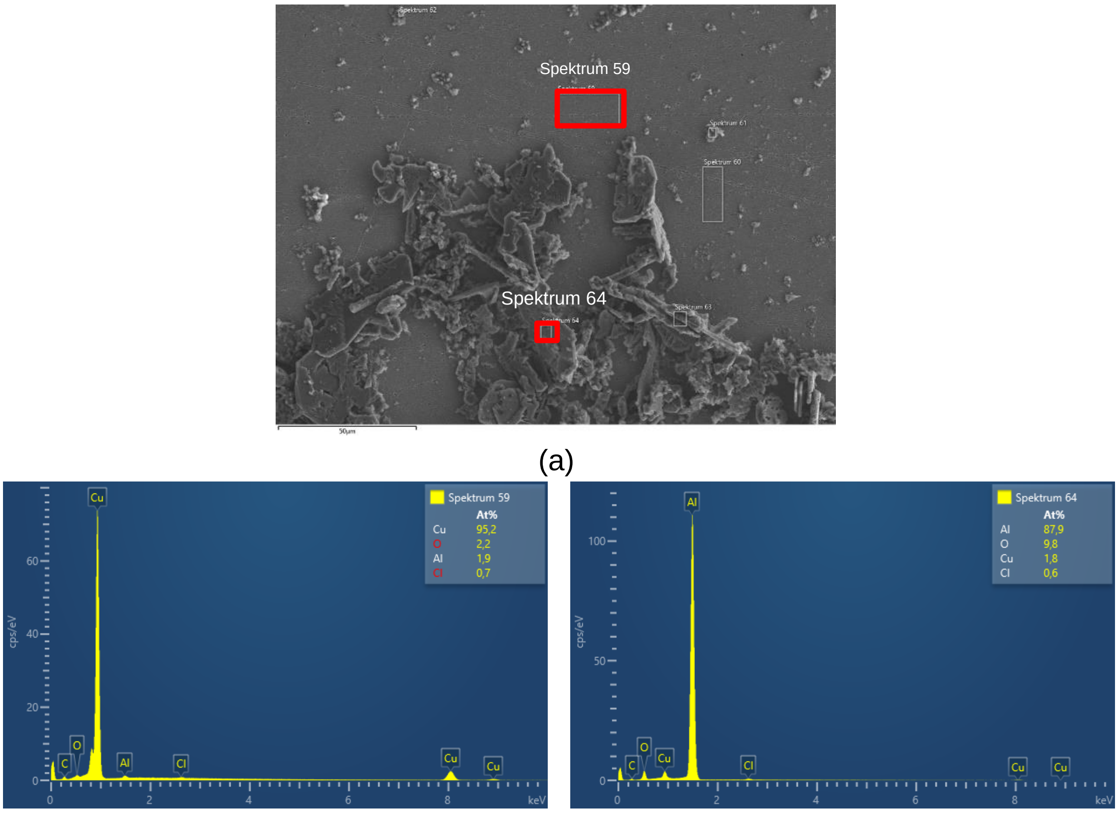

(a)

(b) (c)

Fig. 35: EDX spectra of PIC 5, where a) shows the area of the analysed WE surface, b) the spectra of the uncovered Cu surface and c) the spectra of the Al deposit.

4 Conclusion and outlook

The central theme of this thesis is to find pulse-current parameters for compact and homogeneous Al electrodeposition as half-cell reaction in secondary Al batteries. For that reason, the first step was to characterize the electrolyte Uralumina 150 with a composition of 1.5:1 molar ratio $AlCl_3$:urea by cyclic voltammetry. The first recorded CVs confirmed the necessity to compensate the resistance of the electrolyte during each potentiodynamic measurement due to the low electrical conductivity of the electrolyte (0.75 ± 0.19 mS/cm). Additionally, a polishing step before each measurement ensured a clean working electrode surface and reproducible conditions before the start of each CV. In the CVs on GC and Pt working electrodes no reduction peaks were detected, but a current, steadily rising until the cathodic switching potential. At Cu as substrate material, very broad reduction peaks could be detected, which indicates quasi-reversible behaviour. The peak current densities were plotted against the square root of the scan rate in a Randles-Sevcik plot to see if the system is diffusion controlled. The plot revealed that there is no linear correlation between the two quantities and the plot did not pass through the origin. This showed that the obtained data does not follow the Randles-Sevcik equation and that the system is not diffusion controlled.

In rotating disk electrode voltammetry on a Pt WE, current plateaus were observed at 50 mV/s and 10 mV/s. The current densities were plotted according to Levich equation. There was no linear correlation between the current density and the square root of the rotational rate. Because of the non-linearity it can be concluded that the diffusion is not the limiting step and a kinetic limitation is more presumable. According to Schaltin et al. [64] the limiting step in IL $AlCl_3$:[EMIm]Cl is the equilibrium between the dimeric electroactive species $[Al_2Cl_7]^-$ and the monomeric $[AlCl_4]^-$, which is not electroactive. This chemical equilibrium might be rate limiting also in the Uralumina 150 DES. This leads to Koutecky-Levich equation and the plot of the inverse of the limiting current density vs. the inverse of the square root of the rotational rate. The fit through the data points revealed a linear behaviour. The intercept at $\frac{1}{\omega^{1/2}} = 0$ is the inverse of the kinetically limited current density at infinite rotational rate and reflects only the kinetics of electron transfer or coupled chemical reactions. The intercept is used to calculate the rate constant for the reduction reaction k_{red} to be $9.08 \cdot 10^{-7}$ m/s. Secondly, the diffusion coefficient for the active species $[Al_2Cl_7]^-$ was calculated from the slope of the Koutecky-Levich plot as $2.39 \cdot 10^{-7}$ cm²/s. The kinetically limited current density was used to narrow down the parameter range for Al electrodeposition on Cu current collectors in Swagelok-type cells with Al counter electrodes. The obtained morphologies were compared according to Winand et al. [37] to see the impact of the deposition parameters on the electroplated Al.

During the direct current deposition, a current density of –0.067 mA/cm² leads to a flaky Al morphology. Based on this current density, pulsed current deposition was performed with varying duty cycle and frequency. By pulse interrupt current, the obtained Al metal layer should become dense, decrease in roughness and enable a charging of the battery without dendrite formation. The obtained grain shape was either cauliflower or flake like. The grain size decreased by increasing the pulse current density. A high current density leads to a high overpotential and might consequently provide enough energy to enable instantaneous nucleation on the substrate. The adhesion of the Al particles on the Cu substrate was poor. Especially after the pulsed electrodeposition with duty cycle of 0.01 and a frequency of 0.5 Hz, the Al particles were easily washed off. But on the other side, the morphology was the most homogenous one with a pulse current density of –6.71 mA/cm². All of the obtained Al layers had a high purity with little to no electrolyte entrapment in the deposit.

In further experiments, the kinetic limitations during the deposition process of Al from Uralumina 150 should be investigated in more detail. A better understanding of the reactions and their mechanisms in the electrolyte during the deposition process can help to improve the plated metal layer by finding parameters leading to a more compact Al morphology. After the optimization of the pulse parameter on the anode, the compatibility of these parameters with the battery cathode needs to be checked. The goal is to find parameters for the charging process of the secondary battery that lead to favourable effects on both electrodes, the anode and the cathode.

The influence of pulse reverse metal deposition can be tested, to see if the effect is as positive as reported in literature, even though the bipolar charging of a battery will not be the final goal for an energy efficient storage medium.

References

[1] A. Habib and C. Sou, “Analytical Review on the Trends and Present Situation of Large-scale Sustainable Energy Storage Technology,” *Eur. J. Sustain. Dev. Res.*, vol. 2, no. 3, 2018.

[2] T. M. Gür, “Review of electrical energy storage technologies, materials and systems: Challenges and prospects for large-scale grid storage,” *Energy Environ. Sci.*, vol. 11, no. 10, pp. 2696–2767, 2018.

[3] A. Habib, L. Ling, and B. Abbas, “Demand and Application of Energy Storage Technology in Renewable Energy Power System,” *Am. Sci. Res. J. Eng. Technol. Sci.*, no. September, pp. 2313–4410, 2017.

[4] D. Larcher and J. M. Tarascon, “Towards greener and more sustainable batteries for electrical energy storage,” *Nat. Chem.*, vol. 7, no. 1, pp. 19–29, 2015.

[5] H. Jiao, C. Wang, J. Tu, D. Tian, and S. Jiao, “A rechargeable Al-ion battery: Al/molten AlCl3-urea/graphite,” *Chem. Commun.*, vol. 53, no. 15, pp. 2331–2334, 2017.

[6] A. Chen and P. K. Sen, “Advancement in battery technology: A state-of-the-art review,” *IEEE Ind. Appl. Soc. 52nd Annu. Meet. IAS 2016*, pp. 1–10, 2016.

[7] S. Xia, X. M. Zhang, K. Huang, Y. Le Chen, and Y. T. Wu, “Ionic liquid electrolytes for aluminium secondary battery: Influence of organic solvents,” *J. Electroanal. Chem.*, vol. 757, pp. 167–175, 2015.

[8] C. Yan *et al.*, “Architecting a Stable High-Energy Aqueous Al-Ion Battery,” *J. Am. Chem. Soc.*, vol. 142, no. 36, pp. 15295–15304, 2020.

[9] F. Wu, N. Zhu, Y. Bai, Y. Gao, and C. Wu, “An interface-reconstruction effect for rechargeable aluminum battery in ionic liquid electrolyte to enhance cycling performances,” *Green Energy Environ.*, vol. 3, no. 1, pp. 71–77, 2018.

[10] A. Lahiri, N. Borisenko, and F. Endres, “Electrochemical Synthesis of Battery Electrode Materials from Ionic Liquids,” *Top. Curr. Chem.*, vol. 376, no. 2, pp. 1–29, 2018.

[11] D. Muñoz-Torrero *et al.*, “Investigation of different anode materials for aluminium rechargeable batteries,” *J. Power Sources*, vol. 374, no. October 2017, pp. 77–83, 2018.

[12] G. A. Elia *et al.*, “An Overview and Future Perspectives of Aluminum Batteries,” *Adv. Mater.*, vol. 28, no. 35, pp. 7564–7579, 2016.

[13] H. Yang *et al.*, “The Rechargeable Aluminum Battery: Opportunities and Challenges,” *Angew. Chemie - Int. Ed.*, vol. 58, no. 35, pp. 11978–11996, 2019.

[14] W. Chu, X. Zhang, J. Wang, S. Zhao, S. Liu, and H. Yu, “A low-cost deep eutectic

solvent electrolyte for rechargeable aluminum-sulfur battery,” *Energy Storage Mater.*, vol. 22, no. November 2018, pp. 418–423, 2019.

[15] H. Chen *et al.*, “Oxide Film Efficiently Suppresses Dendrite Growth in Aluminum-Ion Battery,” *ACS Appl. Mater. Interfaces*, vol. 9, no. 27, pp. 22628–22634, 2017.

[16] R. Böttcher, S. Mai, A. Ispas, and A. Bund, “Aluminum Deposition and Dissolution in [EMIm]Cl-Based Ionic Liquids–Kinetics of Charge–Transfer and the Rate–Determining Step,” *J. Electrochem. Soc.*, vol. 167, no. 10, p. 102516, 2020.

[17] Y. Hu, D. Sun, B. Luo, and L. Wang, “Recent Progress and Future Trends of Aluminum Batteries,” *Energy Technol.*, vol. 7, no. 1, pp. 86–106, 2019.

[18] A. P. Abbott and K. J. McKenzie, “Application of ionic liquids to the electrodeposition of metals,” *Phys. Chem. Chem. Phys.*, vol. 8, no. 37, pp. 4265–4279, 2006.

[19] K. V. Kravchyk and M. V. Kovalenko, “Aluminum electrolytes for Al dual-ion batteries,” *Commun. Chem.*, vol. 3, no. 1, pp. 1–9, 2020.

[20] A. A. J. Torriero, *Electrochemistry in Ionic Liquids - Volume 1:Fundamentals*. Springer, 2015.

[21] H. M. A. Abood and N. L. Dawood, “Morphology of electrodeposited aluminium metal from aluminium chloride-urea room temperature ionic liquid (RTIL) at variable parameters,” *Int. J. Sci. Res.*, vol. 4, no. 9, pp. 753–760, 2015.

[22] Y. Fang, X. Jiang, X. G. Sun, and S. Dai, “New ionic liquids based on the complexation of dipropyl sulfide and AlCl3 for electrodeposition of aluminum,” *Chem. Commun.*, vol. 51, no. 68, pp. 13286–13289, 2015.

[23] A. F. Holleman and N. Wiberg, *Lehrbuch der Anorganischen Chemie*, 102. de Gruyter, 2007.

[24] E. L. Smith, A. P. Abbott, and K. S. Ryder, “Deep Eutectic Solvents (DESs) and Their Applications,” *Chem. Rev.*, vol. 114, no. 21, pp. 11060–11082, 2014.

[25] H. M. A. Abood, A. P. Abbott, A. D. Ballantyne, and K. S. Ryder, “Do all ionic liquids need organic cations? Characterisation of [AlCl 2·nAmide]+ AlCl4- and comparison with imidazolium based systems,” *Chem. Commun.*, vol. 47, no. 12, pp. 3523–3525, 2011.

[26] M. Angell *et al.*, “High Coulombic efficiency aluminum-ion battery using an AlCl3-urea ionic liquid analog electrolyte,” *Proc. Natl. Acad. Sci. U. S. A.*, vol. 114, no. 5, pp. 834–839, 2017.

[27] Y. Bian *et al.*, “Using an AlCl3/Urea Ionic Liquid Analog Electrolyte for Improving the Lifetime of Aluminum-Sulfur Batteries,” *ChemElectroChem*, vol. 5, no. 23, pp. 3607–3611, 2018.

[28] C. Liu *et al.*, “Density, viscosity and electrical conductivity of AlCl3-amide ionic

liquid analogues," *J. Mol. Liq.*, vol. 247, pp. 57–63, 2017.

[29] Q. Zhang, K. De Oliveira Vigier, S. Royer, and F. Jérôme, "Deep eutectic solvents: Syntheses, properties and applications," *Chem. Soc. Rev.*, vol. 41, no. 21, pp. 7108–7146, 2012.

[30] Y. Liu, J. B. Friesen, J. B. McAlpine, D. C. Lankin, S. N. Chen, and G. F. Pauli, "Natural Deep Eutectic Solvents: Properties, Applications, and Perspectives," *J. Nat. Prod.*, vol. 81, no. 3, pp. 679–690, 2018.

[31] A. P. Abbott, J. C. Barron, K. S. Ryder, and D. Wilson, "Eutectic-based ionic liquids with metal-containing anions and cations," *Chem. - A Eur. J.*, vol. 13, no. 22, pp. 6495–6501, 2007.

[32] T. Jiang, M. J. Chollier Brym, G. Dubé, A. Lasia, and G. M. Brisard, "Electrodeposition of aluminium from ionic liquids: Part I-electrodeposition and surface morphology of aluminium from aluminium chloride (AlCl3)-1-ethyl-3-methylimidazolium chloride ([EMIm]Cl) ionic liquids," *Surf. Coatings Technol.*, vol. 201, no. 1–2, pp. 1–9, 2006.

[33] N. Kanani, *Electroplating - Basics Principles, Processes and Practice*. Elsevier, 2004.

[34] W. Schmickler and E. Santos, *Interfacial electrochemistry*, Second Edi. Springer, 2010.

[35] V. K. Lamer and R. H. Dinegar, "Theory, Production and Mechanism of Formation of Monodispersed Hydrosols," *J. Am. Chem. Soc.*, vol. 72, no. 11, pp. 4847–4854, 1950.

[36] M. Paunovic, M. Schlesinger, and D. D. Snyder, "Fundamental Considerations," in *Modern Electroplating*, Fifth Edit., M. Schlesinger and M. Paunovic, Eds. John Wiley & Sons, Inc., 2011, pp. 1–27.

[37] R. Winand, "Electrocrystallization - theory and applications," in *Hydrometallurgy, Theory and Practice*, vol. 29, W. C. Cooper and D. B. Dreisinger, Eds. Amsterdam: Elsevier Science Publishers B.V., 1992, pp. 567–598.

[38] H. Fischer, "Elektrochemie," in *Elektrolytische Abscheidung und Elektrokristallisation von Metallen.*, Springer, Berlin, 1954, p. 729.

[39] K. I. Popov, S. S. Djokic, and B. N. Grgur, *Fundamental Aspects of Electrometallurgy*. Kluwer Academic, 2002.

[40] Y. Gamburg and G. Zangari, *Theory and Practice of Metal Electrodeposition*. Springer, 2011.

[41] E. Rodríguez-Clemente *et al.*, "Aluminum Electrochemical Nucleation and Growth onto a Glassy Carbon Electrode from a Deep Eutectic Solvent," *J. Electrochem. Soc.*, vol. 166, no. 1, pp. D3035–D3041, 2019.

[42] A. Bakkar and V. Neubert, “Electrodeposition and corrosion characterisation of micro- and nano-crystalline aluminium from AlCl3/1-ethyl-3-methylimidazolium chloride ionic liquid,” *Electrochim. Acta*, vol. 103, pp. 211–218, 2013.

[43] T. Tsuda, G. R. Stafford, and C. L. Hussey, “Review—Electrochemical Surface Finishing and Energy Storage Technology with Room-Temperature Haloaluminate Ionic Liquids and Mixtures,” *J. Electrochem. Soc.*, vol. 164, no. 8, pp. H5007–H5017, 2017.

[44] V. S. Cvetkovic, N. M. Vukicevic, N. Jovicevic, J. S. Stefanovic, and J. N. Jovicevic, “Aluminium electrodeposition under novel conditions from AlCl3–urea deep eutectic solvent at room temperature,” *Trans. Nonferrous Met. Soc. China*, vol. 30, no. 3, pp. 823–834, 2020.

[45] T. Schoetz, O. Leung, C. P. de Leon, C. Zaleski, and I. Efimov, “ Aluminium Deposition in EMImCl-AlCl 3 Ionic Liquid and Ionogel for Improved Aluminium Batteries ,” *J. Electrochem. Soc.*, vol. 167, no. 4, p. 040516, 2020.

[46] J. Tang and K. Azumi, “Optimization of pulsed electrodeposition of aluminum from AlCl 3-1-ethyl-3-methylimidazolium chloride ionic liquid,” *Electrochim. Acta*, vol. 56, no. 3, pp. 1130–1137, 2011.

[47] B. Li, C. Fan, Y. Chen, J. Lou, and L. Yan, “Pulse current electrodeposition of Al from an AlCl3-EMIC ionic liquid,” *Electrochim. Acta*, vol. 56, no. 16, pp. 5478–5482, 2011.

[48] W. E. G. Hansal and S. Roy, *Pulse Plating*. Eugen G Leuze Verlag KG, 2012.

[49] J.-C. Puippe and F. Leaman, *Pulse-Plating*. Eugen G. Leuze Verlag KG, 1986.

[50] C. G. Zoski, *Handbook of electrochemistry*. Elsevier B.V, 2007.

[51] N. Ibl, “Some theoretical aspects of pulse electrolysis,” *Surf. Technol.*, vol. 10, no. 2, pp. 81–104, 1980.

[52] A. J. Bard and L. R. Faulkner, *Electrochemical methods: fundamentals and applications*. John Wiley & Sons, Inc., 2001.

[53] D. Pletcher, R. Greef, R. Peat, L. M. Peter, and J. Robinson, *Instrumental Methods in Electrochemistry*, vol. 12. Woodhead Publishing Limited, 2001.

[54] B. Soediono, “Electrocheimical dictionary,” *J. Chem. Inf. Model.*, vol. 53, p. 160, 1989.

[55] D. Britz, “iR elimination in electrochemical cells,” *J. Electroanal. Chem*, vol. 88, pp. 309–352, 1978.

[56] W. Oelßner, F. Berthold, and U. Guth, “The iR drop - Well-known but often underestimated in electrochemical polarization measurements and corrosion testing,” *Mater. Corros.*, vol. 57, no. 6, pp. 455–466, 2006.

[57] E. P. Achterberg, “Laboratory techniques in electroanalytical chemistry,” *TrAC*

Trends Anal. Chem., vol. 15, no. 10, p. 550, 1996.

[58] M. Xu, G. Yue, D. Bizzotto, and E. Asselin, “Electrodeposition of Aluminum onto Copper-Coated Printed Circuit Boards,” *J. Electrochem. Soc.*, vol. 164, no. 12, pp. D729–D736, 2017.

[59] J. Heinze, A. Rasche, M. Pagels, and B. Geschke, “On the origin of the so-called nucleation loop during electropolymerization of conducting polymers,” *J. Phys. Chem. B*, vol. 111, no. 5, pp. 989–997, 2007.

[60] M. Jafarian, M. G. Mahjani, F. Gobal, and I. Danaee, “Electrodeposition of aluminum from molten AlCl3-NaCl-KCl mixture,” *J. Appl. Electrochem.*, vol. 36, no. 10, pp. 1169–1173, 2006.

[61] M. S. Al Farisi, S. Hertel, M. Wiemer, and T. Otto, “Aluminum patterned electroplating from AlCl3-[EMIm]Cl ionic liquid towards microsystems application,” *Micromachines*, vol. 9, no. 11, 2018.

[62] D. Pletcher, *A First Course in Electrode Processes*, Second Edi. The Royal Society of Chemistry, 2009.

[63] D. Lloyd, T. Vainikka, S. Schmachtel, L. Murtomäki, and K. Kontturi, “Simultaneous characterisation of electrode kinetics and electrolyte properties in ionic liquids using a rotating disc electrode,” *Electrochim. Acta*, vol. 69, pp. 139–145, 2012.

[64] S. Schaltin, M. Ganapathi, K. Binnemans, and J. Fransaer, “Modeling of Aluminium Deposition from Chloroaluminate Ionic Liquids,” *J. Electrochem. Soc.*, vol. 158, no. 10, pp. D634–D39, 2011.

[65] Á. Miguel *et al.*, “Understanding the Molecular Structure of the Elastic and Thermoreversible AlCl3 : Urea/Polyethylene Oxide Gel Electrolyte,” *ChemSusChem*, vol. 13, pp. 1–9, 2020.

[66] C. Wang, J. Li, H. Jiao, J. Tu, and S. Jiao, “The electrochemical behavior of an aluminum alloy anode for rechargeable Al-ion batteries using an AlCl3-urea liquid electrolyte,” *RSC Adv.*, vol. 7, no. 51, pp. 32288–32293, 2017.

[67] R. T. Carlin, “Nucleation and Morphology Studies of Aluminum Deposited from an Ambient-Temperature Chloroaluminate Molten Salt,” *J. Electrochem. Soc.*, vol. 139, no. 1, p. 2720, 1992.

[68] D. Pradhan and R. G. Reddy, “Dendrite-free aluminum electrodeposition from AlCl 3-1-ethyl-3- methyl-imidazolium chloride ionic liquid electrolytes,” *Metall. Mater. Trans. B Process Metall. Mater. Process. Sci.*, vol. 43, no. 3, pp. 519–531, 2012.

[69] V. A. Elterman, P. Y. Shevelin, L. A. Yolshina, E. G. Vovkotrub, and A. V. Borozdin, “Effects of AlCl3–1-ethyl-3-methylimidazolium chloride ionic liquid composition on transport properties,” *J. Mol. Liq.*, vol. 320, p. 114482, 2020.

List of Figures

List of Tables

Appendix

Electrochemical impedance spectroscopy (EIS)

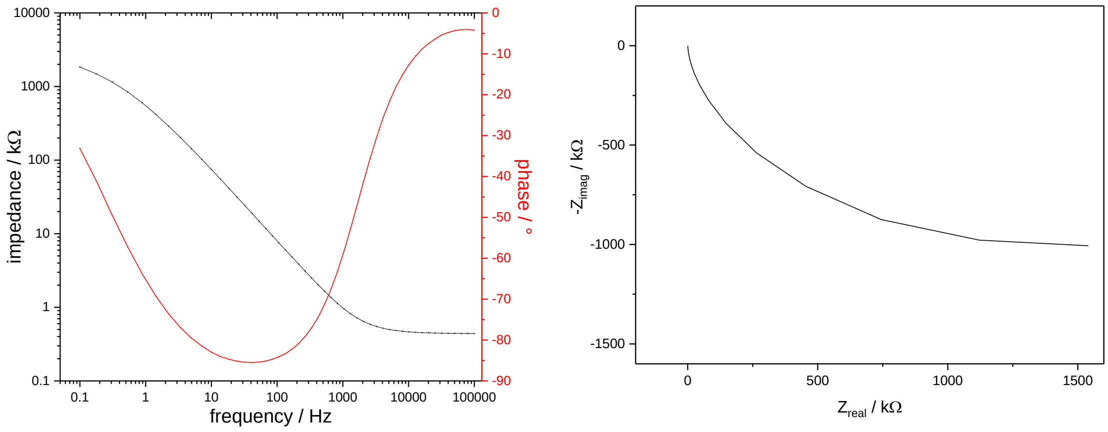

(a) (b)

Fig. 1A: a) Bode impedance spectra and b) Nyquist impedance spectra of Al electrode at 0 V vs. Al/Al^{3+} in Uralumina 150 recorded in Swagelok cell. The resistance of the electrolyte Uralumina 150 is determined to be R=617 Ω and the electrical conductivity is calculated to be 0.66 mS/cm². The data were obtained over the frequency range 100 kHz - 100 mHz.

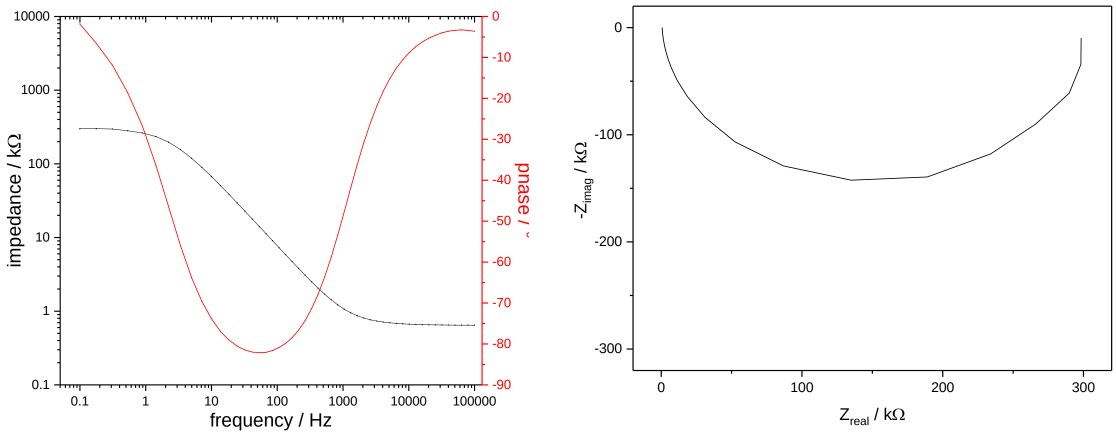

(a) (b)

Fig. 2A: a) Bode impedance spectra and b) Nyquist impedance spectra of Al electrode at 0 V vs. Al/Al3+ in Uralumina 150 recorded in Swagelok cell. The resistance of the electrolyte is determined to be R=643 Ω and the electrical conductivity is calculated to be 0.63 mS/cm². The data were obtained over the frequency range 100 kHz - 100 mHz.

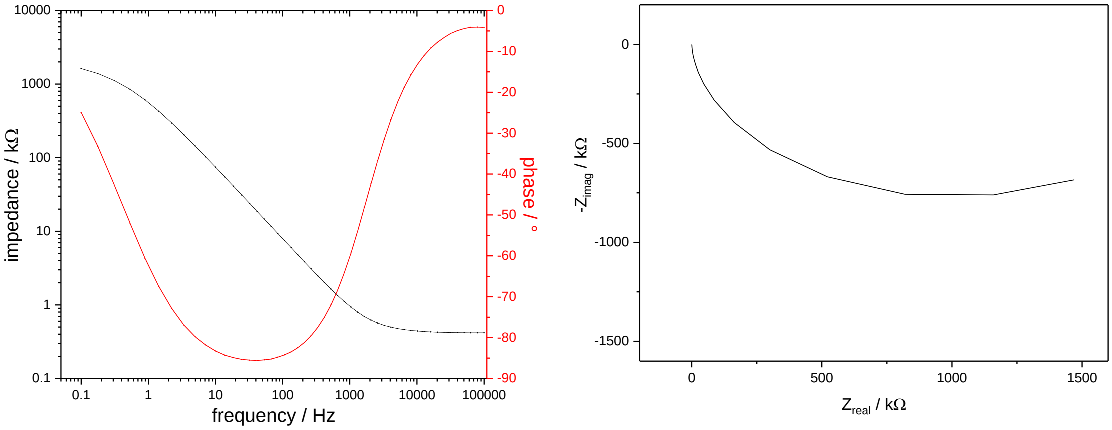

(a) (b)

Fig. 3A: a) Bode impedance spectra and b) Nyquist impedance spectra of Al electrode at 0 V vs. Al/Al^{3+} in Uralumina 150 recorded in Swagelok cell. The resistance of the electrolyte is determined to be R=415 Ω and based on R the electrical conductivity is calculated to be 0.98 mS/cm^2. The data were obtained over the frequency range 100 kHz - 100 mHz.

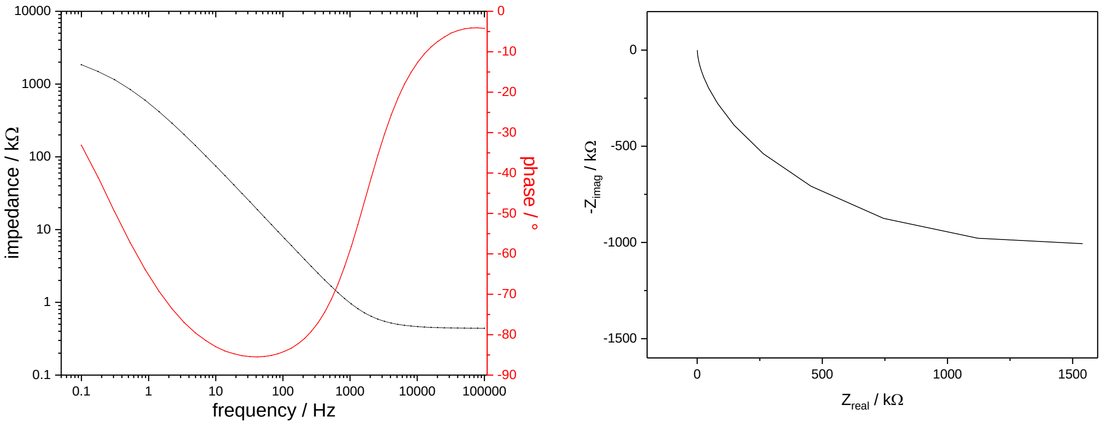

(a) (b)

Fig. 4A: a) Bode impedance spectra and b) Nyquist impedance spectra of Al electrode at 0 V vs. Al/Al^{3+} in Uralumina 150 recorded in Swagelok cell. The resistance of the electrolyte is measured to be R=438 Ω and the electrical conductivity of the electrolyte is 0.93 mS/cm^2. The data were obtained over the frequency range 100 kHz - 100 mHz.

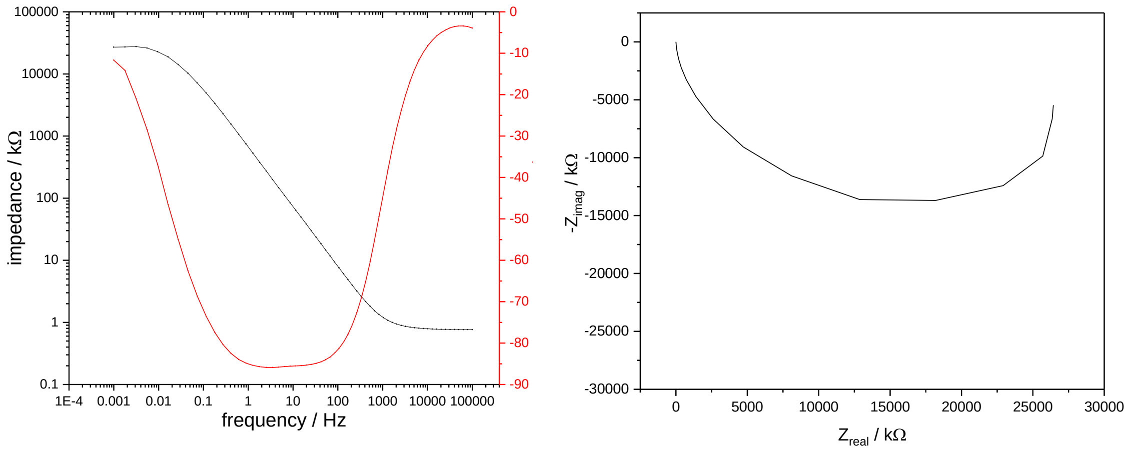

(a) (b)

Fig. 5A: a) Bode impedance spectra and b) Nyquist impedance spectra of Al electrode at 0 V vs. Al/Al^{3+} in Uralumina 150 recorded in Swagelok cell. The resistance of the electrolyte Uralumina 150 is determined to be R=712 Ω and the electrical conductivity is calculated to be 0.57 mS/cm². The data were obtained over the frequency range 100 kHz - 1 mHz.

Cyclic voltammetry

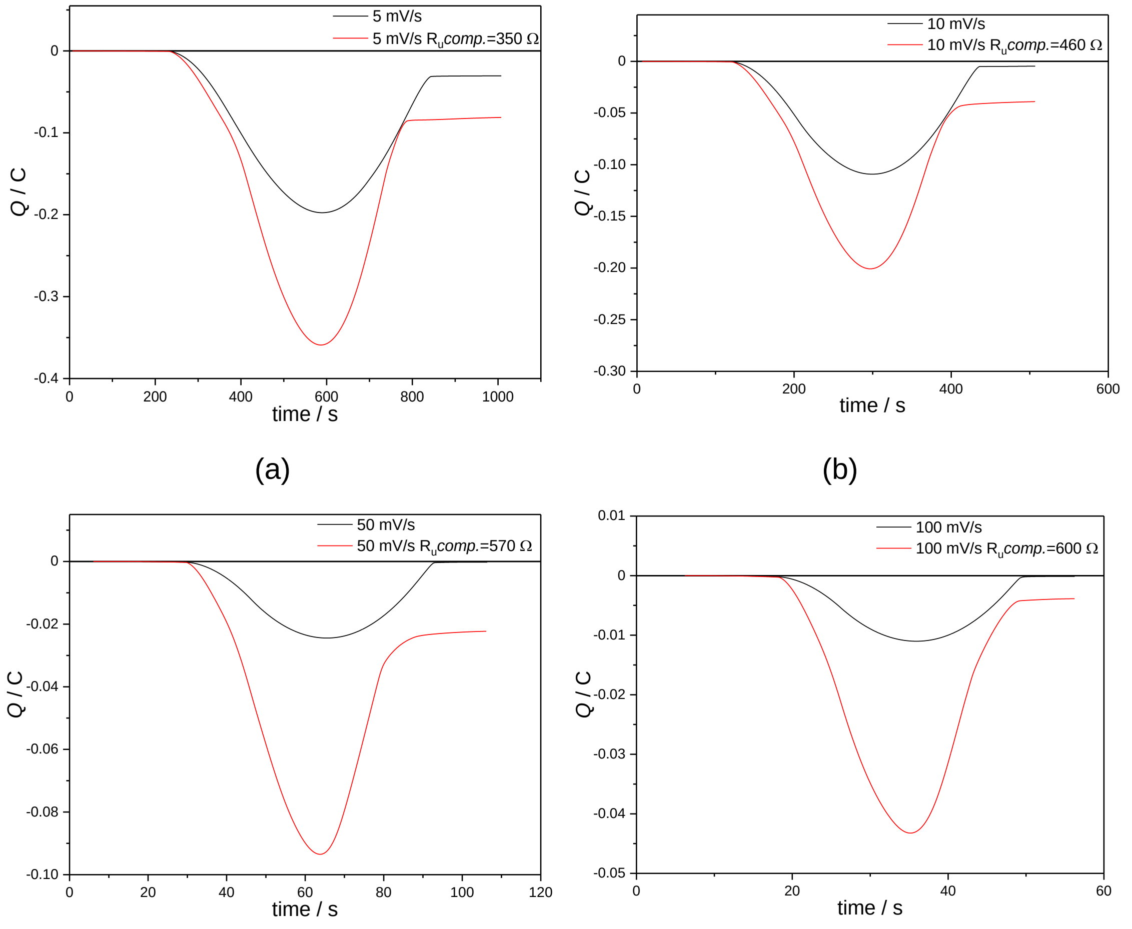

(a) (b)

(c) (d)

Fig. 6A: The coulombic efficiencies (CEff) according to Table 2. The Al deposition was performed on Pt WE in Uralumina 150 with (red line) and without (black line) iR drop compensation. The scan rates ranged from a) 5 mV/s b) 10 mV/s c) 50 mV/s to d) 100 mV/s.

Table 1A: Cathodic peak potentials and peak current densities of CV on Cu working electrode with different scan rates (according to Fig. 16 b)

scan rate [*mV/s*] / R_u*comp.*	peak potential [*V*]	peak current density [*j/mA cm*$^{-2}$]
5 / *200* Ω	-0.92	-14.7
10 / 400 Ω	-0.66	-33.4
50 / 600 Ω	-0.86	-35.1
100 / 600 Ω	-1.0	-34.8

Table 2A: Cathodic peak potentials and peak current densities of CV on Cu working electrode with different scan rates (according to Fig. 19 b).

scan rate [*mV/s*] / R_u*comp.*	peak potential [*V*]	peak current density [*j/mA cm*$^{-2}$]
1 / *0* Ω	-0.85	-27.3
2 / 100 Ω	-0.80	-32.1
5 / 200 Ω	-0.92	-14.7
10 / 400 Ω	-0.66	-33.3
20 / 500	-0.82	-27.4
50 / 600	-0.86	-35.1
100 / 600	-1.0	-34.8
200 / 700	-1.0	-57.9
500 / 700	-0.51	-65.3
1000 / 700	-0.72	-73.1

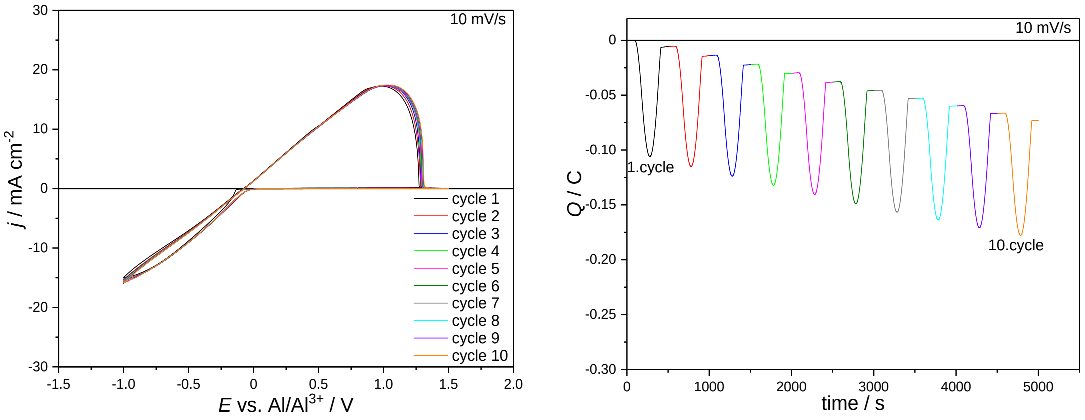

(a) (b)

Fig. 7A: a) Multi cycle cyclic voltammetry at 10 mV/s on Pt WE without ohmic drop correction and b) the corresponding CEff for aluminum deposition of all 10 cycles.

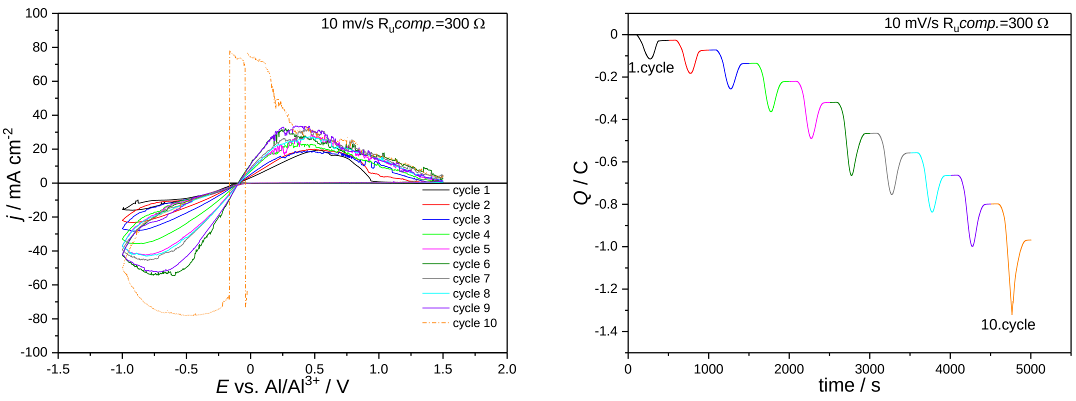

(a) (b)

Fig. 8A: a) Multi cycle cyclic voltammetry at 10 mV/s on Pt WE with iR drop compensation and b) the corresponding CEff for aluminum deposition of all 10 cycles. The 10th cycle should not be determined, because the scan failed.

Table 3A: Coulombic efficiencies of the multi cycle CV performed at 10 mV/s.

10 mV/s		10 mV/s *R* comp. = 300 Ω	
cycle	CEff	cycle	CEff
1	94.96 %	1	77.08 %
2	92.56 %	2	70.51 %
3	92.59 %	3	65.91 %
4	92.86 %	4	62.78 %
5	92.70 %	5	63.25 %
6	93.0 %	6	57.73 %
7	93.53 %	7	68.19 %
8	93.78 %	8	62.22 %
9	93.93 %	9	59.74 %
10	94.04 %	-	-

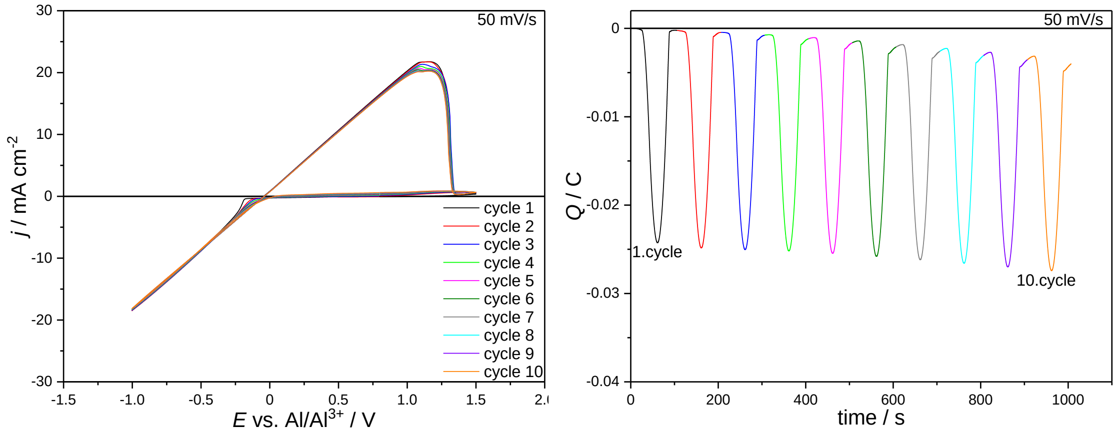

(a) (b)

Fig. 9A: a) Multi cycle cyclic voltammetry at 50 mV/s on Pt WE without ohmic drop correction and b) the corresponding CEff for aluminum deposition of all 10 cycles.

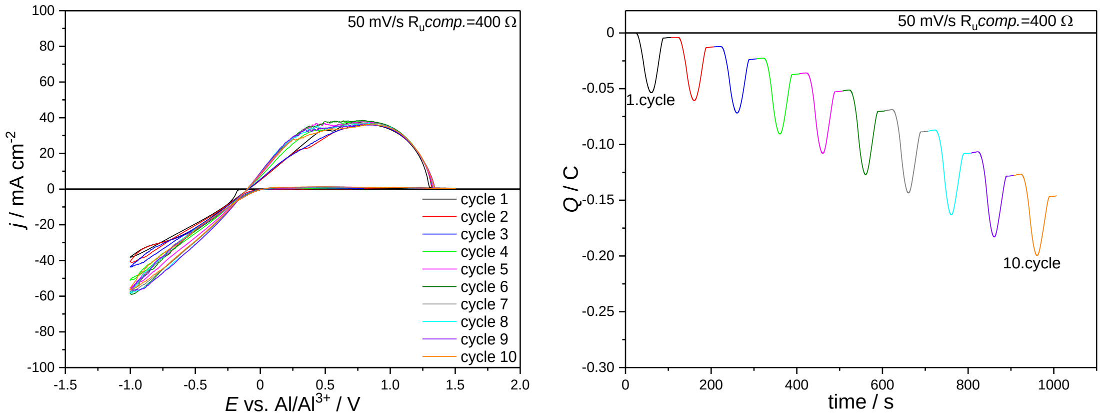

(a) (b)

Fig. 10A: a) Multi cycle cyclic voltammetry at 50 mV/s on Pt WE with iR drop compensation of 400 Ω and b) the corresponding CEff for aluminum deposition of all 10 cycles.

Table 4A: Coulombic efficiencies of the multi cycle CV performed at 50 mV/s.

50 mV/s		50 mV/s *R* comp. = 400 Ω	
cycle	CEff	cycle	CEff
1	99.11 %	1	92.57 %
2	99.06 %	2	85.47 %
3	98.92 %	3	82.44 %
4	98.65 %	4	80.60 %
5	98.46 %	5	78.76 %
6	98.32 %	6	76.79 %
7	98.24 %	7	75.61 %
8	98.20 %	8	74.30 %
9	98.20 %	9	73.77 %
10	96.44 %	10	73.31 %

Rotating disk electrode (RDE) voltammetry

Table 5A: Cathodic plateau potentials and plateau current densities of RDE voltammetry on Pt working electrode with different rotational rates at 50 mV/s and R comp. *= 590 Ω (according to Fig. 21 b).*

rotational rate [*rpm*]	plateau potential [*V*]	plateau current density [*j/mA cm*$^{-2}$]
100	-0.75	-61.1
400	-0.97	-69.2
900	-1.0	-80.4
1600	-1.0	-78.6
2500	-1.0	-73.9
3600	-1.0.	-76.3
4900	-1.0	-76.3

Table 6A: Cathodic plateau potentials and plateau current densities of RDE voltammetry on Pt working electrode with different rotational rates at 10 mV/s and R comp. = *540 Ω (according to Fig. 22 b).*

rotational rate [*rpm*]	plateau potential [*V*]	plateau current density [*j/mA cm*$^{-2}$]
100	-1.0	-33.3
400	-1.0	-44.1
900	-1.0	-50.2
1600	-0.9	-65.1
2500	-1.0	-53.7
3600	-1.0	-60.8
4900	-1.0	-59.7

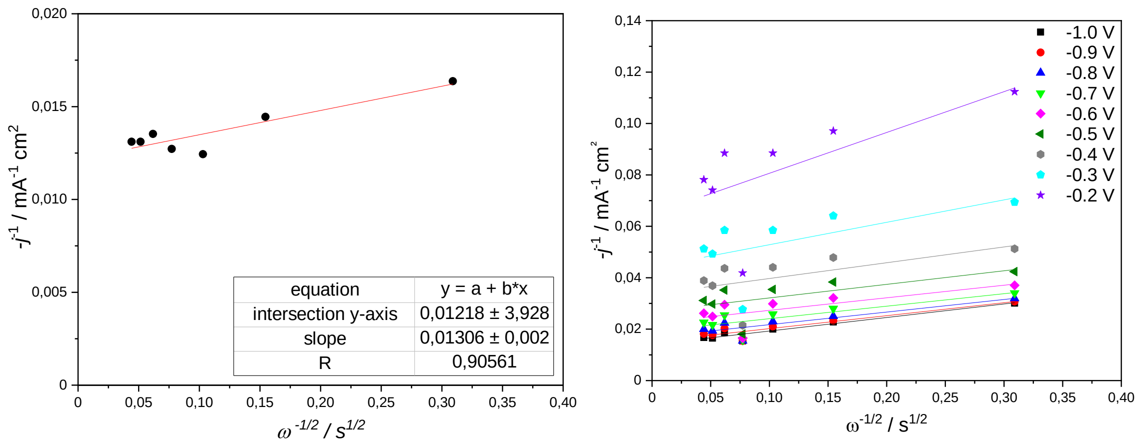

(a) (b)

Fig. 11A: Koutecky-Levich plot of j^{-1} *vs.* $\omega^{-1/2}$ *at a scan rate of a) 50 mV/s and b) 10 mV/s in Uralumina 150 with Pt working electrode.*

Pulse-interrupt current (PIC) aluminum plating

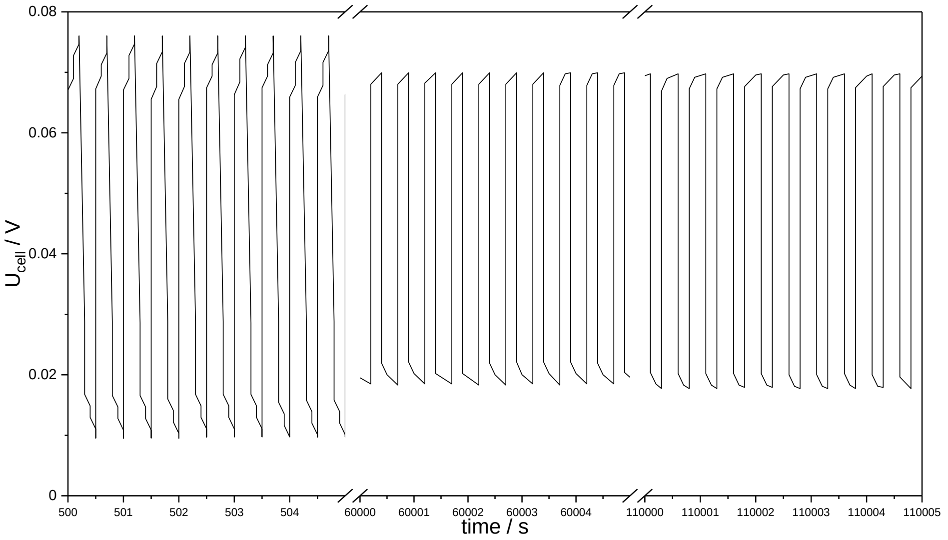

Fig. 12A: Cell voltage of PIC 1 at 500 s, 60 000 s and 110 000 s.

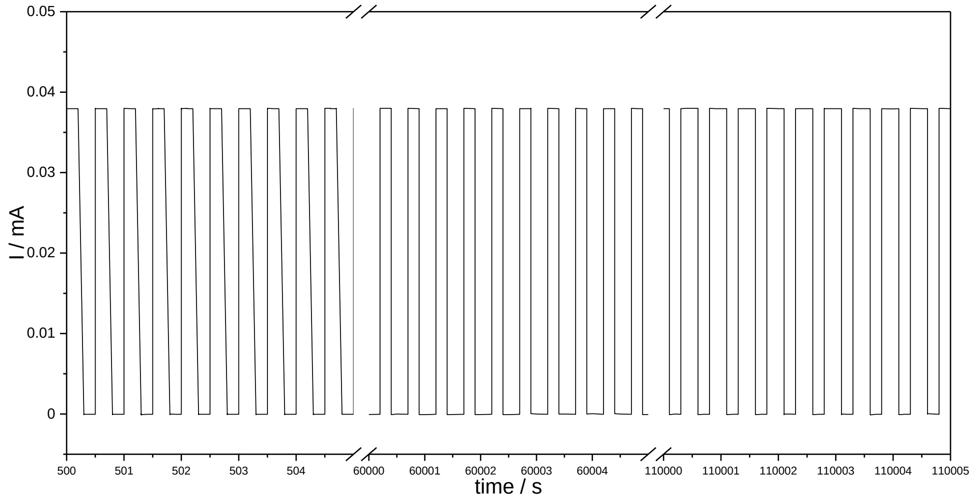

Fig. 13A: Measured current of PIC 1 at 500 s, 60 000 s and 110 000 s.

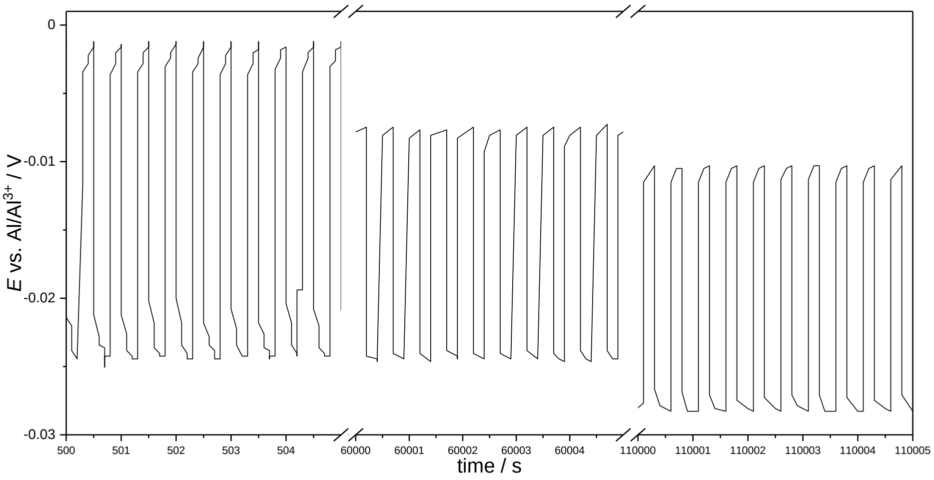

Fig. 14A: Potential of the Cu working electrode vs. Al/Al^{3+} in PIC 1 at 500 s, 60 000 s and 110 000 s.

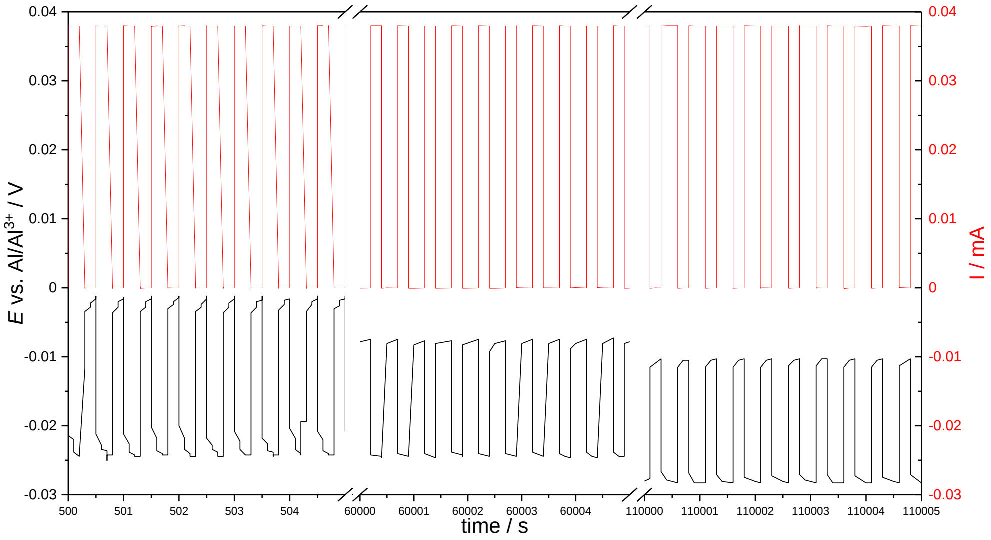

Fig. 15A: Potential of the Cu working electrode vs. Al/Al^{3+} in PIC 1 (black line) and the measured current of the cell at 500 s, 60 000 s and 110 000 s (red line).

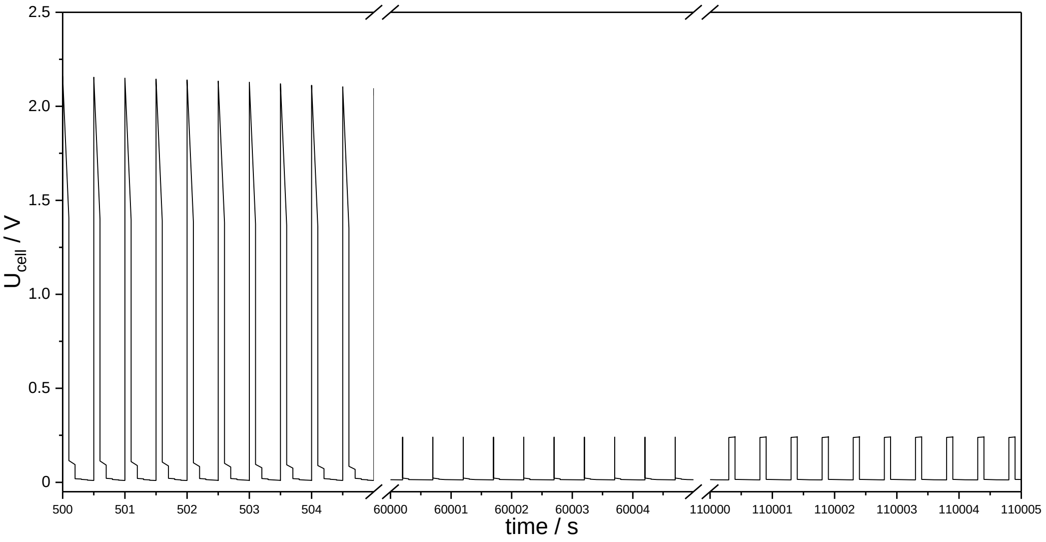

Fig. 16A: Cell voltage of PIC 2 at 500 s, 60 000 s and 110 000 s.

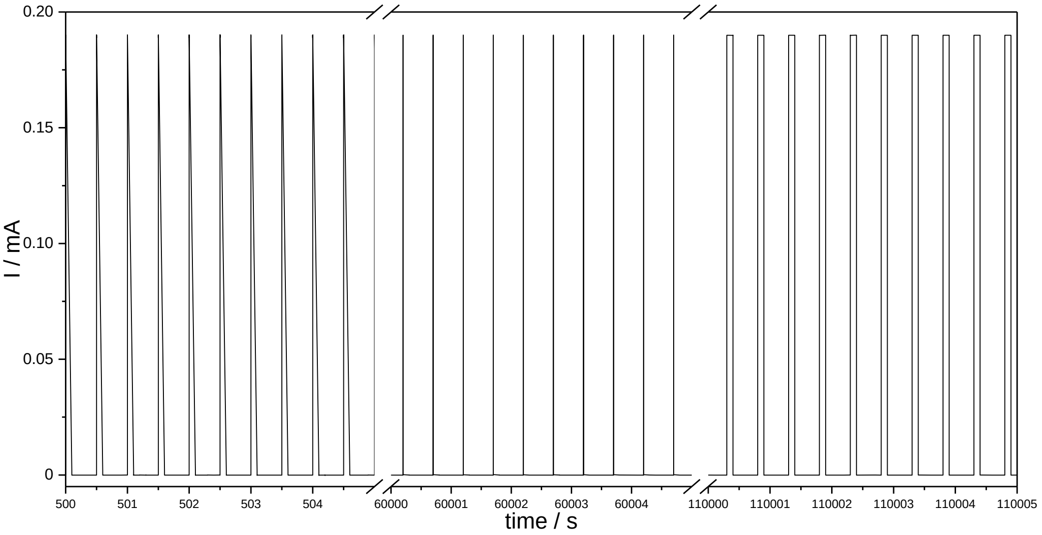

Fig. 17A: Measured current of PIC 2 at 500 s, 60 000 s and 110 000 s.

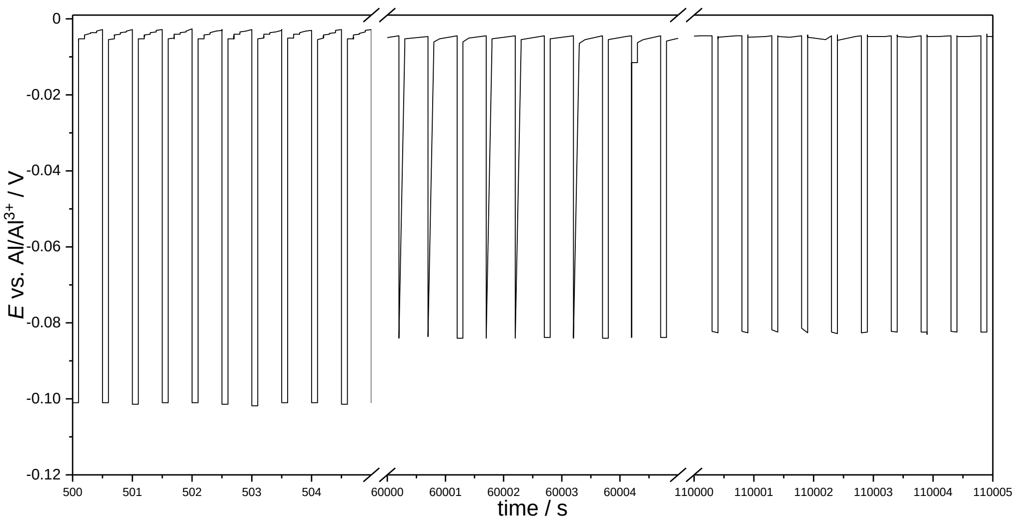

Fig. 18A: Potential of the Cu working electrode vs. Al/Al^{3+} in PIC 2 at 500 s, 60 000 s and 110 000 s.

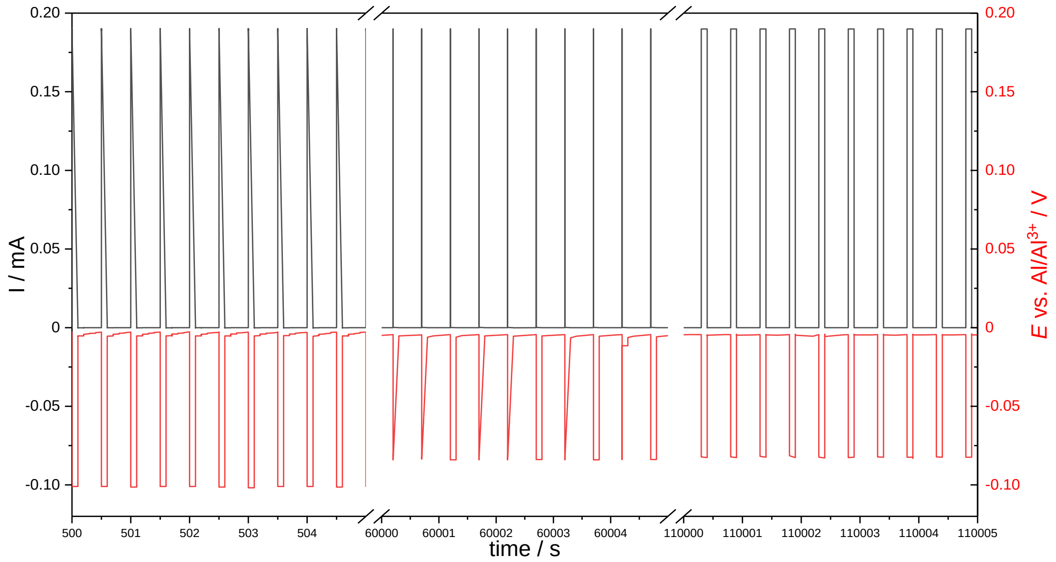

Fig. 19A: Potential of the Cu working electrode vs. Al/Al^{3+} in PIC 2 (red line) and the measured current of the cell at 500 s, 60 000 s and 110 000 s (black line).

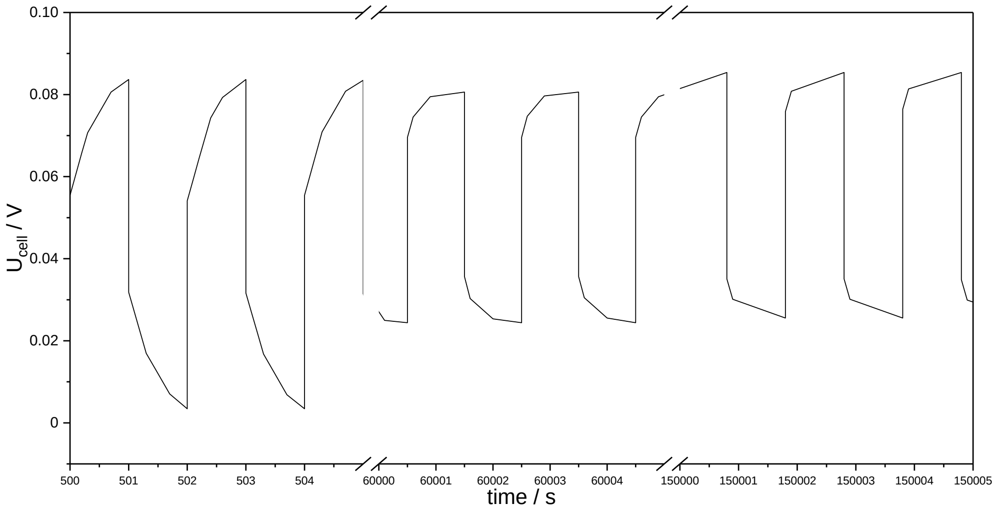

Fig. 20A: Cell voltage of PIC 3 at 500 s, 60 000 s and 150 000 s.

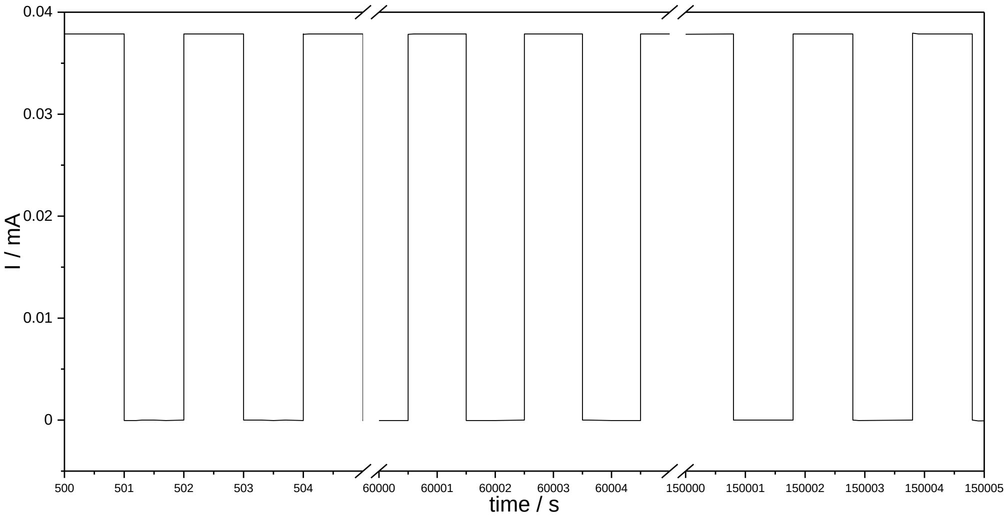

Fig. 21A: Measured current of PIC 3 at 500 s, 60 000 s and 150 000 s.

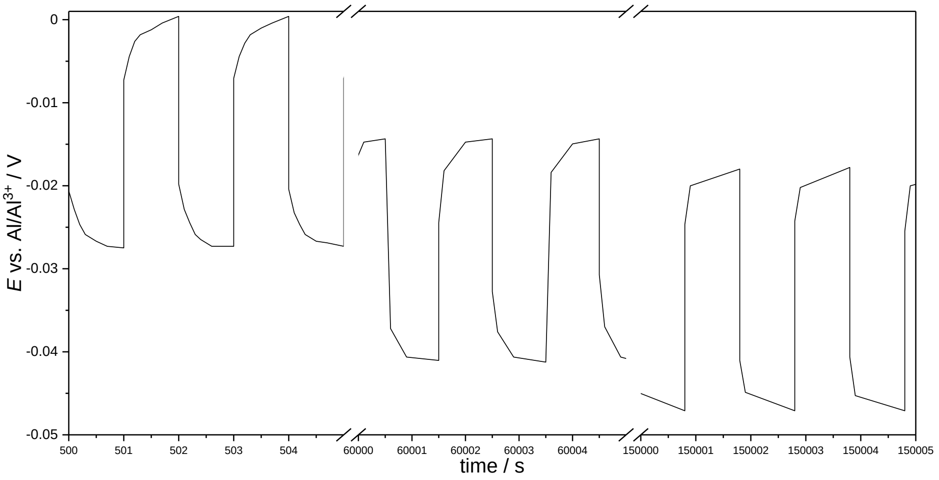

Fig. 22A: Potential of the Cu working electrode vs. Al/Al^{3+} *in PIC 3 at 500 s, 60 000 s and 150 000 s.*

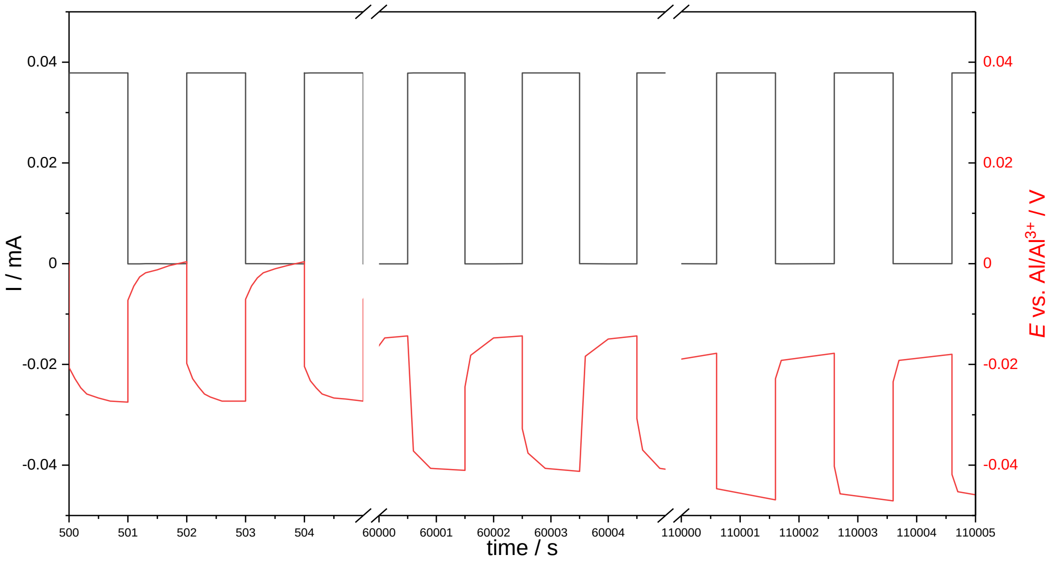

Fig. 23A: Potential of the Cu working electrode vs. Al/Al^{3+} *in PIC 3 (red line) and the measured current of the cell at 500 s, 60 000 s and 150 000 s (black line).*

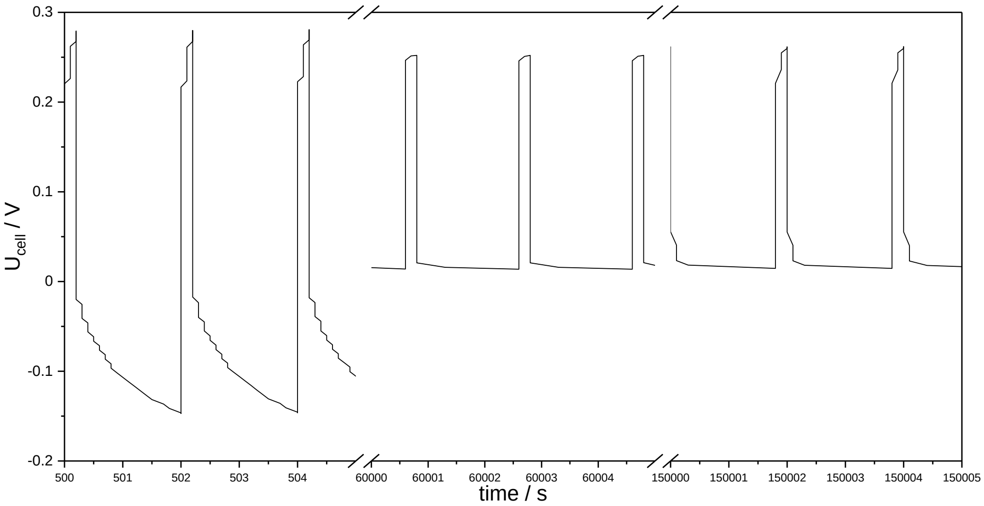

Fig. 24A: Cell voltage of PIC 4 at 500 s, 60 000 s and 150 000 s.

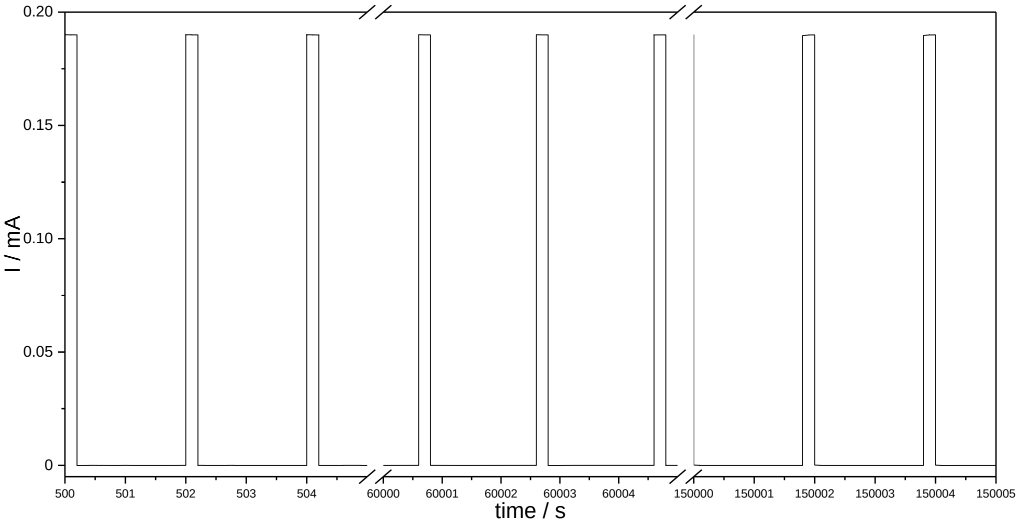

Fig. 25A: Measured current of PIC 4 at 500 s, 60 000 s and 150 000 s.

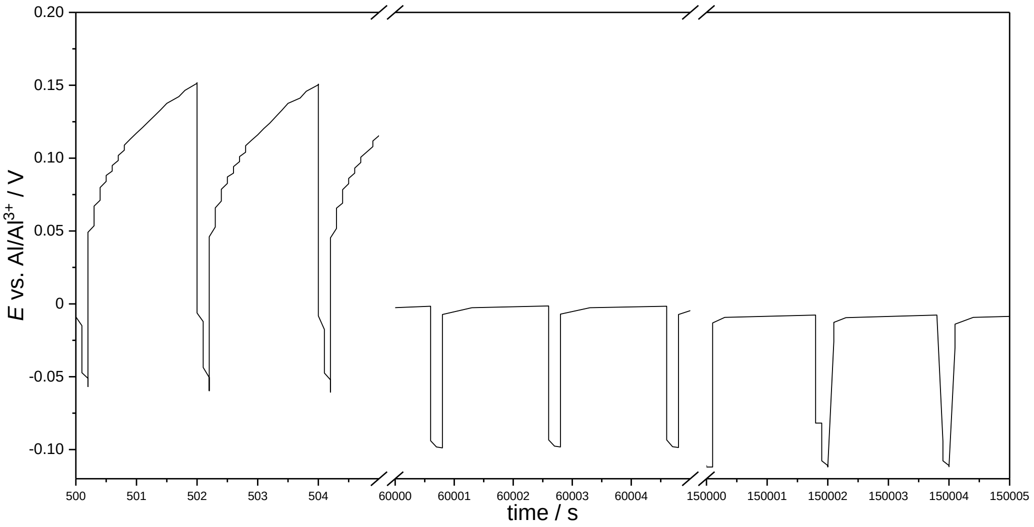

Fig. 26A: Potential of the Cu working electrode vs. Al/Al^{3+} in PIC 4 at 500 s, 60 000 s and 150 000 s.

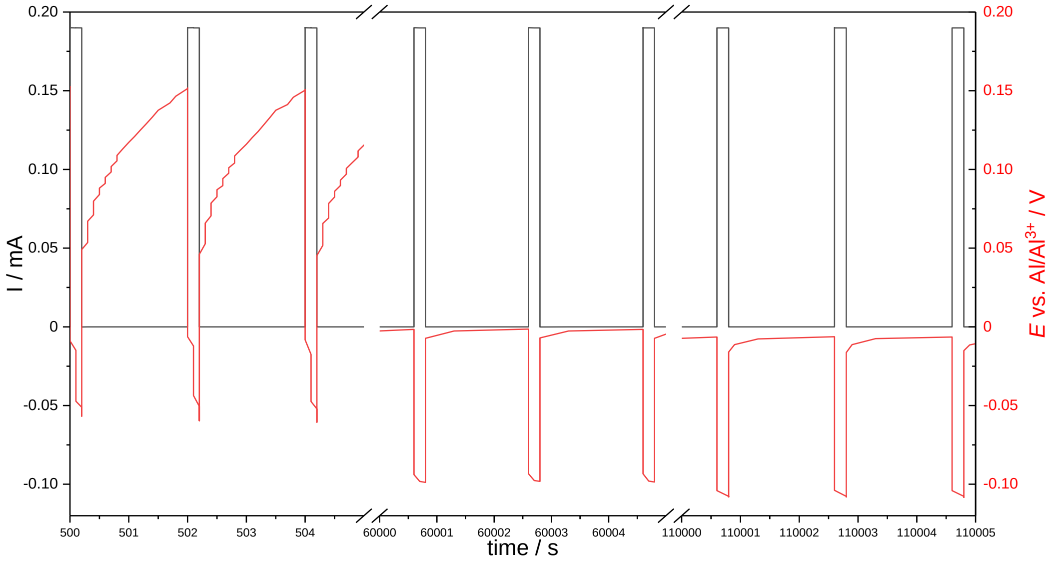

Fig. 27A: Potential of the Cu working electrode vs. Al/Al^{3+} in PIC 4 (red line) and the measured current of the cell at 500 s, 60 000 s and 150 000 s (black line).

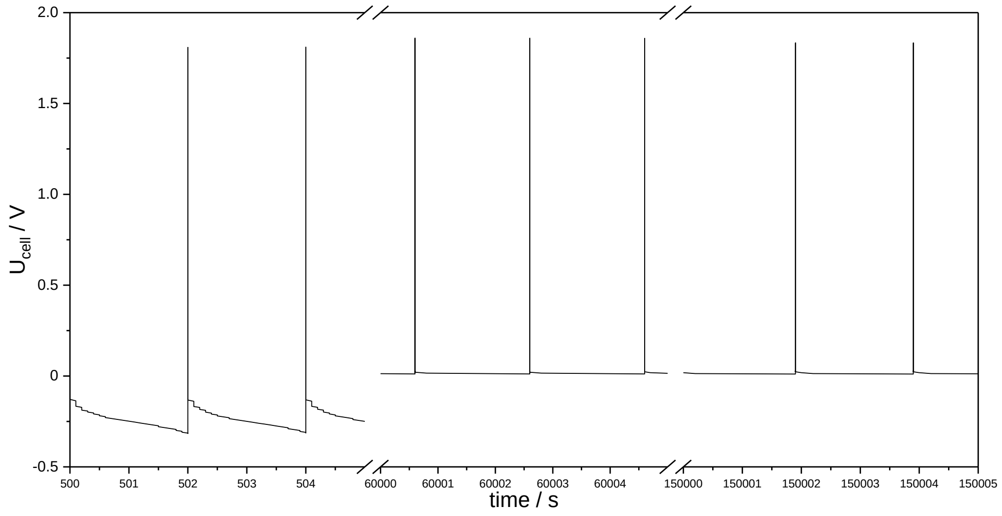

Fig. 28A: Cell voltage of PIC 5 at 500 s, 60 000 s and 150 000 s.

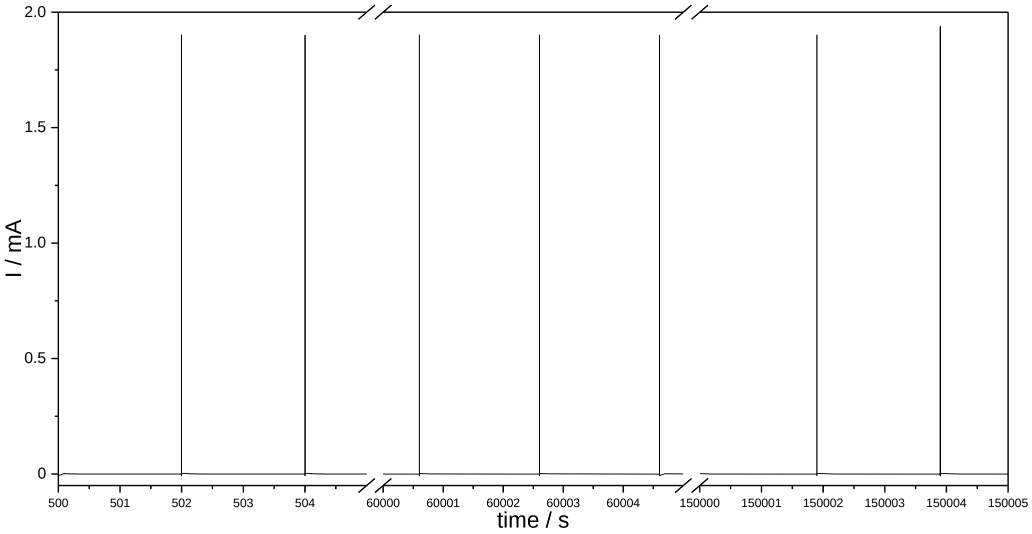

Fig. 29A: Measured current of PIC 5 at 500 s, 60 000 s and 150 000 s.

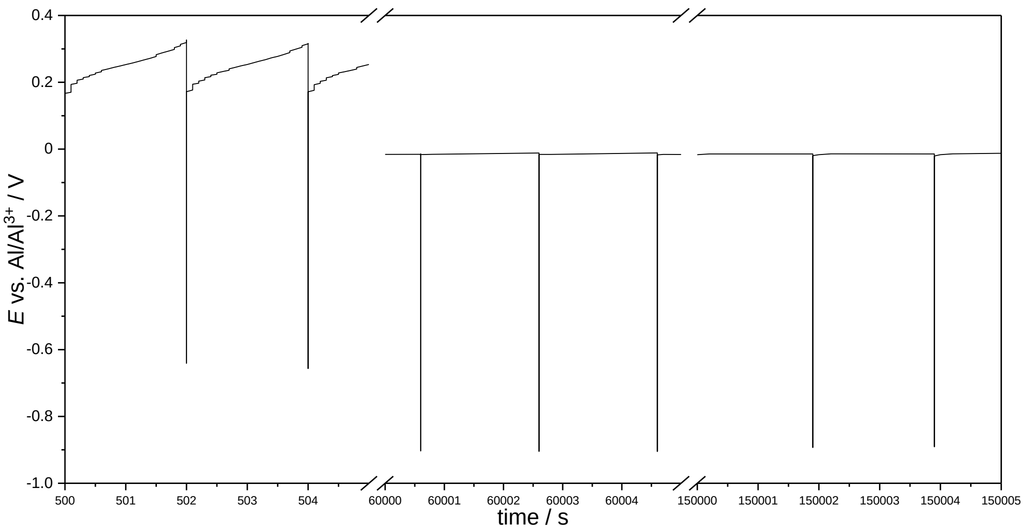

Fig. 30A: Potential of the Cu working electrode vs. Al/Al3+ in PIC 5 at 500 s, 60 000 s and 150 000 s.

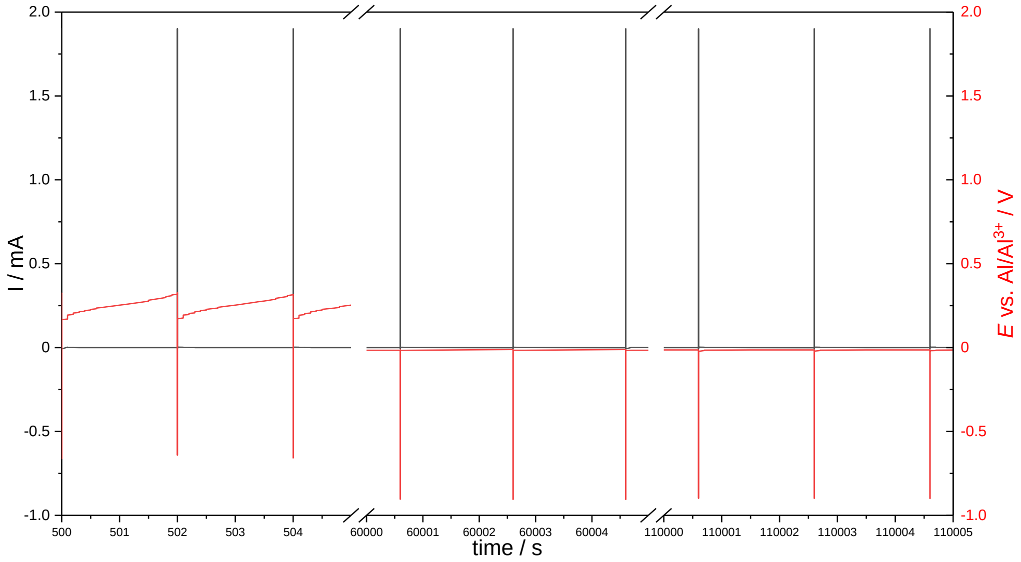

Fig. 31A: Potential of the Cu working electrode vs. Al/Al^{3+} in PIC 5 (red line) and the measured current of the cell at 500 s, 60 000 s and 150 000 s (black line).